

THE UNIVERSITY
of ADELAIDE

Enhanced coherent control of spin states in a quantum dot using the AC Stark effect

by

Josiah Ethan Hsi

In fulfilment of the requirements for the degree of

Master of Philosophy

September 2025

School of PCES

Department of Physics

The University of Adelaide

Contents

Declaration ix

Acknowledgements xi

Abstract xiii

1 Introduction 1

2 Theoretical background 5
- 2.1 Foundations of quantum technologies . . . 5
  - 2.1.1 Historical context . . . 5
  - 2.1.2 Quantum bits . . . 5
  - 2.1.3 Entanglement . . . 8
  - 2.1.4 Multi-partite entangled states . . . 9
- 2.2 Single photon sources . . . 10
- 2.3 Semiconductor quantum dots . . . 16
  - 2.3.1 Carrier states in quantum dots . . . 16
  - 2.3.2 Decoherence mechanisms . . . 19
  - 2.3.3 Optical selection rules . . . 20
- 2.4 Entangled state production in quantum dots . . . 23
- 2.5 Linear cluster state generation: the Lindner and Rudolph protocol . . . 26

3 The combined Zeeman-AC Stark effect on the trion-hole manifold 31
- 3.1 Light-matter interactions and the optical Stark effect . . . 31
- 3.2 Mathematical description of the trion manifold . . . 37
- 3.3 Simulated emission spectrum . . . 38
- 3.4 Spin precession frequency . . . 43
- 3.5 Outlook . . . 46

4 Experimental progress 49
- 4.1 Experiment design . . . 49
  - 4.1.1 Cryogenic system . . . 49

4.1.2 Magnet assembly 52
4.1.3 Laser systems 54
4.1.4 Optical measurement elements 58
4.1.5 Optical setup 59
4.2 Photoluminescence spectroscopy on QD samples 61
4.2.1 Micro-photoluminescence spectroscopy 61
4.2.2 Time resolved photoluminescence 63
4.3 Outlook and future work 64

5 Summary and Outlook **67**

A Appendix of Chapter 3 **69**
A.1 Derivation of the rotating wave approximation 69

Bibliography **71**

List of Tables

2.1 Single photon performance of selected platforms in the current literature 14
2.2 Literature cluster state production rates for various QD spin states. . . 28

List of Figures

2.1 Bloch sphere representation of a qubit. 6
2.2 Second order correlation function for various light sources 11
2.3 Experimental schematics for measuring single photon properties 13
2.4 Schematic of droplet etched epitaxial GaAs/AlGaAs quantum dots. . . 17
2.5 Band structure of a III-V semiconductor around the Γ symmetry point. 18
2.6 Various exciton states within a QD. 19
2.7 Positively charged exciton complex in the presence of magnetic fields with different orientations 21
2.8 Allowed transitions in a QD 24
2.9 Lindner and Rudolph protocol visualised on the Bloch sphere. 28

3.1 Dressed state energies in the rotating frame 34
3.2 Rabi oscillations as a function of detuning 36
3.3 QD energy level structure at various field strengths 39
3.4 Simulated emission frequencies 41
3.5 Transition frequency separation as a function of detuning and Rabi frequency 42
3.6 Ground state precession spectrum as a function of Rabi frequency. . . . 44
3.7 Precession frequency magnitudes of the hole-like dressed state manifold at various magnetic field strengths and Rabi frequencies 47

4.1 Cryostat and sample preparation 50
4.2 Calibration of Attocube XYZ nanopositioners 51
4.3 Design of the magnet mounts 52
4.4 Simulation of the magnetic field mount 53
4.5 Schematic diagram of the laser setup. 55
4.6 Principle of operation of the Ti:Saph laser 56
4.7 Optical setup for probing single quantum dots 60
4.8 Photoluminescence spectra of a QD sample. 62
4.9 PL Decay profile of the neutral exciton 64

Declaration

I certify that this work contains no material which has been accepted for the award of any other degree or diploma in my name, in any university or other tertiary institution and, to the best of my knowledge and belief, contains no material previously published or written by another person, except where due reference has been made in the text. In addition, I certify that no part of this work will, in the future, be used in a submission in my name, for any other degree or diploma in any university or other tertiary institution without the prior approval of the University of Adelaide and where applicable, any partner institution responsible for the joint-award of this degree.

I give permission for the digital version of my thesis to be made available on the web, via the University's digital research repository, the Library Search and also through web search engines, unless permission has been granted by the University to restrict access for a period of time.

I acknowledge the support I have received for my research through the provision of an Australian Government Research Training Program Scholarship.

Josiah Ethan Hsi 29/9/2025

Acknowledgements

This MPhil thesis is the next step of a long journey that I began from childhood. It is an absolute privilege to be in this position, and I am indebted to everyone who have and continues to bless me with their support.

No amount of words can convey how grateful I am to my parents, who gave up their comfortable life in Singapore in pursuit of a better one for my sister and I here in Australia. To my father Tim, you've always encouraged me to be my best and are the rock of my life. To my mother Amy, your emotional support and grounding made me who I am today. To my sister Arabelle, your continuous support is such an inspiration to me. Thanks to my grandmother Esther, who's sacrificed so much for our family and has always been there for me. To my beautiful kitties Zuko and Suki who are the greatest joy of our home.

Thanks to my supervisors Glenn & Satya, you've been a great fount of knowledge and expertise and through you two together my cup runneth over. Glenn, thank you for your mentorship, guidance, and support throughout the entire master's process. Your infectious curiosity extends far beyond physics and was greatly enriching. Satya, thank you for your generosity and for teaching me everything you know. Being there while we built up the lab from scratch was an enlightening process. From fibre coupling to huge setups, look how far we've come.

To my comrades in the group, it has been an honour to be working and growing alongside you. A big thank you to Jacob, Nicole, Declan, Tom, Harry, Lucy, Sangeet, Mikhail, and Jamie. Special thanks to Nicole and Declan, we were the first students here and your company in those early days meant the world. Tim and Sammi, though you've moved on for greater things your presence shaped the DNA of this group and we're eternally grateful.

To my friends. We've been though six years of university from undergrad until now, and I'm so incredibly excited to see what's in store for us next. In particular, thank you so much to Julia, Jacob, Maddy, Georgia, Mitchell, Nick, and Indi. Your friendship means the whole world to me and seen me through some of the hardest times. To Dean, Justin, Josh, Shi Yang, and Yun Fang, we've basically been through war together and

I couldn't have done it without you guys.

Big thanks to the baristas in and out of campus, you kept us awake and alive in the long days.

On to the next adventure!

Abstract

The coherent control of carrier spin states in semiconductor quantum dots (QDs) is a key requirement for certain quantum information applications, particularly where light-matter interactions are involved such as in the generation of spin-photon entangled states. A widely used approach for spin control involves Larmor precession in an externally applied magnetic field. Increasing the magnetic field strength enhances the spin precession rate, thus improving the photon generation rate. However, this also introduces Zeeman splitting, which lifts the spin-state degeneracy. As a result frequency distinguishability is introduced, reducing the fidelity of the entangled spin-photon states.

This work explores a novel approach to mitigate the Zeeman splitting by employing the AC Stark effect via a red-detuned laser. The Stark shift counteracts the Zeeman energy difference, effectively restoring transition degeneracy within the transition linewidth while allowing for an increased magnetic field strength and consequently a faster precession rate. Theoretical modelling demonstrates that this technique enables an almost doubling of the current spin precession frequency while maintaining nearly degenerate optical transitions. To validate this approach, a high-precision optical system is under development to probe QD emission under simultaneous magnetic and optical fields. Simulations incorporating both effects confirm the feasibility of this method for eliminating frequency distinguishability. These results lay the groundwork for the development of scalable quantum dot-based photonic platforms for quantum communication and information processing.

Chapter 1

Introduction

The push in the development of modern quantum technologies have only grown stronger from its conception over 40 years ago, where the concept of a quantum computer was first described [1]. Emerging quantum technologies promise absolute secure communications, simulation of complex systems [2, 3], and metrology with sensitivities beyond the classical limit [4]. With the world's heavy reliance on digital communication, establishment of guaranteed secure communication channels are crucial to meet modern and emerging cybersecurity challenges. Additionally, wide scale infrastructure supporting the distribution and analysis of quantum information may emerge in a "quantum internet" [5].

Crucial to these technologies is the production of entangled quantum states, which are used as a resource for the distribution and processing of quantum information. Among the variety of quantum states explored, single photons of light show the most promise as a medium for the distribution of quantum information. Photons travel at the speed of light, the fastest data transmission speeds possible. The weak interaction strength of individual photons with the environment allows for retention of their quantum coherence properties for an extended duration of time. These properties, along with their ability to be entangled with a wide variety of quantum objects, are thus very attractive for single photons to be the workhorse of emerging quantum technologies.

Among the many systems under development for the production of entangled quantum states of light, semiconductor quantum dots (QDs) are the platform of choice for this work due to their properties as a deterministic source of single photons [6]. The 3-dimensional potential barriers that define a QD allow only for discrete energies levels of charge carriers, where carrier recombination within the dot produces a single photon of well-defined energy. Furthermore, semiconductor QDs benefit well from mature commercial semiconductor fabrication techniques, allowing for the engineering of sophisticated devices around QDs. In-situ optical microcavities enhance the single-photon collection efficiency by improving emission into preferred direction modes [7], and QDs embedded in on-chip photonic circuits show promise as the basis for quantum

information processing units [8]. Substantial work has been performed in the production of non-classical light in QDs ranging from single photons [7], entangled photon pairs [9], and entangled clusters of photons [10]. Such states are of interest in the encoding and transmission of quantum information, and in the case of entangled cluster states, their potential resilience against errors and losses whilst in transmission [11, 12].

One way to generate chains of entangled photons is through the Lindner & Rudolph protocol, where the spin state of confined charge carriers such as electrons or holes are coherently manipulated [13]. This protocol uses the spin precession of a confined charge carrier about an externally applied magnetic field to generate spin-photon entangled states, with repetitions of the above process resulting in chains of polarisation entangled photons. The rate of entangled photon production with this protocol is tied to the precession rate of the spins, which scales with the magnetic field strength. While increasing the magnetic field enhances production rates, the resulting Zeeman effect introduces energy shifts between polarization states, imposing a practical limit on field strength. This shift diminishes the degree of entanglement between the photon states, as which-path information about the polarisation state becomes accessible through the additional energy degree of freedom. To overcome this limitation and increase the production rate of entangled photons, this work introduces the use of a red-detuned laser to induce the AC Stark effect by dressing the transition between the excited and spin ground states. The AC Stark effect shifts the transition energies of the two polarizations at distinct rates, determined by the frequency detuning of the laser relative to each transition. As the laser power increases, these energy shifts reduce the separation between the transitions, eventually bringing them nearly degenerate within the transition linewidth. This convergence effectively eliminates the frequency information from the system, enabling increased entangled state production rates even at higher magnetic fields.

This thesis will document a theoretical investigation of the combined magnetic field and AC Stark field, and progress towards an experimental realisation of the combined effects. A portion of the experimental progress will detail the establishment of a new optical laboratory as part of this work. The thesis is outlined as follows:

Chapter 2: Background and fundamentals. This section covers the basics of quantum information, semiconductor quantum dots, and outlines efforts to producing a variety of entangled states through quantum dots. A key part of the work, the Lindner and Rudolph protocol, is discussed.

Chapter 3: A comprehensive simulation of the system of interest is covered. The simultaneous application of a magnetic field and AC Stark laser is covered, with its effects on the energy levels, selection rules, and precession rates discussed.

Chapter 4: Experimental progress towards observation of the simultaneous effects and generation of entangled states with a semiconductor quantum dot. This chapter outlines the experimental systems and calibrations developed as part of this work.

Chapter 5: Summary and outlook. A comprehensive summary of the key findings and contributions of the work is presented, as well as an outline of potential further objectives and goals that build on this work.

Chapter 2

Theoretical background

2.1 Foundations of quantum technologies

2.1.1 Historical context

In the 1970s and 1980s, interest in applying the principles of quantum mechanics and entanglement to practical problems began to take shape, particularly in the realms of information theory and computing. Classical foundations such as Claude Shannon's theories on quantification of information and transmission [14], as well as Alan Turing's concept of the universal Turing machine as an idealised computer [15], became pivotal frameworks for exploring quantum applications. Benioff introduced the first quantum model of a Turing machine in 1980 [1], and Deutsch later proposed the universal quantum computer as a counterpart to the classical Turing machine in 1985 [16]. Great progress in the field came from the establishment of algorithms for the solution of problems intractable to classical computation, a famous example is Shor's algorithm for solving discrete logarithms and the factoring of large numbers [17].

Parallel to the development of quantum computation was quantum information theory, developed with ideas from Holevo [18] and Ingarden [19], which generalised Shannon's theory to the quantum case. Schumacher then extended the concept of bits as the fundamental unit of information to quantum bits, coining the term "qubits" in 1985 [20]. Since then, these concepts have evolved significantly, positioning quantum computing and technology at the cutting edge of modern research. Today, companies like IBM [21] and Google [22] are leading the charge, exemplified by their development of superconducting processors on the order of hundreds of logical qubits.

2.1.2 Quantum bits

The qubit sits at the core of all quantum technologies. Unlike a classical bit that holds only two possible states, 0 or 1, quantum mechanics allows qubits to take intermediate

states described as a superposition of both $|0\rangle$ and $|1\rangle$. Here the ket notation $|\psi\rangle$ denotes a vector in the state space of the qubit. A general quantum state is described as:

$$|\psi\rangle = \alpha\,|0\rangle + \beta\,|1\rangle \tag{2.1}$$

where $\{\alpha, \beta\}$ are interpreted as the probability amplitudes of each state, satisfying the normalisation condition $|\alpha|^2 + |\beta|^2 = 1$. This leads to the interpretation of $|\alpha|^2$ as the probability of the state being in $|0\rangle$ when measured and $|\beta|^2$ as the probability for $|1\rangle$. An alternative expression for a general qubit state can be written as $|\psi\rangle = \cos(\theta/2)\,|0\rangle + e^{i\phi}\sin(\theta/2)\,|1\rangle$, with parameters $\theta \in [0, \pi], \phi \in [0, 2\pi)$. This allows for the mapping of a qubit to the surface of a unit sphere, with the azimuth and altitude angles corresponding to the parameters θ and ϕ as shown in Figure 2.1. A superposition state written as $|\psi\rangle = |0\rangle + e^{i\phi}\,|1\rangle$ would lie on the equator of the sphere with azimuthal angle ϕ. Implementations of qubits encode the logical 0 and 1 states onto certain physical states, such as the left and right circular polarisations of photons or the spin up/down states of spin $\frac{1}{2}$ states. While pure states represent systems in

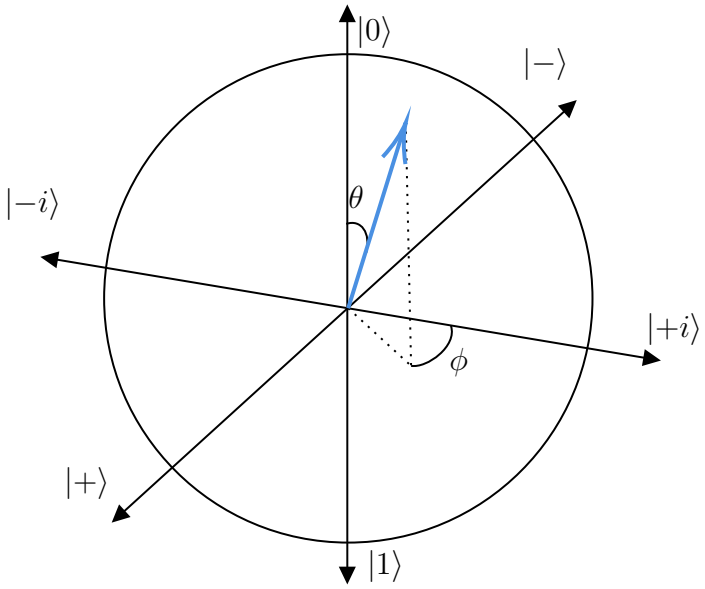


Figure 2.1: **Bloch sphere representation of a qubit.** The $|0\rangle$ and $|1\rangle$ states are mapped to the north and south poles of the sphere respectively, while a general state is represented as a point (blue arrow) on the surface of the unit sphere and is parametrised by θ and ϕ.

a well-defined quantum state, mixed states describe statistical ensembles of different quantum states, where the system is not known to be in any one specific state but instead existing as a probabilistic mixture. Mixed states, which must be represented by density matrices rather than state vectors, arise in scenarios involving decoherence

or incomplete knowledge of the system. This loss of coherence, often arising from interactions with an external environment, reduces the ability of mixed states to exhibit purely quantum phenomena such as superposition, making them an intermediate case between classical and fully quantum behaviour. Mixed states are mathematically represented using density matrices, which generalise the description of quantum objects beyond the vector or pure state representation. For a qubit or two level system, a general quantum state is written as $|\psi\rangle = a|0\rangle + b|1\rangle$. The corresponding density matrix is:

$$\begin{aligned}\rho &= |\psi\rangle\langle\psi| \\ &= (a|0\rangle + b|1\rangle)(a^*\langle 0| + b^*\langle 1|) \\ &= |a|^2|0\rangle\langle 0| + ab^*|0\rangle\langle 1| + a^*b|1\rangle\langle 0| + |b|^2|1\rangle\langle 1|\end{aligned} \tag{2.2}$$

The matrix elements of this density matrix is thus:

$$\rho = \begin{pmatrix} |a|^2 & ab^* \\ a^*b & |b|^2 \end{pmatrix} \tag{2.3}$$

The diagonal elements are the populations in each state, while the off-diagonal elements are defined as the coherences of the state. An equal statistical mixture of $|0\rangle$ and $|1\rangle$ states in a statistical ensemble has the corresponding density matrix:

$$\rho = \frac{1}{2}\begin{pmatrix} 1 & 0 \\ 0 & 1 \end{pmatrix} \tag{2.4}$$

While a quantum superposition of $|0\rangle$ and $|1\rangle$ states has the density matrix:

$$\rho = \frac{1}{2}\begin{pmatrix} 1 & 1 \\ 1 & 1 \end{pmatrix} \tag{2.5}$$

The "purity" of the density state, a measure of the degree of mixing in the state, is defined as $\mathrm{Tr}\{\rho^2\}$ and ranges from 0 to 1. The mixed state (Eq 2.4) has purity 0, while the pure state (Eq 2.5) has purity 1. In general, the density matrix of a pure state is defined as:

$$\rho = \sum_i P_i |\psi_i\rangle\langle\psi_i| \tag{2.6}$$

Where P_i is the probability of observing the population in each pure state $|\psi_i\rangle$. Measuring the state of the qubit in a certain basis can be visualised on the Bloch sphere as projecting the state onto one of the 3 axes. The Bloch sphere picture serves as a visualisation of qubit dynamics or operators performed on the qubit, as often encountered in quantum information theory. Picking the logical basis $|0\rangle, |1\rangle$ to measure the state in results in either reading out $|0\rangle$, with probability $|\alpha|^2$, or $|1\rangle$ with probability $|\beta|^2$. In the Bloch sphere, picking the logical basis is equivalent to choosing the z-axis

to measure the state in, which projects the state to either the north or south pole. An alternative basis can be defined as $|\pm\rangle = |0\rangle \pm |1\rangle$ corresponding to the y axis, or $|\pm i\rangle = |0\rangle \pm i\,|1\rangle$ corresponding to the x axis. In the case of photon polarisation, these basis states map to the R/L circular, horizontal/vertical, and diagonal/anti-diagonal polarisation bases. A mixed state in comparison is represented as a point in the interior of the sphere instead of the surface.

2.1.3 Entanglement

Entanglement can be defined as a non-classical correlation between two or more quantum objects such as qubits, where under entanglement such objects can only be described by a single joint quantum state and cannot be separated into two individual quantum states. To illustrate this, consider a superposition of the four possible states two qubits may take:

$$|\psi\rangle = \frac{1}{\sqrt{4}}\big(\,|0\rangle_A\,|0\rangle_B + |0\rangle_A\,|1\rangle_B + |1\rangle_A\,|0\rangle_B + |1\rangle_A\,|1\rangle_B\,\big) \tag{2.7}$$

This state can be decomposed into a separate product of two qubits:

$$|\psi\rangle = \frac{1}{\sqrt{2}}\big(\,|0\rangle + |1\rangle\,\big)_A \otimes \frac{1}{\sqrt{2}}\big(\,|0\rangle + |1\rangle\,\big)_B \tag{2.8}$$

The two qubits are not entangled, as the joint quantum state can be written as a mixture of the A and B states separated by the tensor product $\otimes$. In this work the "multiplication" of kets implies the tensor product between states. Measuring the state of one qubit does not give information about the state of the other qubit. In contrast, one example of an entangled state of two qubits are given by the Bell states:

$$\begin{aligned} \big|\psi^{\pm}\big\rangle &= \frac{1}{\sqrt{2}}(|0\rangle_A\,|1\rangle_B \pm |1\rangle_A\,|0\rangle_B) \\ \big|\phi^{\pm}\big\rangle &= \frac{1}{\sqrt{2}}(|0\rangle_A\,|0\rangle_B \pm |1\rangle_A\,|1\rangle_B) \end{aligned} \tag{2.9}$$

In this case, a measurement of one qubit immediately gives knowledge of the state of the other qubit without having to make a measurement of the other. Unlike classical correlations, entanglement is basis independent. Choosing a different basis for measurements still leads to correlations between the qubits. As an example, the Bell state $|\psi\rangle = 1/\sqrt{2}\big(\,|0\rangle_A\,|1\rangle_B + |1\rangle_A\,|0\rangle_B\,\big)$ written in the $|\pm\rangle = |0\rangle \pm |1\rangle$ basis still retains the correlation between qubits A and B:

$$|\psi\rangle = \frac{1}{\sqrt{2}}\big(\,|+\rangle_A\,|+\rangle_B + |-\rangle_A\,|-\rangle_B\,\big) \tag{2.10}$$

The density matrix representation of the two qubit state is used to classify the degree of entanglement between two qubits. Following the steps of Equation 2.2, the density matrix of the superposition state (Eq. 2.7) is:

$$\rho_{\text{superposition}} = \frac{1}{4}\begin{pmatrix} 1 & 1 & 1 & 1 \\ 1 & 1 & 1 & 1 \\ 1 & 1 & 1 & 1 \\ 1 & 1 & 1 & 1 \end{pmatrix} \tag{2.11}$$

Where the rows correspond to the states $|0\rangle_A |0\rangle_B, |0\rangle_A |1\rangle_B, |1\rangle_A |0\rangle_B, |1\rangle_A |1\rangle_B$. The density matrix of the Bell state $|\psi\rangle = 1/\sqrt{2}\big(|0\rangle_A |1\rangle_B + |1\rangle_A |0\rangle_B\big)$ on the other hand is written as:

$$\rho_{\text{Bell}} = \frac{1}{2}\begin{pmatrix} 0 & 0 & 0 & 0 \\ 0 & 1 & 1 & 0 \\ 0 & 1 & 1 & 0 \\ 0 & 0 & 0 & 0 \end{pmatrix} \tag{2.12}$$

One measure of entanglement between states among many is the concurrence [23]:

$$\mathcal{C}(\rho) = \max(0, \lambda_1 - \lambda_2 - \lambda_3 - \lambda_4) \tag{2.13}$$

Where λ_i are the eigenvalues of the matrix $\rho\tilde{\rho}$, with $\tilde{\rho}$ defined as $(\sigma_y \otimes \sigma_y)\rho(\sigma_y \otimes \sigma_y)$ for Pauli matrix σ_y. The concurrence of the superposition state is 0, while the concurrence of the Bell state is 1. This illustrates the difference in entanglement between the two states.

2.1.4 Multi-partite entangled states

Entanglement between more than two qubits, or multi-partite entangled states, has found interest for a range of quantum information applications. A wide range of multi-partite states have been formulated, each with a variety of features and characteristics. Of specific interest to this work are cluster states, where the overall quantum state can be described as a mathematical lattice, with vertices representing the qubits and edges as a quantum operator between the two linked qubits [24]. A special case of a cluster state is for N=3 qubits, where the state is written as $|\psi\rangle = \frac{1}{\sqrt{2}}\big(|{+}0{+}\rangle + |{-}1{-}\rangle\big)$. This state is local unitary equivalent to the GHZ state $|GHZ\rangle = \frac{1}{\sqrt{2}}(|000\rangle + |111\rangle$, a three-qubit entangled state which has been used as a platform for a range of quantum communication protocols [25]. Local unitary equivalence, i.e. the two states can be transformed into each other with single qubit rotations [26], allows the N=3 cluster state to benefit from the the same error correcting codes as the GHZ state when used for quantum information applications [23].

Cluster states have found use as the foundation for measurement-based quantum computing (MBQC), an alternative to the more common gate-based quantum computing architecture, and in quantum error correction schemes [27, 28]. The measurement-based quantum computing architecture is particularly suited for photonic implementations of quantum computing and communication due to the ease of creating photons entangled with each other through certain single-photon emitters. Furthermore, two-photon interference for controlled gate operations are difficult to perform in a gate-based architecture, while photon measurements are simpler to achieve in MBQC [29].

N-dimensional cluster states are particularly significant as the measurement of one qubit in the lattice does not necessarily remove the entanglement from the entire system, but results in a new graph state [27]. The entanglement property is especially robust in cluster states of dimension $d > 2$ [11], potentially enabling long range quantum communication protocols that are resilient to losses in optical fibres. A source of high-dimensional, scalable photonic cluster states is therefore highly desirable, and is the topic of investigation in this work.

2.2 Single photon sources

A range of materials and sources have been utilised in the literature for the generation of single as well as entangled photons. Single photon sources generally fall within one of two groups. Photonic engineered sources generally rely on a non-linear optical effect such as spontaneous parametric down-conversion. The second method utilises the transition of an excited energy state to a lower energy state of a physical emitter, resulting in an emitted photon with frequency equal to the transition energy. This section will discuss the key figures of merit characterising single photon sources, along with briefly covering the various devices and methods used in the literature to generate single photons.

When considering single photon sources, the main figures of merit are the single photon purity, photon indistinguishability, and source brightness [6, 30, 31]. Single photon purity is quantified through the second-order coherence $g^{(2)}(t)$, which is measured through the Hanbury-Brown and Twiss (HBT) experiment [32] as depicted in Figure 2.3a. The second-order correlation function, also known as the intensity autocorrelation function, is written for two ideal photon number resolving detectors (Fig. 2.3a):

$$g^{(2)}(\tau) = \frac{\langle n_1(0) n_2(\tau) \rangle}{\langle n_1(0) \rangle \langle n_2(\tau) \rangle} \tag{2.14}$$

where $n_i(t)$ is the number of photons incident on detector $i = 1, 2$ at times $t_{1,2}$, with the relative time delay between clicks on each detector $\tau = t_1 - t_2$. Measurement of the correlation function behaviour at zero time delay reveals properties of the incident

light, as depicted in Figure 2.2. A second-order correlation measurement of $g^{(2)}(0) < 1$ is a key indicator of photon anti-bunching, where photons arrive one at a time within a given time bin. The simultaneous detection of a photon on each detector is described as

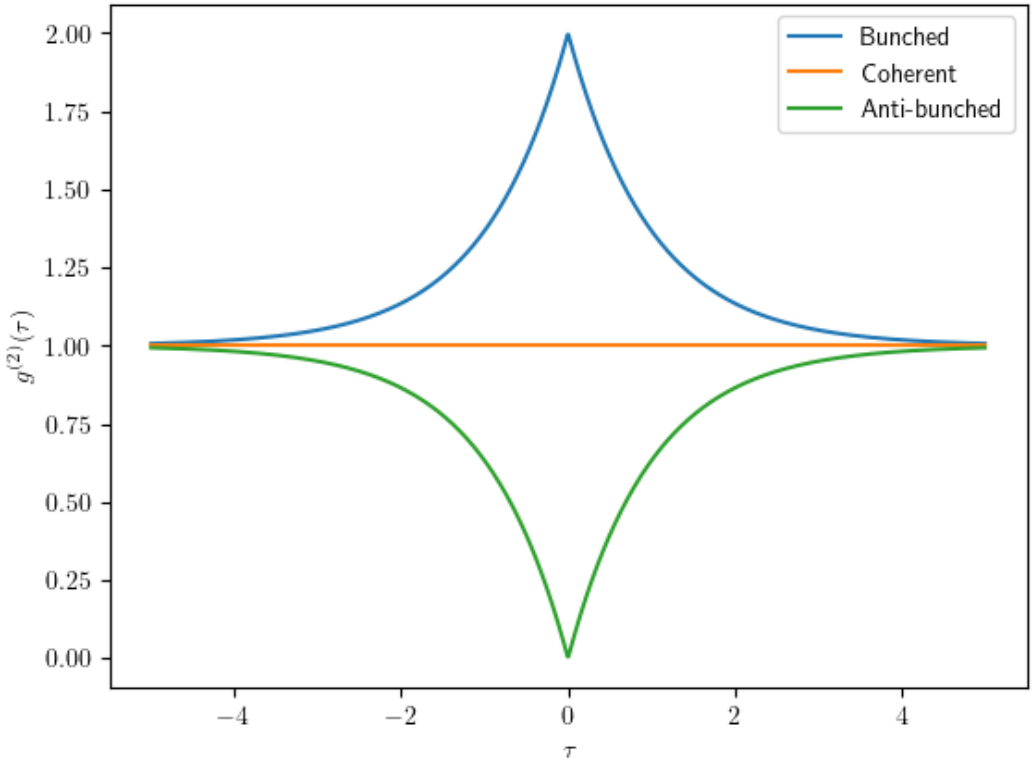


Figure 2.2: **Second order correlation function for various light sources.** A thermal light source such as a black body emitter results in a factor of $g^{(2)}(0) > 1$ (blue trace), where multiple photons are present in the same time bins known as photon bunching. A coherent source for example from a laser has a flat factor $g^{(2)}(0) = 1$ (yellow), exhibiting Poissonian statistics. A single-photon source has one or zero photons per time bin, resulting in a factor of $g^{(2)} < 1$ (green) and displaying photon anti-bunching.

an event at $\tau = 0$. As such, the second-order correlation at $\tau = 0$ serves as an indicator of the number of photons in the photon state incident on the beam splitter. If a single photon (Fock state $|1\rangle$) is incident on the beam splitter, there is zero probability of detection from both detectors, resulting in a result of $g^{(2)}(0) = 0$. In practice, non-ideal detectors, imperfect single photon sources, and other experimental factors reduce the measured single photon purity.

A localised single photon wavepacket produced in discrete time and discrete volume by a physical emitter may be described as a superposition of pure plane waves with

frequency mode $|\omega\rangle$[1]:

$$|1\rangle = \sum_{n,\omega} c_n |\omega\rangle \tag{2.15}$$

Two photons are indistinguishable when the superposition coefficients of two separate photon wavepackets are identical. This is measured through the Hong-Ou-Mandel (HOM) experiment (Fig. 2.3b), which is based on a balanced Mach-Zender interferometer [33]. In the HOM experiment, two localised photons described by Equation 2.15 are incident on separate 50/50 beamsplitter inputs (A and B, as depicted in Figure 2.3b). For beamsplitter reflection and transmission coefficients r_i, t_i for inputs $i = A, B$, the resulting state is described as a superposition of possible results from beamsplitter outputs C and D:

$$|\text{out}\rangle = r_B t_A |2\rangle_C |0\rangle_D + t_b r_A |0\rangle_C |2\rangle_D + t_A t_B |1\rangle_C |1\rangle_D + r_A r_B |1\rangle_C |1\rangle_D \tag{2.16}$$

For a 50/50 beamsplitter, the reflection and transmission coefficients are $r = \frac{i}{\sqrt{2}}$, $t = \frac{1}{\sqrt{2}}$. Given indistinguishable photons, the output states $|1\rangle_C$ and $|1\rangle_D$ are identical and symmetric under interchange, resulting in the cancellation of the two states $t_A t_B |1\rangle_C |1\rangle_D + r_A r_B |1\rangle_C |1\rangle_D = 0$. The final state at the output ports of the beamsplitter is thus:

$$|\text{out}\rangle = \frac{1}{\sqrt{2}}\Big(|2\rangle_C |0\rangle_D + |0\rangle_C |2\rangle_D \Big) \tag{2.17}$$

The final result for indistinguishable photons is an equal probability of two photons exiting output C or output D, and zero probability of one photon each exiting one output. By placing time-resolved single photon detectors on the outputs of the beamsplitter, a HBT-like measurement can be conducted to determine the photon indistinguishability by measuring the zero-time-delay intensity. However any distinguishability between photons, either through polarisation, wavepacket shape, or other features, will result in the equal likelihood of simultaneous detection of photons on each detector.

The brightness of a source is determined through the highest possible single photon production rate, which directly influences the operation speed of various communication or computation protocols. Single photon sources based on non-linear processes produce single photons randomly, and generally have low single photon production rates. Physical emitter single photon sources on the other hand can produce photons "on-demand" compared to non-linear sources, where one excitation pulse generally results in one emitted photon neglecting any extenuating factors. Several factors limit the photon production rates in state-excitation based architectures, including finite excitation and decay time.

With the knowledge of what makes a single photon source, the remaining part of this section will discuss the various single photon devices that have been developed in

[1]Such frequency modes arise from quantizing the EM field, with a single excitation of a given frequency mode ω written as a Fock state $|1_\omega\rangle$.

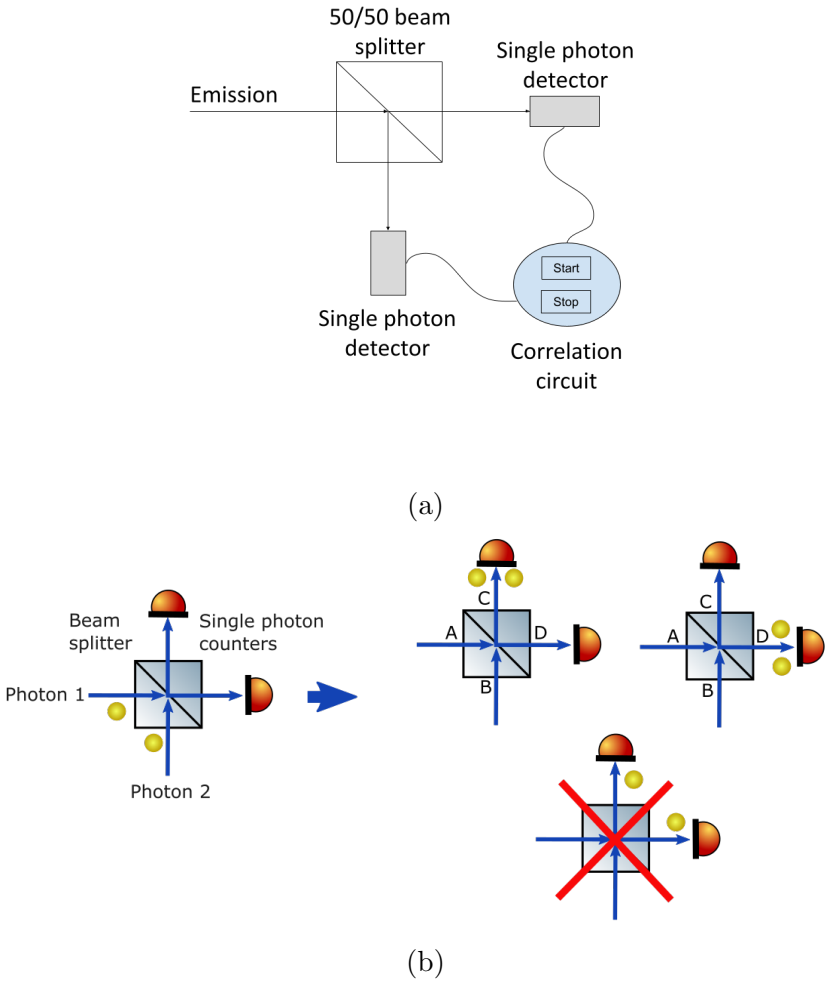


Figure 2.3: **Experimental schematics for measuring single photon properties.** (a) Hanbury-Brown and Twiss experiment for measuring the second-order coherence of a photon source. (b) Possible outcomes of a Hong-Ou-Mandel experiment for two identical photons incident on separate inputs of a beamsplitter.

parallel over the past forty years. Such devices, on top of being able to produce single photons, have been developed as part of a greater effort to realising the broad quantum technology challenges of quantum computation, communication, and simulation. A brief overview of the more common single photon architectures is provided in table 2.1, outlining the main single photon figures of merit.

The single photon workhorse of a large majority of quantum optics experiments is the spontaneous parametric down-conversion (SPDC) mechanism [47], where photons incident on a material with significant non-linearity[2] undergo frequency down-

[2]Non-linear materials have non-zero higher order electric susceptibilities, defined with regard to

Platform	Production rates	$G^{(2)}(0)$	Indistinguishability
SPDC	4.4 MHz [34]	0.004 [35]	0.96 [36]
Atoms	8.1 MHz [37]	0.002 [38]	0.98 [39]
NV Centres	5 MHz [40]	0.003 [40]	0.9 [41]
2D materials	82 MHz [42]	0.09 [43]	0.56 [44]
Semconductor QDs	1 GHz [45]	0.003 [46]	0.996 [46]

Table 2.1: **Single photon performance figures of merit for selected platforms in the current literature.**

conversion. This results in the production of two photons with half the frequency of the original photon, combined momenta equal to the original photon, and entangled in their polarisation degree of freedom. Single photons created through SPDC are heralded, where detection of one of the generated photons are used to signal the presence of the second photon on the other path. Spontaneous four-wave mixing is another non-linear process for the generation of correlated pairs of single photons, where two photon beams intersect in a non-linear material. With the right phase matched conditions, two separate photons are produced with total energy equal to the sum of the two incoming photon energies. Single photons from non-linear sources follow a thermal emission profile, with the probability of generating multiple photons in a single path increasing with pump intensity [30]. To avoid multi-photon events, the pump intensity must remain low, which limits the single-photon generation rate to reported values between tens of kHz and 4.4 MHz.[48, 49, 34, 50]. While SPDC sources remain popular due to the simplicity of the required materials, the non-deterministic generation can be undesirable for certain quantum information applications due to the limited clock rates. Devices based on the excitation-decay cycle of a two level system hold the advantage in this regard, with such architectures potentially achieving very high photon production efficiencies for a single excitation pulse.

Single photons from the relaxation of an excited state was first observed in atomic systems, where a beam of sodium ions crossing the path of a laser tuned to resonance exhibited single photon emission [51]. Since then, a wide range of atomic systems been developed for the production of quantum information devices. Current efforts focus on trapped atomic systems, commonly rare earth ions such as rubidium and yttrium, for both single and entangled photon production along with applications such as quantum computing [52] and simulation [53]. Atom traps suspend single atoms or ions in an ultra-high vacuum chamber, which confers a high resistance to environmental decoherence and allowing for large numbers of quantum operations within the coherence

the material's dielectric polarisation density $\mathbf{P} = \epsilon_0\big(\chi^{(1)}\mathbf{E}(t) + \chi^{(2)}\mathbf{E}(t) + \cdots\big)$. The higher order susceptibilities are the coefficients $\chi^{(n)}$ for $n > 1$.

time [54]. The trade-off for such a system is the high level of complexity required to trap small numbers of atoms, limiting the scalability of this architecture for the production of single photons and quantum communication devices. Trapped ions however show great promise for other applications such as simulation of complex molecular systems and computation [55, 54].

Solid state photon sources are the largest class of single photon sources, with a wide range of materials, geometries, and sizes. Such emitters are larger than single atoms, which allow for higher potential scalability and integration into more sophisticated devices [56, 31]. Although numerous platforms have been developed, this section will focus on those most frequently discussed in the literature. These include defect states in bulk crystal and two-dimensional materials, along with semiconductor quantum dots. Point defects in bulk crystals are any imperfections in the crystalline structure such as vacancies (empty sites) and atomic substitutions in the native crystal site. The nitrogen-vacancy (NV) and silicon-vacancy centres in diamond are some of the most prominent single photon emitters with substantial research towards development and integration into quantum devices [57]. Such platforms are resilient against temperature induced decoherence up to room temperature [58] and confer long spin coherence times to up milliseconds. This makes such defect centres attractive for quantum devices that operate in ambient temperatures without further cryogenic cooling systems. Substantial work has been invested towards the integration of diamond based defects into broader quantum devices such as diode structures [59] and integrated waveguides [60]. However, NV centres have long radiative times on the order of tens of nanoseconds [31] which places the single photon generation rate to around 5 MHz [40, 61].

Two-dimensional (2D) materials such as hexagonal boron nitride (h-BN) and tungsten diselenide have been identified as hosts for single photon emitters. Such materials, also known as van der Waals materials, consist of individual atomic layers which exhibit unique properties when stacked. Similar to NV defects, single photon emitters in h-BN are associated with defect states within the bandgap and exhibit single photon production at room temperature [62, 63] at megahertz rates [64]. However, the physical composition of these optically active defects continue to be a matter of debate [65, 66], and integration into photonic devices are in its infancy [67].

Semiconductor quantum dots, the platform of choice for this work, are regions of low bandgap material surrounded in 3 dimensions by a higher bandgap material. Such regions are on the scale of tens of nanometres, encompassing tens of thousands of individual atoms. As the size of the structure is comparable to their De Broglie wavelength, charge carriers such as electrons and holes within the QD are confined to discrete energy levels, a behaviour similar to atomic states. The lesser bandgap region forms a 3D potential well, limiting the density of states within the dot to those of definite energy. QDs typically exhibit fast single photon generation rates of GHz from a fast radiative lifetime [45, 68]. Such properties along with high single photon indis-

tinguishability [46] make semiconductor QDs attractive for integration into quantum photonic devices. Consequently, the subsequent section will outline in greater detail the assembly, structure and single photon production mechanisms of semiconductor quantum dots.

2.3 Semiconductor quantum dots

Semiconductor QDs are typically grown through molecular beam epitaxy, where semiconductor materials are deposited onto the wafer substrate with the precision of single atomic layers at a time. Tight control of the semiconductor deposition rate, temperature, pressure, and material choice facilitates the formation of localised 3D regions that become quantum dots when covered with higher bandgap material. The first QDs were produced through the Stranski-Krastonov method [69], where InAs deposited onto a GaAs substrate causes strain to build up due to a 7% lattice constant mismatch. The strain energy is minimised by the formation of lens-shaped InAs islands with a height of 1-2 monolayers. Deposition of GaAs above the InAs islands completes the QD. Due to the self-assembled nature of these QDs, the size, shape, and position are randomly distributed and often lack perfect cylindrical D_{2d} symmetry [70]. The reduced C_2 symmetry forming an ellipsoid affects the Coulomb exchange interaction between the electron and hole states within the quantum dot, resulting in a fine-structure energy splitting in the recombination of electrons and holes [71]. This fine-structure splitting manifests as a distinctive energy difference between the H/V polarisations of emitted photons (see Section 2.4), and is undesirable in the production of entangled photon pairs thus leading to the exploration of alternative quantum dot growth methods.

The QDs discussed here are grown through a more recent method; droplet etching epitaxy, where nanoholes are etched into an AlGaAs epitaxial layer by depositing droplets of aluminium [73]. Filling the holes with GaAs and capping with AlGaAs completes these QDs (Fig. 2.4), which exhibit significantly reduced strain from the two materials due to their similar lattice constant. Furthermore, such QDs are highly symmetric as compared to the self-assembled kind, greatly reducing the characteristic fine-structure splitting. This makes such QDs an ideal source of indistinguishable single photons, and as an entangled photon pair source [74]. The precise details of the growth process is outlined in the master's thesis of Declan Gossink [72].

2.3.1 Carrier states in quantum dots

Electrons and holes are the common mobile carriers in bulk semiconductors. Here, electrons with $m_s = \pm\frac{1}{2}$ spin reside in the conduction band, which is derived from an S-type atomic orbital with $m_l = 0$ orbital angular momentum. Holes with similar $m_s = \pm\frac{1}{2}$ spin reside in the valence band. This band is derived from P-type orbitals, which

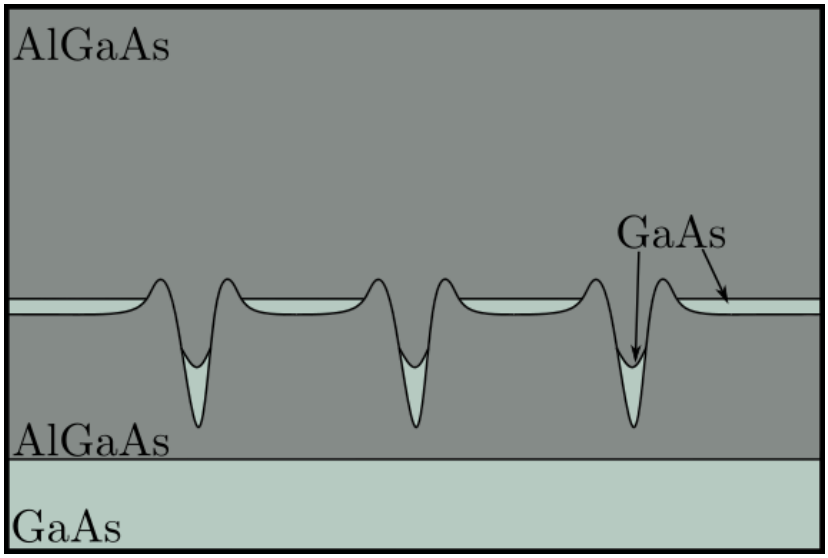


Figure 2.4: **Schematic of droplet etched epitaxial GaAs/AlGaAs quantum dots.** Figure originally from the thesis of Declan Gossink [72].

take orbital angular momentum values of $m_l = \pm 1, 0$. Each orbital spin corresponds to an initially degenerate band, which gets lifted through the spin-orbit interaction. This results in the $m_l = 0$ spin-orbit band shifting down in energy by $\Delta \approx O(100)$ meV, and can be ignored as the states are much higher in energy as compared to the other states. The remaining 4 states $|m_l, m_s\rangle = \left|\pm 1, \pm\frac{1}{2}\right\rangle$ are organised by the z projection of angular momentum. $m_j = m_l + m_s = \pm\frac{1}{2}$ states are denoted as the light holes, and $m_j = \pm\frac{3}{2}$ states denoted as heavy holes. Aside from angular momentum, the heavy and light holes have differing effective masses leading to the choice in nomenclature [75]. In a bulk III-V semiconductor as depicted in Figure 2.5, the heavy (HH) and light (LH) hole bands are degenerate at the $k = 0$ point. However when confined to a quantum dot with lengths $L_x, L_y >> L_z$ exhibiting D_{2d} symmetry, the HH and LH split in energy by tens of meV [71]. This leaves the HH as the lower energy state that is usually populated in the dot, and the LH can be ignored due to its higher energy apart from a negligible HH-LH mixing [76]. The heavy hole in a quantum dot thus acts as an effective two level system with angular momentum $m_j = \pm\frac{3}{2}$. In this chapter, the $+\frac{1}{2}$ and $-\frac{1}{2}$ electron states are denoted as $|\uparrow, \downarrow\rangle$, and heavy hole states as $|\Uparrow, \Downarrow\rangle$. In using QDs as a platform for quantum information applications, a range of confined states have been investigated and used as qubits including but not limited to the electron, hole, and dark exciton [77]. In this work, the confined hole is used where the $|\Uparrow\rangle, |\Downarrow\rangle$ states are associated with the logical $|0\rangle, |1\rangle$ states.

Mobile carriers in quantum-confined semiconductor structures consist of a family of quasi-particles known broadly as excitons. Quantum confined semiconductor

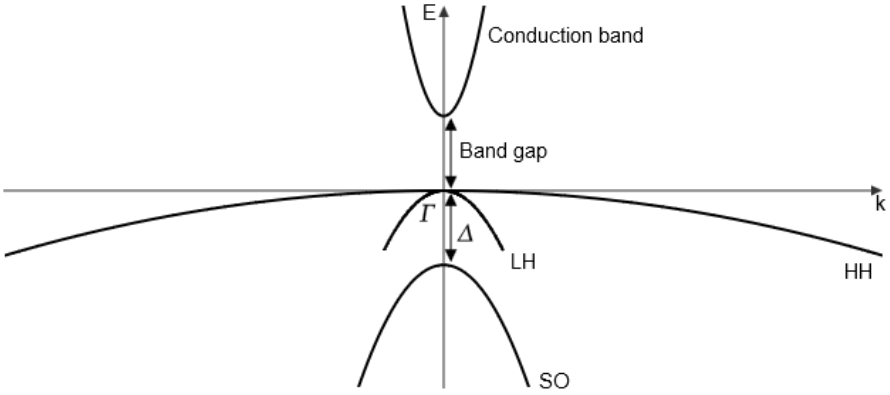


Figure 2.5: **Band structure of a III-V semiconductor around the Γ symmetry point.** HH and LH are the heavy and light hole bands, and SO is the split-off band.

structures, such as quantum wells and quantum dots, localise electrons and holes. This increases the likelihood of electron-hole quasi-particle formation known as excitons. These quasi-particles consist of various numbers of electrons and holes interacting through the standard Coulomb interaction as well as the exchange interaction. The usual Coulomb potential for two charges i, j is written as:

$$V_{i,j} = \frac{1}{4\pi\epsilon_0\epsilon_r}\frac{q_i q_j}{|r_i - r_j|} \tag{2.18}$$

Where ϵ_0 is the vacuum electric permittivity and ϵ_r is the material relative permittivity. For a hole and electron, the Coulomb and exchange interactions in materials like GaAs produces a binding energy of $\Delta E \approx O(1)$ meV, lowering the total energy when compared to the sum of their individual confinement energies. Additional confined electrons or holes produce a greater energy shift, resulting in discrete emission lines representing the family of excited states.

The exchange interaction arise from the Fermi statistics of electrons and holes, which due in QDs to their effective spin indistinguishability result in an additional energy shift dependent on the constituent spins. The short-range exchange Hamiltonian for a single hole with spin J_h and electron with spin S_e is written as [71]:

$$H_{\text{exch.}} = -\sum_{i=x,y,z}\left(a_i J_{h,i} S_{e,i} + b_i J_{h,i}^3 S_{e,i}\right) \tag{2.19}$$

Where the constants a, b relate to various physical properties of the QD such as geometry and rotational symmetry. Diagonalisation of this Hamiltonian for the neutral exciton leads to four different spin states depending on the z-axis spin projection of the constituent electron and hole $M = S_{e,z} + J_{h,z}$. A spin-aligned pair $|\uparrow\Uparrow\rangle, |\downarrow\Downarrow\rangle$ has an

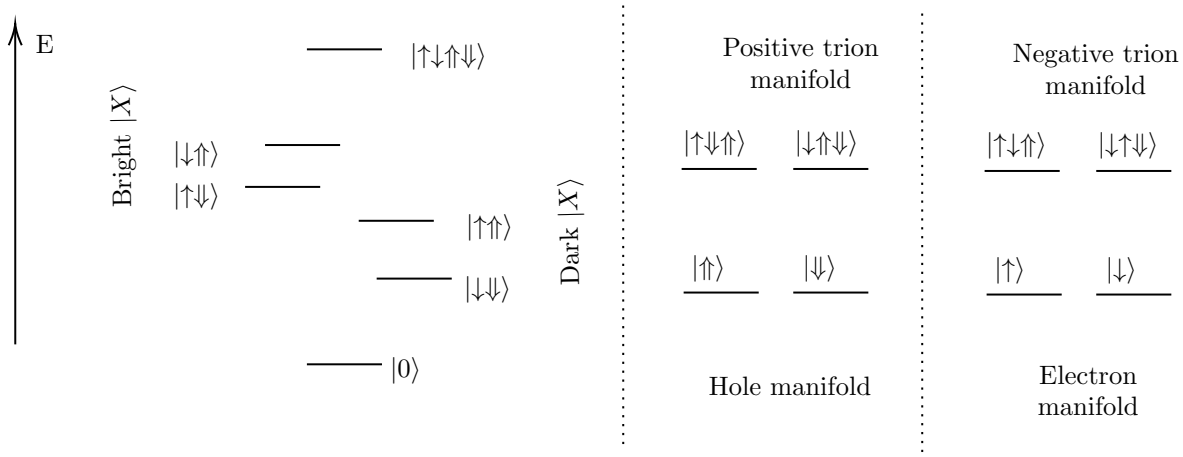


Figure 2.6: **Various exciton states of interest within a QD.** Energies of the states are depicted relative to other states in each section. The kets labelling each state illustrate the spin states of the constituent electrons and holes. $|0\rangle$ refers to the empty dot, with no electrons or holes present.

effective spin of ± 2, while an anti-aligned pair $|\uparrow\Downarrow\rangle, |\downarrow\Uparrow\rangle$ has an effective spin of ± 1. The ± 1 "bright exciton" states can be directly excited from the ground state (empty QD) with the absorption of a single photon. The excitation and decay of the ± 2 "dark exciton" states in comparison are electric dipole forbidden transitions, requiring a non-radiative or phonon assisted transition for a dark exciton to be produced.

Optical excitation of an additional spin anti-aligned electron-hole pair in the presence of a bright exciton produces the "biexciton" state, with two electrons and two holes in the ground state. The energy of the biexciton differs from two unpaired excitons due to the additional four particle Coulomb interactions. Excitation of an electron-hole pair in the presence of a single electron or hole in the QD results in the "charged" exciton, or trion, which can be positive or negative depending on the initial state. For the case of a postively charged trion, the two holes must be spin anti-aligned due to Hund's rule. This leads to an overall spin of $\pm\frac{1}{2}$ as determined by the individual electron. Similarly, a negatively charged trion has a spin of $\pm\frac{3}{2}$. A summary of the most common excitons present in QDs are depicted in Figure 2.6.

2.3.2 Decoherence mechanisms

The spin decoherence of the ground state is a major limitation to the production of entangled states in these QDs, as the spin transitions from a pure to a mixed state. Decoherence generally occurs when a quantum system interacts with its surrounding environment, causing a gradual loss of coherence over time due to these interactions. In a QD, the hyperfine interaction between the single electron spin and the surrounding

nuclear spin ensemble is a key contributor to spin decoherence. The Hamiltonian for the hyperfine interaction is defined from the Fermi contact interaction [78]:

$$H = \frac{8\pi}{3}\frac{\mu_0}{4\pi} g_0 \mu_B \sum_i \hbar \gamma_{n,i} \mathbf{S} \cdot \mathbf{I_i} \delta(\mathbf{r} - \mathbf{R}_i) \tag{2.20}$$

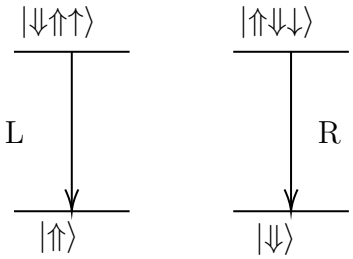
g_0 is the free electron g factor, μ_B is the Bohr magneton, i indexes the nucleus at each lattice point with position $\mathbf{R}_i$, $\gamma_{n,i}$ is the nuclear gyromagnetic ratio, and $\mathbf{S}, \mathbf{I}_i$ are the electron and nuclear spin operators respectively. From the Hamiltonian, the electron with wavefunction $\psi(\mathbf{r})$ and effective g factor g experiences an effective magnetic field, defined as the Overhauser field [79]:

$$\mathbf{B}_n = \frac{2\mu_0}{3}\frac{g_0}{g} \sum_i \hbar \gamma_{n,i} \mathbf{I}_i |\psi(\mathbf{R}_i)|^2 \tag{2.21}$$

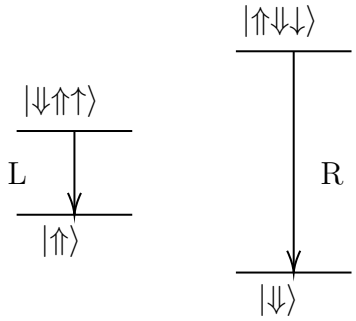
Here, the hyperfine interaction leads to decoherence through fluctuations in the effective magnetic field [80] arising from neighbouring nuclear dipole-dipole interactions, which also affect the emission spectrum of the dot through fluctuations in the Zeeman splitting from $\mathbf{B}_n$. Furthermore, the nuclear spins also precesses due to the magnetic field from the electron, with precession rates dependant on the distance from the electron. Larmor precession of the nuclear spin bath takes place on the orders of 1 microsecond, while the electron's Larmor precession is much faster than the nuclei on the orders of 10s of nanoseconds [81]. Additional dephasing takes place in the presence of a strong external magnetic field that is dominant over the nuclear Overhauser field. The applied field polarises and disperses the nuclear spin orientations similar to that of an NMR system, resulting in a bath of nuclear spins precessing around the applied magnetic field direction at different phases based on the local environment. This changes the direction of the electron's precession axis slightly, leading to a dephasing of the electron spin along the original z axis.

2.3.3 Optical selection rules

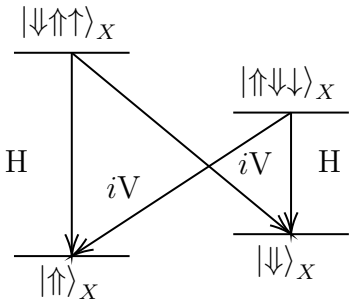
Optical transitions in the electric dipole approximation are constrained by the selection rules given by the spin angular momentum of the initial and final states. As the emitted or absorbed photon carries an angular momentum z-projection of $m_z = \pm 1$ corresponding to left and right circular polarisation, the initial and final states must differ by the same amount to conserve angular momentum. For example the recombination of the charge neutral $|X^{\pm}\rangle$ bright exciton to the ground (empty) state is optically allowed, with a spin z-projection of ± 1. Alternatively by examining the spin states of the constituent electron and hole, the recombination of the $\pm\frac{1}{2}$ electron with the $\mp\frac{3}{2}$ hole results in a net spin of ∓ 1, producing a left/right circularly polarised photon. Charged excitons follow the same selection rules, where a negative trion with $\pm\frac{3}{2}$ decays to a



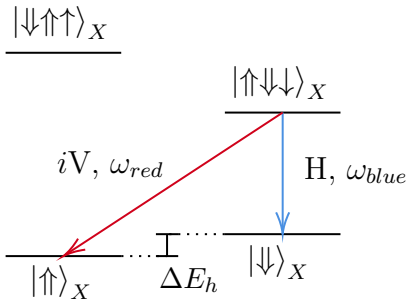
(a) Charged exciton energy level structure. Transitions between ground and excited states are spin-preserving, where the states are coupled with circularly polarised light [82].



(b) External magnetic field in the Faraday configuration aligned to z axis. Polarisation selection rules remain unchanged.



(c) External magnetic field in Voigt configuration aligned to x axis. Eigenstates of the system lie in the x direction. Excited states may decay to either ground state, emitting a horizontally polarised photon.



(d) Lambda system as a candidate for the generation of spin-photon entangled states. The Zeeman effect shifts transition energies between H and V polarisation states.

Figure 2.7: **Positively charged exciton complex in the presence of magnetic fields with different orientations.**

single electron with spin $\pm\frac{1}{2}$ and emits a R/L circularly polarised photon as illustrated in Figure 2.7a. Spin non-conserving transitions $|\uparrow\downarrow\Uparrow\rangle \leftrightarrow |\downarrow\rangle$,$|\downarrow\uparrow\Downarrow\rangle \leftrightarrow |\uparrow\rangle$ are electric dipole forbidden due to an angular momentum difference of ± 2. Multipole transitions may allow this transition, however such probabilities are insignificant compared to the electric dipole transition and can be neglected.

Selection rules in the presence of magnetic fields

Applying an external magnetic field $\vec{B}$ to the quantum dot modifies the energy manifold and selection rules of the trion, and the nominally degenerate excited trion spin states are lifted along with the ground spin states. The Hamiltonian governing the spin-

magnetic field interaction is written as:

$$H = g\mu_B \vec{S} \cdot \vec{B} \tag{2.22}$$

$\mu_B = \frac{q\hbar}{2m_e}$ is the Bohr magneton and g is the Landé g-factor, which in a solid state environment depends on the charge carrier and a variety of factors including QD geometry, strain fields, and magnetic field orientation for the case of the heavy hole [83]. $\vec{S} = S\hbar\vec{\sigma}$ is the spin operator, with S as the spin projection of the charge carrier and $\vec{\sigma} = \sigma_x\hat{x} + \sigma_y\hat{y} + \sigma_z\hat{z}$ as the Pauli vector. The magnetic field oriented along the direction of growth axis (denoted the z axis) is denoted as the Faraday configuration, and does not affect the optical selection rules. This is due to the alignment of the magnetic field to the natural quantisation axis of the state in the z direction, where the cylindrical D_{2d} symmetry of the QD provides a preferential quantisation axis along the growth direction [84]. In the case of the positive exciton family $|\Downarrow\Uparrow\downarrow\rangle, |\Uparrow\Downarrow\uparrow\rangle$, the trion states and ground hole states shift in energy given by:

$$\begin{aligned} \Delta E_{\pm t} &= \pm g_e \mu_B |\vec{B}| \\ \Delta E_{\pm h} &= \pm g_h \mu_B |\vec{B}| \end{aligned} \tag{2.23}$$

Here, the positive trion g factor is determined by the single electron due to the anti-aligned spins of the two holes. Furthermore the signs of the g-factor are opposite for electrons and holes, and take different absolute values [85]. This results in the energies of the excited and ground state shifting in the opposite direction as pictured in Figure 2.7b. Aligning the magnetic field perpendicular to the growth axis gives the Voigt configuration, where the eigenstates of the system are no longer quantised along the z direction, but along the x axis (the QD is rotationally symmetric about the z axis, thus we can pick any direction in the x-y plane to be the x axis). An alternative description is that the Voigt magnetic field mixes the spin up and down states such that the new eigenstates are superpositions of the previous:

$$\begin{aligned} |\Uparrow\rangle_X &= |\Uparrow\rangle_Z + |\Downarrow\rangle_Z \\ |\Downarrow\rangle_X &= |\Uparrow\rangle_z - |\Downarrow\rangle_Z \end{aligned} \tag{2.24}$$

The optical selection rules for the new states can be determined by considering the decay channels for each trion state:

$$|\Uparrow\Downarrow\uparrow\rangle_X = |\Uparrow\Downarrow\uparrow\rangle_Z + |\Downarrow\Uparrow\downarrow\rangle_Z \rightarrow |L\rangle\,|\Uparrow\rangle_Z + |R\rangle\,|\Downarrow\rangle_Z \tag{2.25}$$

Writing the circular polarisation states in the linear basis:

$$\begin{aligned} |R\rangle &= |H\rangle + i\,|V\rangle \\ |L\rangle &= |H\rangle - i\,|V\rangle \end{aligned} \tag{2.26}$$

And regrouping terms results in the decay paths for the Voigt trion states:

$$|\Uparrow\Downarrow\uparrow\rangle_X \rightarrow |H\rangle\,|\Uparrow\rangle_X + i\,|V\rangle\,|\Downarrow\rangle_X \tag{2.27}$$
$$|\Downarrow\Uparrow\downarrow\rangle_X \rightarrow |H\rangle\,|\Downarrow\rangle_X + i\,|V\rangle\,|\Uparrow\rangle_X \tag{2.28}$$

Thus, applying a magnetic field in the Voigt configuration results in modified selection rules leading to horizontally polarised photons, as depicted in Figure 2.7c which illustrates the energy levels and allowed transitions for a charged QD with applied magnetic field. In contrast to the Faraday configuration (Fig. 2.7b), spin-flipping transitions (e.g. $|\Uparrow\Downarrow\uparrow\rangle_X \rightarrow i\,|V\rangle\,|\Downarrow\rangle_X$) are allowed in addition to the spin-preserving decay paths when measured in the x-projection basis with roughly equivalent branching ratios [86]. This behaviour of an excited state decaying into either ground states is exploited for the production of spin-photon entangled states. Furthermore, the Zeeman shift allow for selective resonant excitation of a single excited state, for example $|\Downarrow\rangle \rightleftarrows |\Uparrow\Downarrow\downarrow\rangle$ (blue transition in Figure 2.7d). By continuous pumping of this transition, the QD can be prepared in the unaddressed ground state $|\Uparrow\rangle$ from spontaneous emission into the state.

2.4 Entangled state production in quantum dots

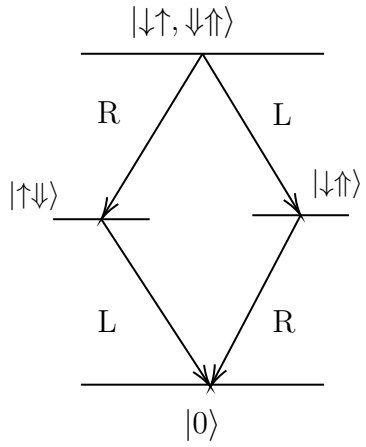
Photon-photon entanglement

A variety of states ranging from multiple-photon entangled states and combined spin-photon entangled states have been experimentally produced [82]. The first demonstration of the generation of entangled states in quantum dots was the production of a pair of photons in an entangled Bell state [87]. The biexciton decays radiatively to one of two bright exciton states, where it subsequently decays into the ground state [88]. The emitted photon from biexciton decay is described as a superposition of R and L polarisation states. The roughly equal branching ratios results in the decay of the biexciton to either exciton, producing a photon with the corresponding polarisation. Since the specific decay path remains undetermined until measurement, the resulting photon state must be expressed as a coherent superposition of both possible decay channels. Following this, the polarisation of the following photon emitted from excitonic decay is therefore correlated with the previously emitted photon, as illustrated in Figure 2.8a.

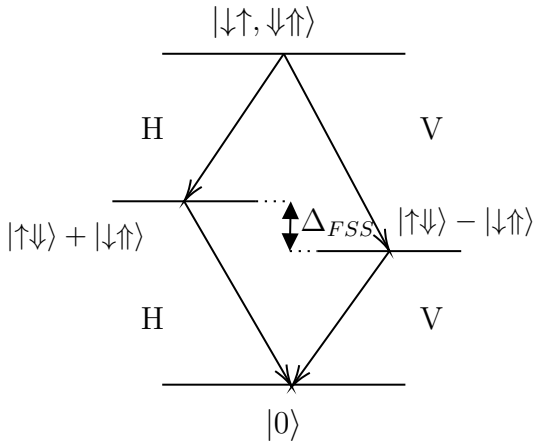
$$|\psi\rangle = |R\rangle_1\,|L\rangle_2 + |L\rangle_1\,|R\rangle_2 \tag{2.29}$$

Where the subscript denotes the individual photon emitted in the first and second cascaded decay process. Equivalently, this Bell state can be written in the horizontal/vertical basis (Equation 2.26):

$$|\psi\rangle = |H\rangle_1\,|H\rangle_2 + |V\rangle_1\,|V\rangle_2 \tag{2.30}$$



(a) The ideal biexciton decays to either of two separate exciton states, emitting an R or L circularly polarised photon. The subsequent decay of the exciton to the ground state emits another L or R polarised photon based on the decay path.



(b) Biexciton-exciton cascade in the presence of dot asymmetry, which mixes the exciton states and introduces an energy fine-structure splitting. This modifies the polarisation selection rules and shifts the energies of each transition.

Figure 2.8: **Allowed transitions in a QD.**

For spatially asymmetric dots such as those grown by the Stranski-Krastanov method, the reduced spatial asymmetry and the anisotropic charge carrier exchange interaction mixes the two excitons, modifying the optical selection rules and causing a split in energy between them defined as the fine-structure splitting [71]. The QD eigenstates are now linear combinations of the old exciton states $|X\rangle_{\text{new}} = |\uparrow\Downarrow\rangle \pm e^{i\theta} |\downarrow\Uparrow\rangle$, which result in the photons emitted through the cascaded decay process becoming linearly polarised.

The energy difference admits information leakage as two bits of information are encoded onto two separate degrees of freedom of the photons, leading to a less than maximally entangled state in a single measurement basis, often the polarisation basis [89]. Thus additional measures are often taken to reduce the energy splitting of the excitons, such as the application of magnetic [90] or optical fields [9]. Alternatively the growth of highly symmetric droplet etching epitaxial QDs such as those investigated here mitigates the fine-structure splitting leading to the production of high fidelity entangled states. The production of frequency indistinguishable entangled photon pairs with symmetric QDs was demonstrated in 2013 [91].

Spin-photon entanglement

Spin-photon entanglement has been demonstrated through the charged exciton decay channel. An external magnetic field in the Voigt configuration results in the energy states forming a double Λ system, where each excited state may decay to two ground states. The decay of one excited state into either ground state results in the polarisation of the emitted photon entangled with the spin state of the ground state hole. For example by considering the lowest three levels in Figure 2.7c, the decay of the $|\Uparrow\Downarrow\downarrow\rangle_X$ state results in the entangled state:

$$|\Uparrow\Downarrow\downarrow\rangle_X \rightarrow |H\rangle\,|\Downarrow\rangle_X + i\,|V\rangle\,|\Uparrow\rangle_X \tag{2.31}$$

A key challenge to producing spin-photon entangled states through this decay structure is the shift in transition energies through the Zeeman effect. As the excited and ground state manifolds energies shift with the magnetic field at separate rates and in different directions in energy, the horizontally polarised photon is red-shifted in comparison to the vertically polarised photon. This colour difference serves as an additional bit of information encoding the decay path of the excited state, and is detrimental to the entanglement quality between the spin-polarisation degrees of freedom of the quantum state. With the colour degree of freedom added to the entangled state, Eq. 2.31 becomes $|\psi\rangle = |H, \omega_{blue}\rangle\,|\Downarrow\rangle_X + i\,|V, \omega_{red}\rangle\,|\Uparrow\rangle_X$ and a detection of the photon in the R circular polarised state at time t_1 results in the time-dependent spin state:

$$|\psi(t)\rangle = \frac{1}{\sqrt{2}}\Big(e^{i\Delta\omega(t-t_1)}\,|\Downarrow\rangle - |\Uparrow\rangle\Big) \tag{2.32}$$

Where $\Delta\omega = \omega_{red} - \omega_{blue}$. The equivalent density matrix of this state is:

$$\begin{aligned}\rho(t) = \frac{1}{2}\Big[\,&|\Uparrow\rangle\langle\Uparrow| + |\Downarrow\rangle\langle\Downarrow| + \\ &+ ie^{i\Delta\omega(t-t_1)}\,|\Uparrow\rangle\langle\Downarrow| - ie^{-i\Delta\omega(t-t_1)}\,|\Downarrow\rangle\langle\Uparrow|\,\Big]\end{aligned} \tag{2.33}$$

The purity of Eq. 2.33 is written as $\mathrm{Tr}(\rho^2) = 1/2(e^{-i\Delta\omega(t-t_1)} + 1)$, which goes to zero for large energy differences resulting in a mixed state instead of a pure quantum state [86]. Techniques to "erase" the unwanted information have been demonstrated, where either the polarisation or colour degree of freedom is eliminated. In the case of erasing the colour information, De Greve et al. [86] frequency downconverts the emitted photons such that the energy difference between polarisations is indistinguishable from the overall linewidth of the frequency downconversion process. For eliminating the polarisation degree of freedom, Gao et al. [92] employs a circularly polarised resonant excitation scheme. As part of filtering out the excitation laser with a cross-polarisation setup, the scheme projects the emitted photons of each transition into a common polarisation, erasing the horizontal/vertical polarisation information.

2.5 Linear cluster state generation: the Lindner and Rudolph protocol

The generation of cluster states for quantum communication relies on the production of chains or lattices of entangled photons. The photon-spin coupling in a QD makes it a suitable candidate for deterministic on-demand generation of such states, through a series of repeated optical excitation and qubit rotations developed by Linder and Rudolph [13]. This protocol utilises the charged exciton energy level structure, where the only allowed transitions between pure z basis states are spin preserving and circularly polarised (Fig. 2.7a). For this section the hole and positive trion are used, however this protocol also applies for the electron and negative trion. Coherent control of the ground state is performed through the application of a magnetic field in the Voigt configuration. This results in a precession of the spin state in the Bloch sphere around the axis defined by the applied magnetic field. This is analogous to the Larmor precession of a classical magnetic moment about an external magnetic field. If the spin is initially prepared in the $|\Uparrow\rangle_Z$ state from the decay and heralded detection of a left circularly polarised photon (Fig. 2.7a), the spin will rotate in the plane perpendicular to the x axis. This is shown by writing the $|\Uparrow\rangle_Z$ state in the x-basis eigenstates $|\Uparrow\rangle_Z = |\Uparrow\rangle_X + |\Downarrow\rangle_X$. The time dependence of the state is given by the solution to the Schrödinger equation:

$$i\hbar\frac{d}{dt}|\psi(t)\rangle = H|\psi(t)\rangle \tag{2.34}$$

With the Hamiltonian given by Equation 2.22. In this case, the energy of each eigenstate determines the time dependence of the superposition state:

$$|\psi(t)\rangle = e^{i\Delta E_h t\hbar}|\Uparrow\rangle_X + e^{-i\Delta E_h t\hbar}|\Downarrow\rangle_X \tag{2.35}$$

Where $\pm\Delta E_h/2 = g\mu_B|B|$ are the energies of the $|\Uparrow,\Downarrow\rangle$ states respectively. Writing the X basis eigenstates in the Z basis results in:

$$|\psi(t)\rangle = i\sin\frac{\Delta E t}{\hbar}|\Uparrow\rangle_Z + \cos\frac{\Delta E t}{\hbar}|\Downarrow\rangle_Z \tag{2.36}$$

Thus the ground state spin precesses between the two Z states with characteristic period $T = \hbar/g_h\mu_B B_x$. With this mechanism, the protocol for cluster state generation is described as follows (Fig. 2.9):

1. Initialise the ground state qubit into a pure z basis state. This is achieved through exciting a hole in an initially statistical mixture of $|\Uparrow\rangle$ and $|\Downarrow\rangle$ states to the trion with linearly polarised light. The detection of a spontaneously emitted right circularly polarised photon heralds the qubit in the $|\Uparrow\rangle_Z$ state.

2. Perform a $\frac{\pi}{4}$ rotation of the qubit to the $|\Uparrow\rangle_Z + |\Downarrow\rangle_Z$ state using a magnetic field in Voigt configuration, aligned perpendicular to the growth direction. The spin qubit undergoes Larmor precession with a period of $T = \frac{h}{g_h \mu_b B}$, where h is the Planck constant, g_h is the g-factor of the ground state hole in the dot, and μ_b is the Bohr magneton.

3. A timed pulse of linearly polarised light just as the qubit precesses to $|\Uparrow\rangle_Z + |\Downarrow\rangle_Z$ places the state into $|\Uparrow\Downarrow\uparrow\rangle_Z + |\Downarrow\Uparrow\downarrow\rangle_Z$. Upon radiative decay, the total system is in the state $|R\rangle |\Uparrow\rangle_Z + |L\rangle |\Downarrow\rangle_Z$

4. Rotate the spin qubit by $\frac{\pi}{2}$ again. The state is now $|R\rangle_1 (|\Uparrow\rangle + |\Downarrow\rangle) + |L\rangle_1 (|\Uparrow\rangle - |\Downarrow\rangle)$. Another linearly polarised excitation and decay step puts the system in $\Big(|\Uparrow\rangle |R\rangle_2 + |\Downarrow\rangle |L\rangle_2 \Big) |R\rangle_1 + \Big(|\Uparrow\rangle |R\rangle_2 - |\Downarrow\rangle |L\rangle_2 \Big) |L\rangle_1$. Writing the polarisation of the first photon in the horizontal/vertical basis, the final system state can be re-written as [93]:

$$|\psi\rangle = -i |\Uparrow\rangle |V_1\rangle |R_2\rangle + |\Downarrow\rangle |H_1\rangle |L_2\rangle \tag{2.37}$$

This state is local unitary equivalent to the GHZ state, where the same error correcting codes can be used for either state [94]:

$$|GHZ\rangle = \frac{1}{\sqrt{2}}(|000\rangle + |111\rangle) \tag{2.38}$$

Repetition of steps 2-4 results in a 1 dimensional chain of entangled photons, only limited to the decoherence time of the ground state spin. As spin precession is driven by an external magnetic field, the field strength must be carefully balanced: the Zeeman splitting must remain within the transition linewidth to ensure frequency indistinguishability between polarisation states, while the precession rate must be fast enough to generate an adequate number of photons before decoherence. As an added factor, the finite radiative lifetime $1/\Gamma$ of the excited state means that after excitation, the excited state continues precessing for a indeterminate amount of time before decaying. This would introduce errors in the resultant entangled state as the precession rate and direction differ to the ground state due to the sign and magnitude of the g factor. As a result, the polarisation of the emitted photon is slightly rotated due to the spin precession of the trion. Mitigating this source of error requires the radiative lifetime to be significantly shorter than the precession period of the excited state, satisfying $1/\Gamma << h/g_e \mu_B B$ such that trion precession is suppressed prior to decay. This can be achieved by either increasing the precession period or decreasing the radiative lifetime. To reduce the radiative lifetime, the QD can be embedded within a micro-cavity structure tuned to the frequency of the emitted photons. This induces the Purcell effect which accelerates the decay of the photon proportional to the Q factor of the cavity

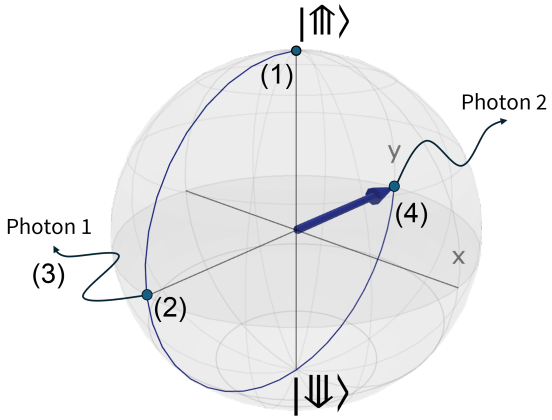


Figure 2.9: **Lindner and Rudolph protocol visualised on the Bloch sphere.** Timed excitation and decay steps as the spin precesses about the x axis produces chains of polarisation entangled photons. Each number corresponds with the associated step in the entanglement generation protocol.

Charge carrier	B field (mT)	Precession period (ns)	Decoherence time (ns) [38]	Entangled chain length	Ref.
Electron	40	3.25	1.5	3	[54]
Heavy hole	90	2.19	130	10	[59]
Dark exciton	12 (eff.[3])	3	145	5	[10]

Table 2.2: Literature cluster state production rates for various QD spin states.

[95, 96]. The short radiative lifetime also leads to a broadening of the emission frequency of the photons from the uncertainty principle, allowing for more room for error in frequency indistinguishability when increasing the magnetic field. On the opposite side, spin decoherence through environmental nuclear spin interactions limits the generation of large numbers of entangled photon states. Spin coherence is progressively lost throughout execution of the protocol, incentivising a faster precession time such that each photon is generated at a faster rate. Mitigating the effect of decoherence would involve increasing the strength of the magnetic field to produce a higher rate of photon production. This would also have the advantage of generating a larger cluster state, which is desirable for further quantum information applications.

The decoherence time for various electronic spin states is summarised in Table 2.2. Experimental generation of cluster states has been demonstrated for each choice of spin

[3] Assuming a DE g-factor of 1.85 [97]

state, though the length of each chain varies according to the decoherence time for each spin. The first experimental demonstration by Schwartz et al. used the precession of a dark exciton, which featured a slightly different energy level structure than the charged exciton and incorporated an intermediate state to initialise the dark exciton [10]. This lead to a significant timing jitter from the non-radiative phonon-assisted decay of the intermediate state, disrupting the indistinguishability of the emitted photons. Coste et al. [93] utilised the electron-negative trion energy structure in a direct implementation of the Lindner and Rudolph protocol, though the low decoherence time limited the number of photons produced. Finally Cogan et al. [98] in the same year demonstrated the production of a longer entangled linear cluster state using the heavy hole owing to a decoherence time two orders of magnitude higher than the electron.

Enhancing cluster state generation

Improving on the established Lindner and Rudolph protocol requires an increase in the number of photons in the cluster state without compromising the indistinguishability of each photon. Higher magnetic fields offer the potential to improve the photon generation rate. However, this approach must account for the finite decay time of the excited state and the impact of Zeeman splitting, which can compromise the indistinguishability between polarization states. The finite decay time may be partially mitigated through Purcell enhancement by embedding the QD in a micro-cavity. However, frequency indistinguishability remains a challenge particularly at higher fields where the energy differences exceed the transition linewidth. This work aims to address this point, seeking to enable faster spin precession while maintaining energy separation below the transition linewidth. This is accomplished through introducing a red-detuned laser that addresses both transitions, inducing the AC Stark effect on the excited and ground states. The Stark effect increases the transition frequency at a rate proportional to the detuning between the laser and transition frequencies, effectively negating the energy splitting due to the Zeeman effect. This would allow for an increased magnetic field strength and thus higher cluster state generation rates. The implementation of an AC Stark shift has been demonstrated on the exciton-biexciton manifold for the elimination of the fine-structure splitting of the bright exciton in self-assembled QDs [9]. This resulted in the restoration of degeneracy for both decay channels. enabling the generation of high quality two-photon entangled states. Furthermore, the Stark effect has been shown to shift the transitions in the charged exciton manifold, enabling coherent control of the energy states in a QD [99]. This thesis thus proposes a natural extension of the aforementioned works in applying the Stark effect to a trion manifold in the presence of an external magnetic field for the enhanced generation of spin-photon entangled states.

Chapter 3

The combined Zeeman-AC Stark effect on the trion-hole manifold

This chapter develops the dressed-state physics of atomic and molecular optics and applies it to the trion manifold of the QD, along with the spin-state physics underpinning the Lindner and Rudolph protocol for the generation of entangled cluster states. The central tension between decreasing the spin precession period and maintaining frequency indistinguishability is discussed. The AC Stark effect, the far detuned case of dressed state physics, is shown to relieve this tension. A four level system is introduced to model the charged positive exciton-hole manifold, with two ground states corresponding to the hole spin and two excited states for the trion. The AC Stark shift for a simplified two-level system is then applied to the four level system of the quantum dot along with an external magnetic field. Finally the simulated combined effects of the AC Stark laser and applied magnetic field is presented, demonstrating a viable approach to reconciling the trade-off between faster spin precession and preserving frequency indistinguishability within the emission linewidth.

3.1 Light-matter interactions and the optical Stark effect

The interaction of confined charge carriers in quantum dots with light is well described in the physics of atom-light interactions, a cornerstone in the field of atomic and molecular optics. This section begins with a description of an idealised two level matter system interacting with a monochromatic laser field, where the two level system may represent either the empty QD and neutral exciton, or the confined hole (electron) and positive (negative) trion. The excited state $|e\rangle$ and ground state $|g\rangle$ are separated by

energy $\hbar\omega_0$, and are governed by the Hamiltonian:

$$H_0 = -\frac{\hbar\omega_0}{2}\left|g\right\rangle\left\langle g\right| + \frac{\hbar\omega_0}{2}\left|e\right\rangle\left\langle e\right| \tag{3.1}$$

The interaction Hamiltonian in the electric dipole approximation is [100]:

$$H_{\text{int}} = -\vec{\mathbf{d}}\cdot\vec{E}(t) \tag{3.2}$$

Where $\vec{\mathbf{d}}$ is the dipole moment $\vec{\mathbf{d}} = q\hat{\mathbf{r}}$ and $\vec{E}$ is the electric field.
The simplest description of the effects of the light field on a quantised two-level system is by describing the field as a classical electric field oscillating with frequency ω_L. In this semi-classical approach, the electric field is treated as a potential acting on the system and is generally valid for large field strengths but breaks down when approaching small photon numbers. Choosing the electric field polarisation in the z direction, the field at the origin is written as $\vec{E}(t) = |E|\cos(\omega_L t)\hat{z}$ for some amplitude $|E|$. This can be decomposed into positive and negative frequency components:

$$\vec{E}(t) = \frac{|E|}{2}\left(e^{-i\omega_L t} + e^{i\omega_L t}\right)\hat{z} \tag{3.3}$$

The dipole moment operator acting on the Hilbert space spanned by the two level system is evaluated by inserting a complete set of states $\vec{\mathbf{d}} = \sum_{i,j} e\left|i\right\rangle\left\langle i\right|\hat{\mathbf{r}}\left|j\right\rangle\left\langle j\right|$. Since the position operator $\hat{\mathbf{r}}$ has odd spatial parity, $\left\langle e\right|\vec{\mathbf{d}}\left|e\right\rangle = \left\langle g\right|\vec{\mathbf{d}}\left|g\right\rangle = 0$ and the operator simplifies to

$$\vec{\mathbf{d}} = \vec{d}_{eg}\left|e\right\rangle\left\langle g\right| + \vec{d}^{*}_{eg}\left|g\right\rangle\left\langle e\right| \tag{3.4}$$

This indicates that the transition dipole moment operator couples the excited and grounds states. Assuming the dipole axis is parallel to the field polarisation[1], the dot product between the transition dipole moment and electric field picks off the z component of the dipole moment. The interaction Hamiltonian (Eq. 3.2) can be written as:

$$H_{\text{int}} = \frac{|E|}{2}\left(d_{eg}e^{-i\omega_L t}\left|e\right\rangle\left\langle g\right| + d_{eg}e^{i\omega_L t}\left|e\right\rangle\left\langle g\right| + d^{*}_{eg}e^{-i\omega_l t}\left|g\right\rangle\left\langle e\right| + d^{*}_{eg}e^{i\omega_L t}\left|g\right\rangle\left\langle e\right|\right) \tag{3.5}$$

$$= \frac{\hbar\Omega}{2}\left(\left(e^{-i\omega_L t} + e^{i\omega_L t}\right)\left|e\right\rangle\left\langle g\right| + \left(e^{i\omega_L t} + e^{-i\omega_L t}\right)\left|g\right\rangle\left\langle e\right|\right) \tag{3.6}$$

Where d_{eg} refers to the z component of the dipole moment, and introducing the Rabi frequency as $\Omega = \frac{|E|d_{eg}}{\hbar}$, assuming it to be purely real ($\Omega = \Omega^*$). To simplify this into a form that has a straightforward solution, this Hamiltonian is first transformed into the

[1]This assumption generally holds for any field polarisation as one can choose a linear combination of excited states that are parallel to the field. This applies for both neutral and charged exciton transitions.

interaction picture[2] with the unitary operator $U = e^{iH_0 t/\hbar}$. For brevity, the result of this transformation are stated here with details of the calculation found in Appendix A.

$$H_{\text{int}} \to \tilde{H}_{\text{int}} = -\frac{\hbar\Omega}{2}\Big(\left(e^{-i(\omega_0+\omega_L)t} + e^{i(\omega_0-\omega_L)t}\right)|e\rangle\langle g| + \left(e^{i(\omega_0-\omega_L)t} + e^{i(\omega_0+\omega_L)t}\right)|g\rangle\langle e|\Big) \tag{3.7}$$

Here, the rotating wave approximation is made where the fast oscillating terms $\omega_0+\omega_L$ are discarded. This approximation applies when the laser frequency is close to the transition frequency such that the detuning $\Delta = \omega_0 - \omega_L$ is much smaller than the fast oscillating terms. Transforming back to the Schrödinger picture, the Hamiltonian of the overall system is:

$$H_{\text{total}} = H_0 + H_{\text{int}} = -\frac{\hbar\omega_0}{2}|g\rangle\langle g| + \frac{\hbar\omega_0}{2}|e\rangle\langle g| - \frac{\hbar\Omega}{2}\Big(e^{i\omega_L t}|e\rangle\langle g| + e^{i\omega_L t}|g\rangle\langle e|\Big) \tag{3.8}$$

Finally the time-dependence is removed by making another unitary transformation $U = e^{-i\omega_L t/2(|g\rangle\langle g| - |e\rangle\langle e|)}$, which maintains the dynamics of the system but simplifies the problem. This corresponds with a transformation to a rotating reference frame about the z axis with frequency ω_L. This results in the Hamiltonian:

$$H = -\frac{\hbar\Delta}{2}|g\rangle\langle g| + \frac{\hbar\Delta}{2}|e\rangle\langle e| - \frac{\hbar\Omega}{2}(|e\rangle\langle g| + |g\rangle\langle e|) \tag{3.9}$$

$$= \begin{pmatrix} -\hbar\Delta/2 & -\hbar\Omega/2 \\ -\hbar\Omega/2 & \hbar\Delta/2 \end{pmatrix} \tag{3.10}$$

This Hamiltonian is easily diagonalisable with eigen-energies:

$$E_\pm = \pm\frac{\hbar}{2}\sqrt{\Omega^2 + \Delta^2} \tag{3.11}$$

Before writing the corresponding eigenstates, it is useful to define a "mixing" angle [101]:

$$\tan\theta = \frac{\Omega}{\Delta} \tag{3.12}$$

The corresponding eigenstates written in the $|g\rangle, |e\rangle$ basis are:

$$\begin{aligned} |+\rangle &= \cos(\theta/2)|e\rangle + \sin(\theta/2)|g\rangle \\ |-\rangle &= \sin(\theta/2)|e\rangle - \cos(\theta/2)|g\rangle \end{aligned} \tag{3.13}$$

These eigenstates are known as "dressed states", where the incident light field mixes the ground and excited matter states. The energies of the dressed states in the rotating frame are shown in Figure 3.1. On resonance the uncoupled states depicted as dotted lines are degenerate, however the applied field alters the energies into an avoided crossing.

[2] Equivalently, the co-rotating frame of the two-level system.

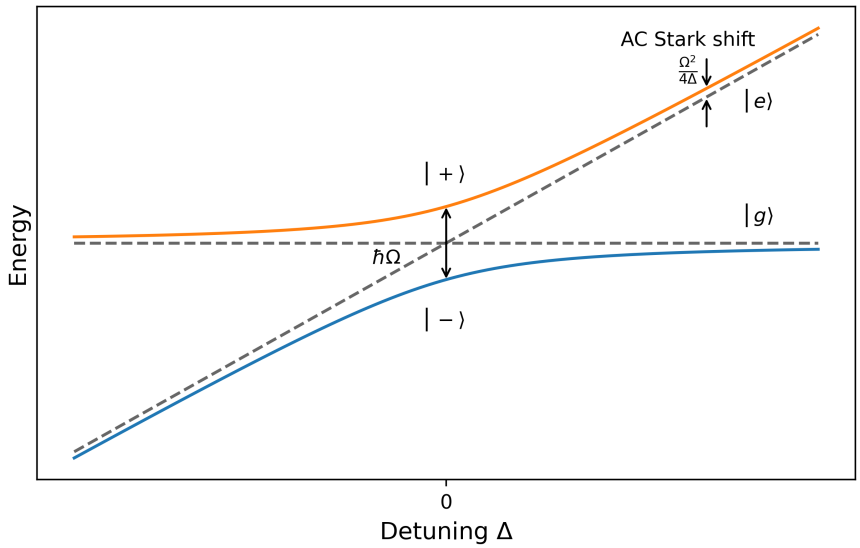


Figure 3.1: **Dressed state energies in the rotating frame.** On resonance ($\Delta = 0$), the dressed states are separated by the Rabi frequency Ω and are equal superpositions of the initial ground and excited states. Off resonance, the eigenstates have similar energies to the initial states with a shift of $\frac{\Omega^2}{4\Delta}$.

Resonant case

In the resonant case ($\Delta = 0$), the mixing angle is $\theta = \pi/2$ which results in a pair of symmetric and anti-symmetric superpositions of the excited and ground states $|\pm\rangle = (|e\rangle \pm |g\rangle)/\sqrt{2}$. These states are split in energy by the Rabi frequency Ω. The system initially in the $|g\rangle$ state evolves over time as

$$|\psi(t)\rangle = e^{-i\Omega t/2}|+\rangle - e^{i\Omega t/2}|-\rangle \tag{3.14}$$

Projecting the dressed states onto the $|e, g\rangle$ basis results in an oscillation between the excited and ground states with frequency $\Omega/2$[3]:

$$|\psi(t)\rangle = -i\sin(\Omega t/2)|e\rangle + \cos(\Omega t/2)|g\rangle \tag{3.15}$$

This is the phenomenon known as Rabi oscillation, where the applied laser drives the matter state between the excited and ground states. This allows for the preparation of any superposition of the excited and ground states. An applied pulse with length tuned to $\Omega t = \pi/2$ (a "$\pi/2$ pulse") results in the following evolutions for initial states $|e\rangle, |g\rangle$:

$$|e\rangle \to i|e\rangle + |g\rangle, \ |g\rangle \to -i|e\rangle + |g\rangle \tag{3.16}$$

A π-pulse instead exchanges the two states:

$$|e\rangle \to i|g\rangle, \ |g\rangle \to -i|e\rangle \tag{3.17}$$

In this way any superposition state may be prepared by tuning the pulse length of the resonant laser.

Far off-resonance case

In the limit that the detuning is very large ($|\Delta| \gg \Omega$), $\tan\theta \to +\infty$ and $\theta \to 0$ for positive (red) detuning, and $\theta \to \pi$ for negative (blue). The dressed states approach the unperturbed $|e\rangle, |g\rangle$ states with a small mixing with the opposing $|g\rangle, |e\rangle$ state. The eigenstates to first order in Ω/Δ in the unperturbed basis are:

$$\begin{aligned} |-\rangle &= |g\rangle - \frac{\Omega}{2\Delta}|e\rangle \\ |+\rangle &= \frac{\Omega}{2\Delta}|g\rangle + |e\rangle \end{aligned} \tag{3.18}$$

Thus for large detunings the eigenstates $|\pm\rangle$ are similar to the unperturbed states $|g, e\rangle$ with a small component from the other state.

[3]Conventions vary in literature when defining the Rabi frequency Ω, where the factor of 1/2 is sometimes absorbed into the definition in Equation 3.6.

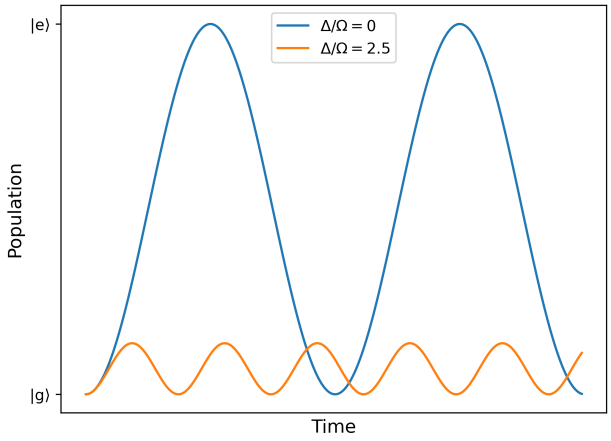


Figure 3.2: **Rabi oscillations as a function of detuning.** Two detuning parameters are illustrated with $|g\rangle$ as the initial state. Dressing the system with a resonant laser results in oscillations between the excited and ground states at frequency $\Omega/2$. Off resonant pumping results in oscillations at a higher frequency $\sqrt{\Delta^2+\Omega^2}/2$.

The time dependence of the states in both cases is depicted in Figure 3.2. In the resonant case, the initial ground state exhibits a periodic population inversion between the excited and ground at a frequency equal to the Rabi frequency Ω. For the off-resonant case, oscillations occur at the generalised Rabi frequency:

$$\Omega_R = \frac{1}{2}\sqrt{\Delta^2+\Omega^2} \tag{3.19}$$

The initial ground state fails to fully reach the excited state, indicating that it remains predominantly in the ground state throughout the time evolution. The energies of the eigenstates approach the initial states as a function of Δ with a small correction, derived by expanding the eigen-energies $E_\pm = \pm\frac{\hbar\Delta}{2}\sqrt{1+\frac{\Omega^2}{\Delta^2}}$ in powers of Ω/Δ:

$$E_\pm = \pm\frac{\hbar}{2}\left(\Delta + \frac{\Omega^2}{2\Delta} + O\left(\frac{\Omega^4}{\Delta^3}\right)\right) \tag{3.20}$$

The first order correction term $\Delta E = \frac{\Omega^2}{4\Delta}$ to the energies is defined as the "AC Stark shift". This results in the energy splitting of the two-level system shifting by $\Omega^2/2\Delta$ in the large detuning limit. Such an effect has been experimentally demonstrated on the trion-electron state manifold in QDs, shifting the transition frequency by up to 20 GHz in either direction with a red or blue detuned laser [99]. As the AC Stark shift is inversely proportional to the detuning, a lower detuning value has a greater

effect on the energy states. This property may be exploited for the suppression of the Zeeman splitting in the cluster state generation process, where the lower energy transition experiences a lower laser frequency detuning leading to a greater Stark shift.

One extenuating factor may arise from the non-zero excited state component in the ground-like dressed state $|-\rangle$, as the excited state component couples to the external vacuum fields and undergoes spontaneous emission. This results in the emission of photons at a rate proportional to the excited state population. A constant photon emission background may be significant in the context of the Lindner and Rudolph protocol as unwanted photon emission may pollute the generated entangled state. With the excited state population scaling with $|\Omega/2\Delta|^2$ (Eq. 3.18) and AC Stark shift scaling with $\Omega^2/4\Delta$ (Eq. 3.20), the energy shift increases faster than the excited state population. This would suggest an ideal range where the Stark shift is large enough to negate the Zeeman effect but low enough to have a insignificant excited state population.

3.2 Mathematical description of the trion manifold

The QD system with applied magnetic and oscillating electric fields has been explored in Flagg & Solomon (2015) for the charged exciton manifold [102]. The authors investigate the effect of a circularly polarised AC Stark field on the optical selection rules in the presence of a magnetic field, where the polarisation was chosen such that only one transition was addressed. Here, we extend the analysis to a linear polarised beam where both transitions are addressed. The Hamiltonian is written as:

$$H = H_0 - \underbrace{\vec{\mu}\cdot\vec{B}}_{H_B} - \underbrace{\vec{d}\cdot\vec{E}}_{H_E} \tag{3.21}$$

The unperturbed Hamiltonian H_0 is a four level system comprising of two degenerate excited states and two degenerate ground states. These states correspond to the two z-component spin states of the trion and ground state hole, with the ground states defining the logical qubit states $|1\rangle, |0\rangle$. With the transition frequency ω_0 separating the excited states $|t\pm\rangle$ from the ground states $|h\pm\rangle$ and choosing the reference energy to be halfway between excited and ground states, the unperturbed Hamiltonian is:

$$H_0 = -\frac{\hbar\omega_0}{2}\Big(|h+\rangle\langle h+| + |h-\rangle\langle h-|\Big) + \frac{\hbar\omega_0}{2}\Big(|t+\rangle\langle t+| + |t-\rangle\langle t-|\Big) \tag{3.22}$$

An external magnetic field in the Voigt configuration couples the two ground states and two excited states. Following the formalism introduced in Section 2.3.3, the effect is extended to four states with the Hamiltonian:

$$H_B = \mu_B B_x\Big(-|g_{h,x}|\big[\,|h+\rangle\langle h-| + |h-\rangle\langle h+|\,\big] + |g_e|\big[\,|t+\rangle\langle t-| + |t-\rangle\langle t+|\,\big]\Big) \tag{3.23}$$

The signs for $g_{h,x}$ and g_e is explicitly placed as the g factors differ by a sign. In the Z-basis, the state initially prepared in $|h+\rangle$ would precess about the x axis at the Larmor frequency $\omega_B = g_h \mu_B B_x/\hbar$. As the g factors of the electron and hole differ, so would the direction and magnitude of the precession frequency of the spins. A mono-frequency laser incident on the QD is modelled as a oscillating electric field with frequency ω_L as introduced in Section 3.1. In the electric dipole approximation, only transitions between states with angular momentum difference $\Delta m_j = \pm 1$ are allowed to ensure conservation of angular momentum. Here, the spin up excited and ground states $|t+\rangle, |h+\rangle$ are coupled by left circularly polarised light, and separately with the spin down states $|t-\rangle, |h-\rangle$ for right circular polarisation. In the appropriate rotating reference frame, the combined unperturbed Hamiltonian and electric field perturbation is written as:

$$\begin{aligned} H_0 + H_E = &- \frac{\hbar\Delta}{2}\Big(|h+\rangle\langle h+| + |h-\rangle\langle h-| \Big) + \frac{\hbar\Delta}{2}\Big(|t+\rangle\langle t+| + |t-\rangle\langle t-| \Big) \\ &- \frac{\hbar\Omega_+}{2}\Big(|h+\rangle\langle t+| + |t+\rangle\langle h+| \Big) - \frac{\hbar\Omega_-}{2}\Big(|h-\rangle\langle t-| + |t-\rangle\langle h-| \Big) \end{aligned} \tag{3.24}$$

Here $\Delta = \omega_0 - \omega_L$ is the the detuning between the resonant transition frequency of the QD and the applied laser, and $\Omega_\pm$ is the Rabi frequency for the left and right circularly polarised components of the electric field. A linearly polarised field would thus have equal Rabi frequency magnitudes. In the unperturbed state basis $|\psi_i\rangle = |h+\rangle, |h-\rangle, |t+\rangle, |t-\rangle$, the total Hamiltonian can be represented as a matrix with elements $A_{ij} = |\psi_i\rangle\langle\psi_j|$:

$$H = \hbar \begin{pmatrix} -\Delta/2 & -\mu_B B_x g_{h,x}/\hbar & -\Omega_+/2 & 0 \\ -\mu_B B_x g_{h,x}/\hbar & -\Delta/2 & 0 & -\Omega_-/2 \\ -\Omega_+/2 & 0 & \Delta/2 & \mu_B B_x g_e/\hbar \\ 0 & -\Omega_-/2 & \mu_B B_x g_e/\hbar & \Delta/2 \end{pmatrix} \tag{3.25}$$

3.3 Simulated emission spectrum

The influence of the magnetic field and subsequently the AC Stark laser on the eigenenergies of the Hamiltonian is first shown schematically in Figure 3.3. The initially degenerate transitions are split by the magnetic field, red-shifting one transition while blue-shifting the other. In the application of a laser with lower frequency, the red-shifted transition has a lower detuning between laser and transition when compared to the blue-shifted one. This results in the red transition experiencing a greater AC Stark shift, allowing the energies to catch up as the laser intensity Ω is increased. If the linewidth of each transition surpasses their energy separation, the transitions

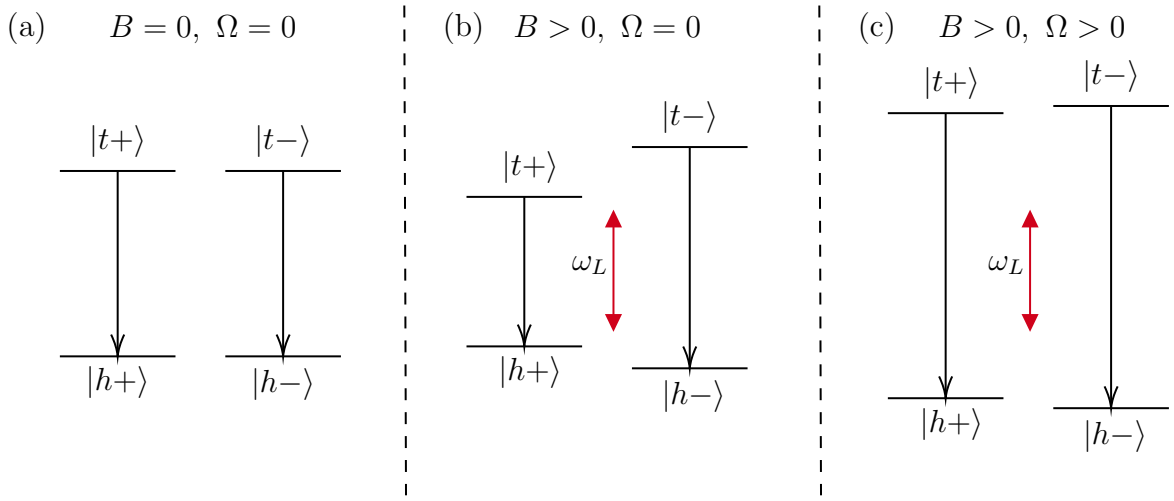


Figure 3.3: **QD energy level structure at various field strengths**. Energy states are given in the R/L basis with (a) no magnetic field and no applied Stark field, (b) applied magnetic field, (c) simultaneous magnetic and laser fields. The laser frequency (ω_L) is detuned relative to the transition frequencies of the QD. The labelled states are not strictly accurate due to the magnetic field induced state mixing, however are placed as a useful reference for tracking eigen-energies.

can be considered effectively degenerate within the linewidth. Additionally, a limited frequency resolution of the detector may further enhance the apparent frequency indistinguishability when measuring this effect.

To investigate the simultaneous application of the magnetic and AC Stark fields, numerical simulations of the spontaneous emission process was performed, allowing for the extraction of the resulting emission spectrum. Throughout this work, the Python package QuTiP was utilised to simulate various quantum processes including the dynamics of closed and open quantum systems [103]. This approach incorporates the transition lifetimes when simulating the emission process, which translates to an estimate of the linewidth of each emission. By accounting for the natural broadening of emission lines in the simulation, the relationship between emission line separation and transition linewidth can be analysed.

Computing the emission spectrum

The spontaneous emission process may be solved analytically through the Wigner-Weisskopf formalism where a two-level system is coupled to a continuum of frequency modes [104], however extending the theory to a four level system with various perturbing fields becomes significantly more complex. Instead an alternative approach is adopted that is suitable for numerical integration, involving analysing the first order

coherence function of the emitted EM field.

To establish the methodology, the process of evaluating the emission spectrum is briefly outlined for a two level system before extending it to the four level system of interest. A full derivation of the process is available in Chapter 10 of *Quantum Optics*, Scully & Zubairy (1997) [100]. The emission spectrum is obtained via the Fourier transform of the first order correlation function of the emitted field in the steady state:

$$S(\mathbf{r},\omega) = \frac{1}{\pi}\,\mathrm{Re}\int_0^\infty d\tau \langle E^{(-)}(\mathbf{r},t)E^{(+)}(\mathbf{r},t+\tau)\rangle e^{i\omega\tau} \tag{3.26}$$

The correlation function is a measure of the coherence of the emitted field. In the case of light produced from the decay of an excited state of a two-level system, the function is related to the two-time expectation value of the raising and lowering operators $\sigma_\pm$ of the matter state:

$$\langle E^{(-)}(\mathbf{r},t)E^{(+)}(\mathbf{r},t+\tau)\rangle = I_0\langle\sigma_-(t)\sigma_+(t+\tau)\rangle \tag{3.27}$$

Where I_0 is a constant incorporating various properties of the field:

$$I_0 = \left(\frac{\omega^2 d_{eg}}{4\pi\epsilon_0 c^2 \mathbf{r}}\right)^2 \tag{3.28}$$

The lowering operator for a two level system is defined as $\sigma_- = |g\rangle\langle e|$, which transforms the excited state to the ground state. The raising operator σ_+ is its Hermitian adjoint $\sigma_-^\dagger = \sigma_+ = |e\rangle\langle g|$. Through the quantum regression theorem [105], the two-time expectation value is expressed as:

$$\langle\sigma_-(t)\sigma_+(t+\tau)\rangle = \rho_{eg}(t+\tau)\langle\sigma_+(t)\rangle \tag{3.29}$$

$$\langle\sigma_+(t)\rangle = \mathrm{Tr}[\sigma_+(0)\rho(t)] \tag{3.30}$$

Where ρ is the reduced density matrix of the two-level system after taking the trace over the continuum of field modes, and ρ_{eg} is the coefficient of the matrix element of the density matrix $\rho_{eg}|e\rangle\langle g|$. The time evolution of the density matrix is governed by the Linblad master equation, which serves as the open quantum system analog to the Schrödinger equation.

$$\dot{\rho} = -\frac{i}{\hbar}[H,\rho] + \sum_i \Gamma_i\Big(L_i\rho L_i^\dagger - \frac{1}{2}\{L_i^\dagger L_i,\rho\}\Big) \tag{3.31}$$

Where H is the Hamiltonian, $\{a,b\}$ is the anti-commutator $(ab+ba)$, L_i are jump operators that describe the dissipative dynamics from the system-environment coupling, and Γ_i are the corresponding dissipation rates. In the two level system, this corresponds to the lowering operator σ_- and decay rate Γ. Solving for the density matrix ultimately yields the emission spectrum of the system.

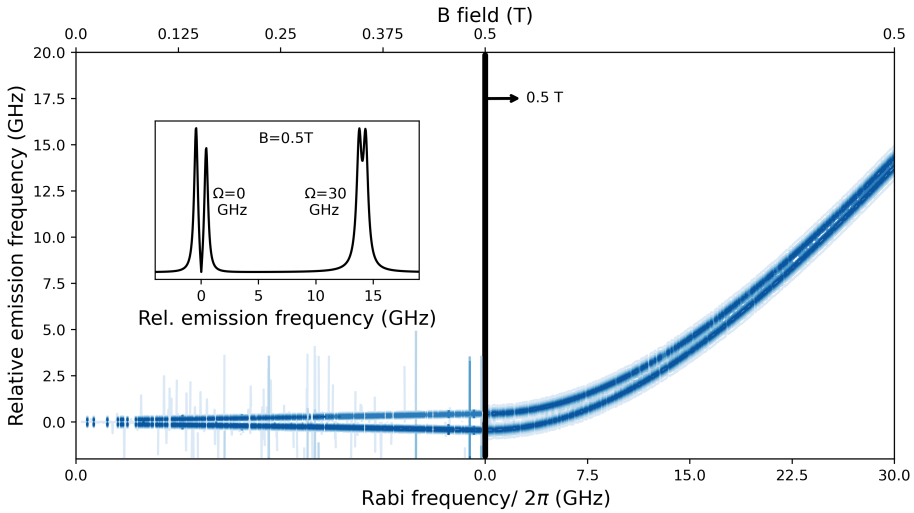


Figure 3.4: **Simulated emission frequencies.** First as a function of magnetic field, followed by Rabi frequency which is proportional to laser intensity. In this simulation the detuning is set to $\Delta/2\pi = 25$ GHz. Artefacts in the magnetic field section are likely due to instabilities in the simulation. Inset: Emission spectra at two Rabi frequencies. Increasing laser intensity simultaneously shifts both transition frequencies and reduces the energy difference between transitions.

Simulated spectra

For the case of the four-level system, the lowering operator is defined as $\sigma_- = |h+\rangle\langle t+| + |h-\rangle\langle t-|$. This allows for the transformation of any superposition of excited trion states to its corresponding ground state. While the emission spectrum can be derived exactly for a two-level system with some effort, the extension to a four level system requires solving 16 coupled differential equations. Instead, numerical methods for solving the density matrix in the presence of applied magnetic and laser fields are employed. In the simulations, equal decay rates between polarisations are assumed. While fine-structure splitting, QD anisotropies, and birefringence effects in the growth material may all affect the transition lifetime, such considerations is beyond the scope of the current work. Radiative lifetimes vary between individual samples in the literature, ranging from 380 [106] to 800 ps [107]. For this work, a lifetime of 400 ps was chosen, corresponding to a recombination rate of 2.5 GHz.

Figure 3.4 depicts the simulated emission frequencies relative to the unperturbed trion transition frequency as a function of the magnetic field, followed by the application of the AC Stark field with increasing Rabi frequency. The initially degenerate transitions are split by the applied magnetic field by approximately 2 GHz at a field strength of 0.5 T, scaling linearly with increasing magnetic field strength. Increasing

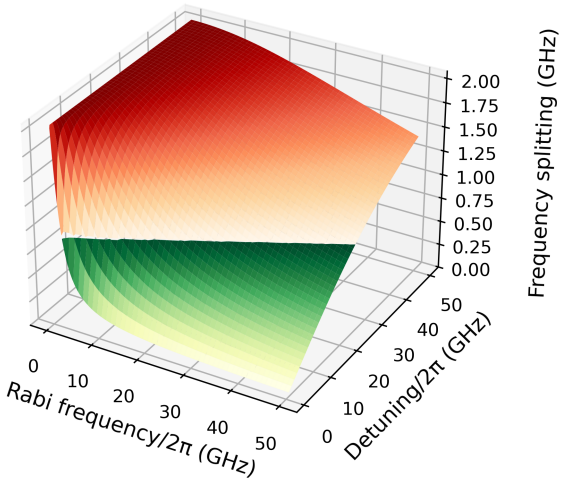


Figure 3.5: **Transition frequency separation as a function of detuning and Rabi frequency.** Colours correspond to energy splittings above (orange) and below (green) $1/e$ times the linewidth of each transition.

laser intensity at a detuning of $\Delta/2\pi = 25$ GHz causes both transitions to increase in frequency scaling with the square of Rabi frequency, while the difference in transition frequencies decrease as expected. The inset plot illustrates the difference in emission spectra at two Rabi frequencies. At 30 GHz, the peaks of each transition are significantly closer than at 0 GHz, confirming the effect of the AC Stark shift to reduce the splitting between transitions.

Figure 3.5 shows the transition frequency splitting as both Rabi frequency and detuning are varied, with an applied magnetic field strength of 0.5 T. At 0 Rabi frequency, corresponding to disabling the AC Stark laser, the frequency splitting is maximised. Increasing Rabi frequency reduces the the frequency splitting as the energy levels converge, which correspond to an increasing AC Stark effect. Increasing the detuning on the other hand reduces the AC Stark effect, which is reflected in a greater energy difference. The green region indicates where the transition frequency splitting falls below $1/e$ of the linewidth for each transition. This threshold was chosen as an estimate for the point at which the two transitions become indistinguishable to a detector with finite resolution.

3.4 Spin precession frequency

While it was shown above that the emission frequency splitting can be reduced with the AC Stark effect, a question still remains about whether the Stark field affects the spin precession frequency. To investigate this, the time dependency of the state evolving under the Hamiltonian (Eq. 3.25) is analysed. For completeness, the evaluation of the precession of the ground state hole with an effective spin of $\frac{1}{2}$ is described before extending the analysis to the four level system. Two initially degenerate states $|h\pm\rangle$ are perturbed by a magnetic field in the x direction. Setting the reference energy to the energy of the unperturbed states, the Hamiltonian is given by:

$$\begin{aligned} H &= \mu_B B_x g_{h,x} \sigma_x \\ &= \begin{pmatrix} 0 & \mu_B B_x g_{h,x} \\ \mu_B B_x g_{h,x} & 0 \end{pmatrix} \end{aligned} \tag{3.32}$$

Where σ_x is the Pauli x matrix. The time dependence of a state initially prepared in the z eigenstate $|\psi(0)\rangle = |h+\rangle$ is given by Equation 2.36. The oscillation between states can be extracted from the projection onto the z axis of the Bloch sphere. This corresponds to taking the expectation value of the Pauli Z matrix $\langle\sigma_z\rangle = \langle\psi(t)|\,\sigma_z\,|\psi(t)\rangle$:

$$\langle\psi(t)|\,\sigma_z\,|\psi(t)\rangle = \cos\left(2\mu_B B_x g_{h,x} t/\hbar\right) \tag{3.33}$$

The Larmor frequency can thus be extracted as $\omega = 2\mu_B B_x g_{h,x}/\hbar$. This is extended to the four level system by defining the qubit as the two hole states $|h\pm\rangle$, and neglecting the population of the trion states which is assumed to be small compared to the hole state population. The initial state remains as $|\psi(0)\rangle = |h+\rangle$, but now lives on the Hilbert space spanned by the eigenstates of Equation 3.22. The operator in the role of the Pauli Z matrix written in the basis of the aforementioned eigenstates is $\sigma_Z^{'} = |h+\rangle\langle h+| - |h-\rangle\langle h-|$, with no components proportional to the trion states $|t\pm\rangle\langle t\pm|$. With the Hamiltonian defined in Equation 3.25, the time evolution of this state is solved analytically with the aid of the computer algebra system Mathematica. Four frequency components are identified in the time dependent z projection expectation value:

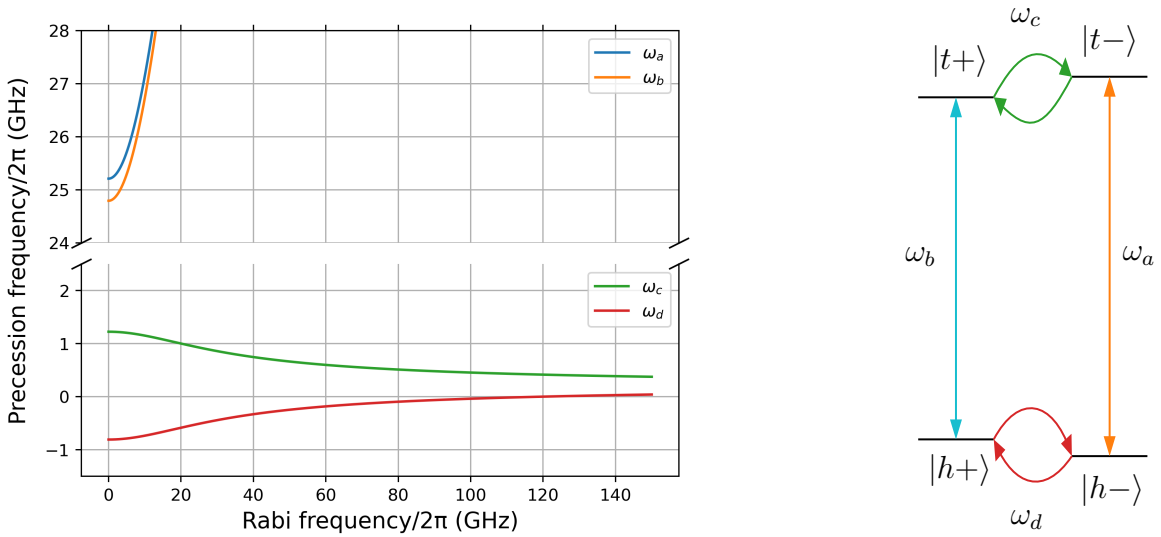
$$\begin{aligned} \omega_a = (g_e - g_h)\frac{\mu_B B_x}{\hbar} \\ + \frac{1}{2}\sqrt{(\Delta-\omega_z)^2+\Omega^2} + \sqrt{(\Delta+\omega_z)^2+\Omega^2} \end{aligned} \tag{3.34a}$$

$$\begin{aligned} \omega_b = -(g_e - g_h)\frac{\mu_B B_x}{\hbar} \\ + \frac{1}{2}\sqrt{(\Delta-\omega_z)^2+\Omega^2} + \sqrt{(\Delta+\omega_z)^2+\Omega^2} \end{aligned} \tag{3.34b}$$

$$\omega_c = (g_e - g_h)\frac{\mu_B B_x}{\hbar} - \frac{1}{2}\sqrt{(\Delta-\omega_z)^2+\Omega^2} + \sqrt{(\Delta+\omega_z)^2+\Omega^2} \tag{3.34c}$$

$$\omega_d = (g_e - g_h)\frac{\mu_B B_x}{\hbar} + \frac{1}{2}\sqrt{(\Delta-\omega_z)^2+\Omega^2} - \sqrt{(\Delta+\omega_z)^2+\Omega^2} \tag{3.34d}$$

With the joint Zeeman precession frequency defined as $\omega_z = (g_h + g_e)\frac{\mu_b B_x}{\hbar}$. Each frequency component consists of two "Zeeman-Rabi generalised frequencies" $\Omega_{\mathrm{ZR}}^{\pm} = \sqrt{\left[\Delta \pm (g_h + g_e)\frac{\mu_b B_x}{\hbar}\right]^2 + \Omega^2}$ where the detuning is modified by the energy shift of each transition due to the Zeeman effect (Fig. 3.3b). These frequencies are presented in Figure 3.6 for a magnetic field strength of $B = 0.5$ T and detuning of $\Delta/2\pi = 25$ GHz.



(a) (b)

Figure 3.6: **Ground state precession spectrum as a function of Rabi frequency.** The precession spectrum is computed in the presence of a 0.5 T magnetic field, and a detuning of $\Delta/2\pi = 25$ GHz. (a) Oscillation frequencies with increasing Rabi frequency as described with Equation 3.34. (b) Energy diagram corresponding to observed frequency components.

In the simplifying case where the Zeeman precession frequency is much weaker than the Rabi frequency $\omega_Z << \Delta, \Omega$:

$$\begin{aligned}\Omega_{\mathrm{ZR}}^{\pm} &= \sqrt{\omega_Z^2 \pm 2\omega_Z\Delta + \Delta^2 + \Omega^2} \\ &\approx \sqrt{\pm 2\omega_Z\Delta + \Omega_R^2} \\ &\approx \Omega_R\sqrt{1 \pm \frac{2\omega_Z\Delta}{\Omega_R^2}} \\ &\approx \Omega_R\left(1 \pm \frac{\omega_Z\Delta}{\Omega_R^2}\right) \\ &\approx \Omega_R \pm (g_h + g_e)\frac{\mu_b B_x}{\hbar}\cos(\theta)\end{aligned} \tag{3.35}$$

Where the generalised Rabi frequency is defined as $\Omega_R = \sqrt{\Delta^2 + \Omega^2}$ (Eq. 3.19) and the mixing angle θ is defined as $\cos(\theta) = \Delta/\sqrt{\Delta^2 + \Omega^2}$ (Eq. 3.12). Thus the four frequency components in this limit simplifies to:

$$\omega_a = (g_e - g_h)\frac{\mu_B B_x}{\hbar} + \Omega_R \tag{3.36a}$$

$$\omega_b = -(g_e - g_h)\frac{\mu_b B_x}{\hbar} + \Omega_R \tag{3.36b}$$

$$\omega_c = g_e\frac{\mu_B B_x}{\hbar}\sin^2\frac{\theta}{2} - g_h\frac{\mu_B B_x}{\hbar}\cos^2\frac{\theta}{2} \tag{3.36c}$$

$$\omega_d = g_e\frac{\mu_B B_x}{\hbar}\cos^2\frac{\theta}{2} - g_h\frac{\mu_B B_x}{\hbar}\sin^2\frac{\theta}{2} \tag{3.36d}$$

The frequencies $\omega_{a,b}$ consist of the generalised Rabi frequency Ω_R of each transition split by the magnetic field $\pm(\frac{g_e - g_{h,x}}{2})\mu_B B_x$. Though they do not represent oscillations between the two hole spin states but rather between the dressed states, the frequency components are still present as an overall oscillation between the hole and trion manifold similar to the off-resonant oscillations in Figure 3.2. The frequencies $\omega_{c,d}$ correspond to the precession of the trion manifold and hole manifold respectively, which can be confirmed when the effect of the laser is removed by taking $\Omega \to 0$ ($\theta = 0$). This holds true even for the general case (Eq. 3.34). This results in $\omega_c \to g_e\mu_B B_x/\hbar$ and $\omega_d \to g_e\mu_B B_x/\hbar$. The opposing sign of each manifold's precession frequencies are a reflection of the corresponding g factor, which causes the hole to precess in the opposite direction to the trion. At non-zero laser powers $\Omega \neq 0$, the trion and hole precession frequencies mix, with proportions equal to the population of ground and excited states in each dressed state manifold (Eq. 3.13).

At higher Rabi frequencies, the two precession frequencies ω_c, ω_d converge to a common value $(g_e - g_h)\mu_B B_x/\hbar$. This behaviour suggests an equal mixing of hole and trion frequencies at high laser intensities corresponding to $\theta = \pi/2$, where $\Omega >> \Delta$.

The hole precession frequencies are thus shown to be perturbed by the application of the Stark field. Analogous to the two-level system, the ground state hole and excited state trion manifolds are mixed through the light-matter interaction. This results in the hole-like dressed state precessing at a modified rate depending on the mixing angle of the dressed state. As the hole and trion possess opposite signs, the mixing effectively reduces the magnitude of the hole precession rate up to a zero crossing point where the trion and hole precession negate each other as shown in Figure 3.6a.

3.5 Outlook

Enhancing the generation rate of spin-photon entangled cluster states using the AC Stark effect requires two key considerations: preserving transition frequency indistinguishability and maintaining sufficiently high spin precession rates. Increased magnetic field strengths increases the precession rate, however splits the energy of each transitions into two distinguishable frequencies. Analysis of the combined effects of a magnetic field and AC Stark field on both transition and spin precession frequencies in this chapter indicates that an appropriate selection of magnetic field strength, detuning, and Rabi frequency allows for an enhanced precession rate while maintaining transition indistinguishability. Figure 3.7 compares the spin precession rates used for generating spin-photon entangled cluster states with those achievable through the proposed approach. For a detuning of $\Delta/2\pi = 25$ GHz, significantly higher precession rates can be achieved at low Rabi frequencies compared to existing methods. However, the AC Stark effect must be sufficiently strong to maintain transition frequency indistinguishability. The required Rabi frequencies are indicated on each precession rate curve with an "x" along with the associated precession frequency. As the magnetic field strength increases, higher Rabi frequencies are needed to compensate for the growing Zeeman splitting. Consequently the precession rate enhancement diminishes at higher magnetic fields, converging with the literature value at 0.75 T. The optimal enhancement occurs at 0.25 T, where the precession rate is doubled compared to the previously reported value. Furthermore, the solid lines on each curve indicate where the excited state population of the ground-like dressed state is lower than 15%, ensuring that excessive spontaneous decay from the excited state component does not pollute the entanglement protocol.

These preliminary results point towards the viability of this approach in enhancing the generation rate of spin-photon entangled cluster states. The demonstrated ability to manage the trade-off between increased precession rates and spectral distinguishability paves the way towards enhanced coherent control of quantum systems in the presence of a range of limiting factors. Further theoretical work may be directed towards a complete simulation of the entanglement generation protocol with the applied AC Stark field, and determining if the Stark field affects the entanglement fidelity of the

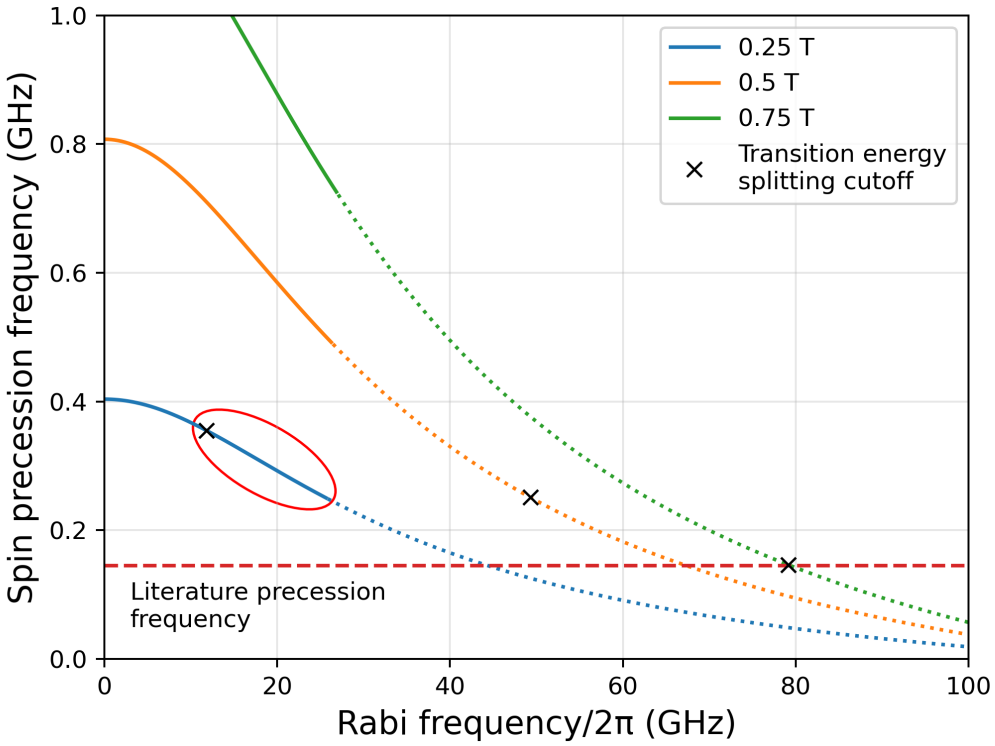


Figure 3.7: **Precession frequency magnitudes of the hole-like dressed state manifold at various magnetic field strengths and Rabi frequencies with a laser detuning of $\Delta/2\pi = 25$ GHz.** Increasing magnetic fields increase the hole precession frequency, while increasing Rabi frequencies decrease it. Solid lines indicate where the excited state population is less than 15%, while dotted lines denote higher excited state populations. The precession rate of the hole used for generation of entangled spin-photon states in the literature [98] is marked with a dashed red line for reference. The Rabi frequencies where the transition energies are considered effectively indistinguishable are denoted for each magnetic field curve with an "x" (c.f. Fig 3.5). For 0.25 T this marks the upper limit of the ideal region (red) where the transition frequencies are indistinguishable, excited state population is low, and the spin precession frequency is roughly double the previous literature value.

overall state including any decoherence effects induced from the applied laser such as polarisation of the Overhauser field [99]. Future work, including the focus of the next chapter, aims to experimentally validate these theoretical findings. A key step in this validation is the design and assembly of an experimental setup capable of precisely measuring the combined effects of the magnetic field and AC Stark laser on the QD system. This requires both a high-precision optical spectroscopy system and a reliable method for applying and controlling a magnetic field around the QD sample. Significant progress has already been made toward constructing this setup, including the design and integration of key components necessary for accurate measurement. The details of this progress, along with the challenges encountered and potential refinements, will be discussed in the following chapter.

Chapter 4

Experimental progress

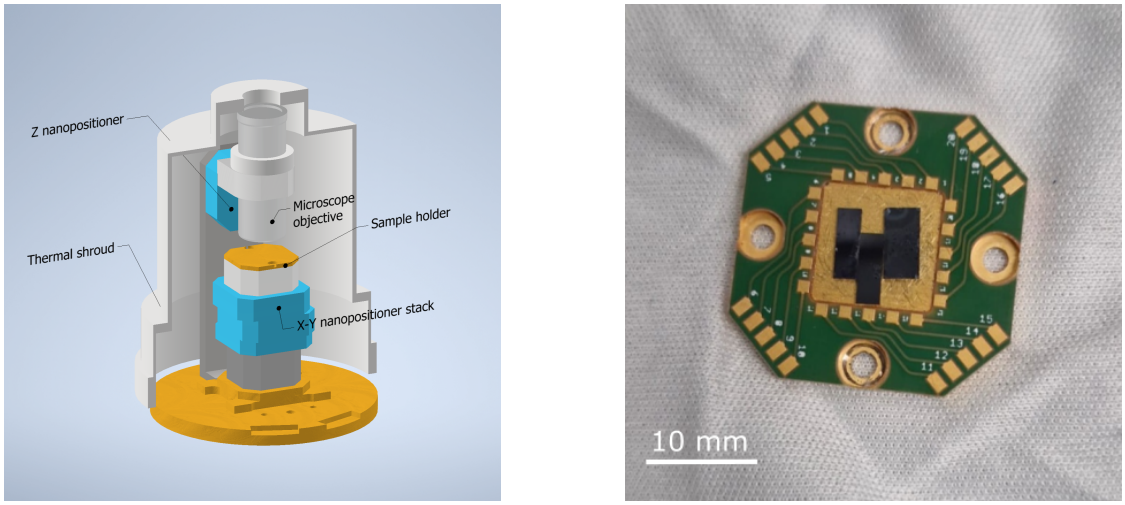
This chapter outlines the design and construction of the experimental system used in this work, including the cryogenic system used to mount the QD samples, the optical spectroscopy system, and the laser systems. Individual components of interest are discussed, including the working principles and any calibration efforts undertaken. Using the assembled system, preliminary characterisation data of a QD sample was taken. This includes above-band photoluminescence to identify emission lines arising from confined charge carriers and time-resolved photon counting to measure the temporal decay profile of the confined states. All systems were jointly designed and assembled by Satya Undurti, Nicole Blaess, Declan Gossink, Tim Wohlers-Reichel, and the author.

4.1 Experiment design

4.1.1 Cryogenic system

The cryogenic system used in this work is the Attocube attoDRY800, which cools the sample to 4 K with a closed cycle liquid helium compressor. A large vacuum shroud (LT-APO, pictured in Figure 4.1a) with dimensions 37 mm radius by 98 mm height allows for the installation of x-y nanopositioners and a high numerical aperture (NA) microscope objective (NA = 0.81, working distance = 0.7 mm). The ANP101 nanopositioners function through a stick-slip piezoelectric mechanism providing 5 mm of travel distance at sub-micron resolutions. Thermalised electrical feedthroughs are provided for both DC and RF signals to the sample stage, enabling voltage biasing of the samples. GaAs/AlGaAs QD samples were loaded onto the 5x5 mm gold contact area on the sample stage (Figure 4.1b) and cemented with vacuum grease, which solidifies at cryogenic temperatures.

The nanopositoners function through a slip-stick mechanism, where a piezoelectric actuator expands or contracts when a sawtooth wave is applied to it. The ramping



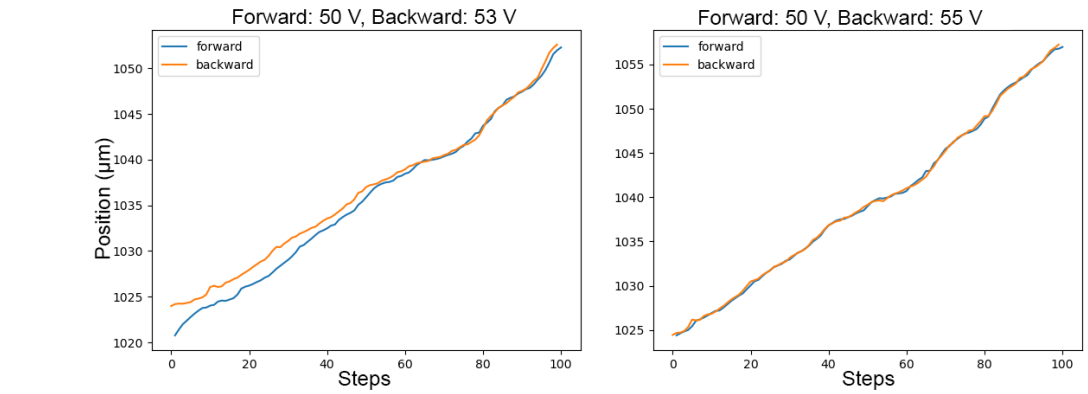
(a) (b)

Figure 4.1: **Cryostat and sample preparation.** (a) Render of AttoDRY800 vacuum shroud and nanopositioner assembly. (b) Three QD samples prepared for loading into cryostat.

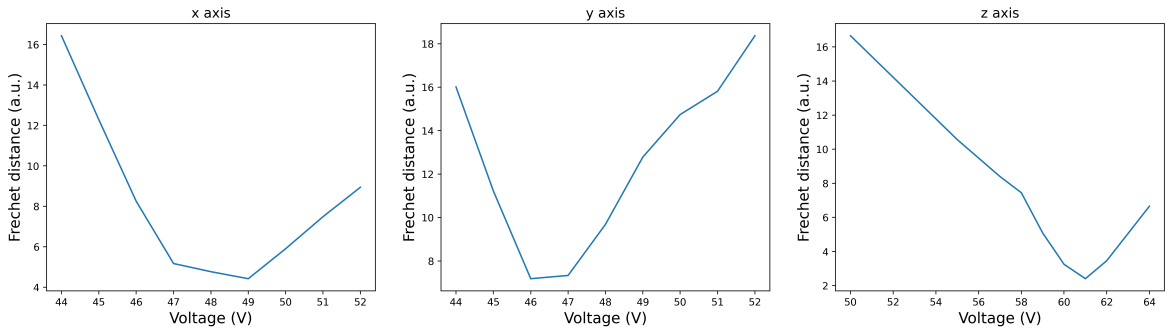
section of the saw tooth wave causes the piezo component to expand slowly, causing the active region of the positioner to "stick" with the piezo due to friction and move along with it. The rapidly falling part of the sawtooth causes the piezo to retract quickly, causing the contact between the piezo and active region to "slip". Repeating these two steps with a constant sawtooth wave allows for the active region to travel a theoretically infinite distance barring external limitations.

The nanopositioners are capable of both open loop and closed loop operation. In open loop mode, motion executed step by step, with the distance covered in each step determined by the magnitude of the applied voltage. In closed loop mode, position control is achieved through a proportional-integral-derivative (PID) control loop. This function continuously monitors the current position and compares it to the desired position. The movement is then adjusted accordingly until the target position is reached. Though suitable for travelling to targeted positions at distances requiring a large number of single steps, this feature was not used for precise positioning of QDs below the microscope objective due to the continuous adjustments taken around the desired position from the PID loop. A notable feature of the piezoelectric nanopositioners in open loop mode is the hysteresis experienced between the forwards and backwards direction of travel (Fig. 4.2a), typical of all piezoelectric actuators. This introduces challenges when locating QDs, as a single forward and backward step does not return the sample to the same position under the objective. Furthermore, it was noted that the length of each step varied at different positions, leading to overall non-linear translational

motion. To mitigate this, the applied voltage can be adjusted when changing direction. The calibration of required voltage amplitudes were determined by recording the position during both forward and backward motion. While the forward voltage was held at 50 V, the backward was varied to identify the optimal voltage compensation. The Fréchet distance [108], a measure of the similarity between two curves, between the forward and backward paths was minimised to determine the required voltage (Fig. 4.2b.



(a)



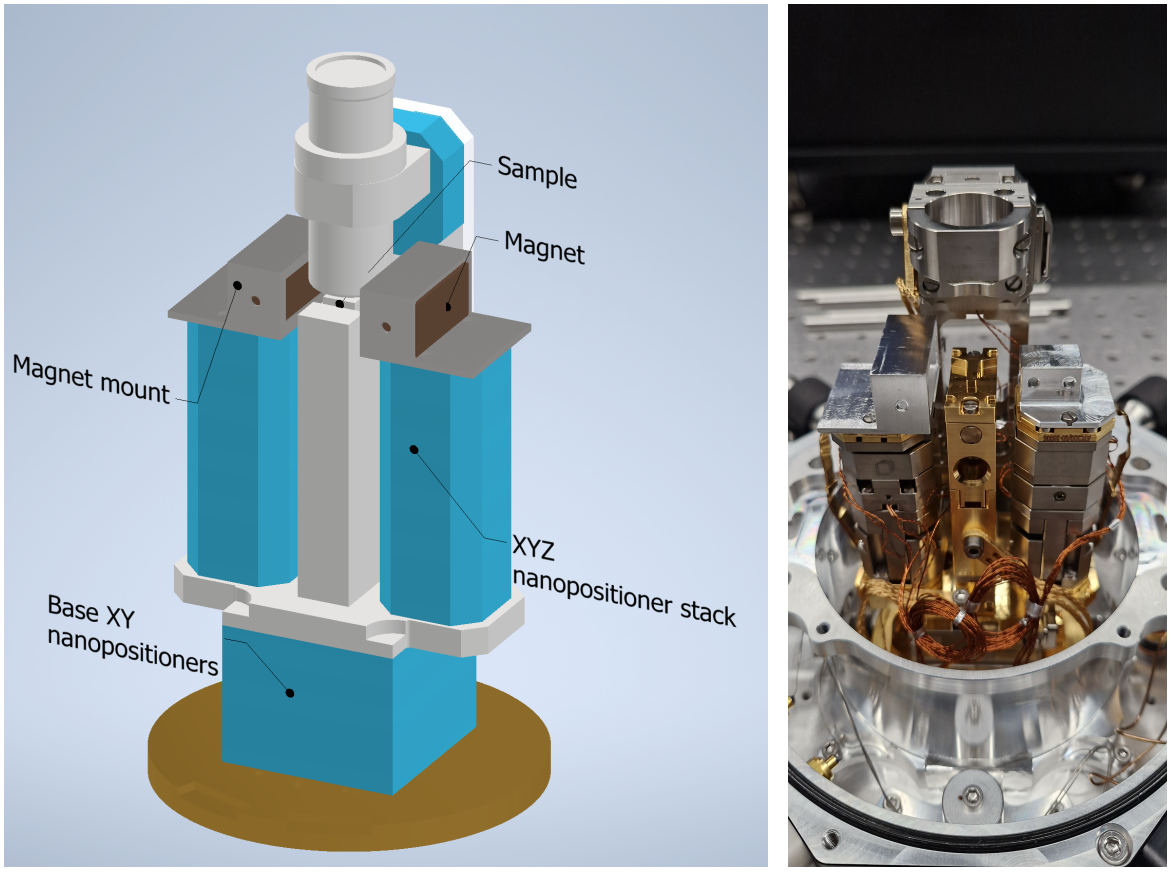
(b)

Figure 4.2: **Calibration of Attocube XYZ nanopositioners.** (a) Backwards and forwards motion of x-axis piezo nanopositioners at various voltages. A (b) Fréchet distance between the forward and backwards motion for each nanopositioner. Minima correspond to the optimal backward voltage given a forward voltage of 50V.

The x and y nanopositioners could thus be programmed to travel the same distance backwards and forwards by adjusting the voltage before moving, and such features were implemented with a custom python script that was developed. The z nanopositioner controlling the height of the objective above the sample had a considerable difference in backwards and forwards positioning, likely resulting from combating gravity in one

direction. It was also noted that the voltage calibrations for each direction and axis would need to be completed after each sample exchange procedure.

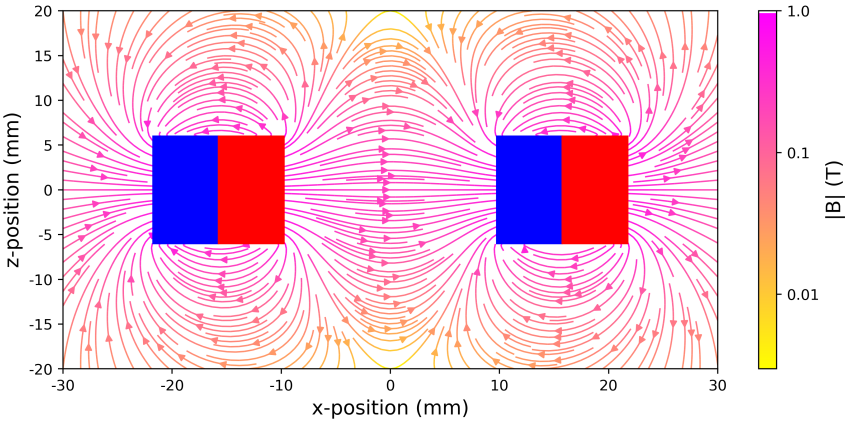
4.1.2 Magnet assembly



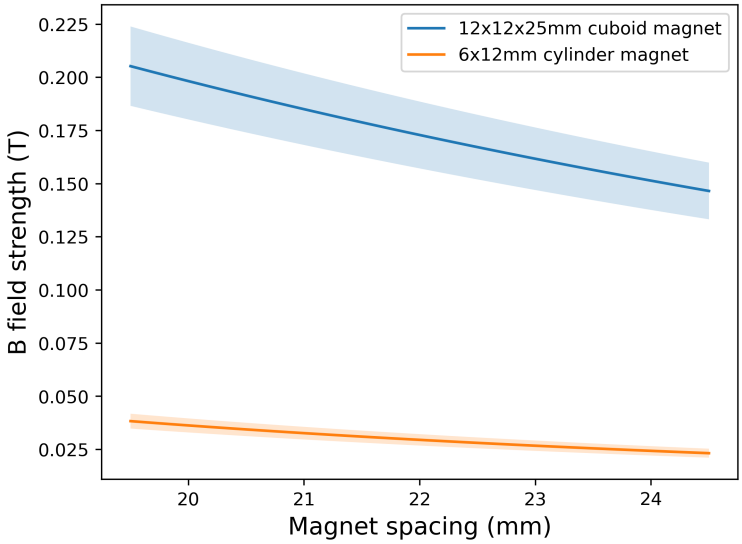
(a) (b)

Figure 4.3: **Design of the magnet mounts**. (a) Render of PPS nanopositioner and sample assembly. Fibre holders mounted onto the XYZ nanopositioner stack have been replaced with magnet mounts, providing some but limited control over air gap between magnets. (b) PPS cryostat with machined cuboid (left) and cylinder (right) magnet holders mounted on the nanopositioner stack. Microscope objective is not present in image.

Implementation of the Lindner and Rudolph protocol requires the application of a stable magnetic field to the QD. Furthermore, a variable magnetic field enable probing and characterisation of various spin states in a QD such as measurements of the g factor of various carriers. To accomplish this, a tunable magnetic field assembly contained



(a)



(b)

Figure 4.4: **Simulation of the magnetic field mount.** (a) Simulated magnetic field in x-z plane for a pair of 12x12x25 mm cuboid magnets with spacing 19.5 mm. (b) Peak magnetic field strengths between magnets as the spacing between magnets increase.

within the existing cryostat is desired. Two general designs were considered in order to achieve magnetic field strengths on the order of 100s of millitesla: an electromagnetic coil design such as a Helmholtz coil, or a permanent magnet assembly. The coil option was ruled out early into the design phase as a standard resistive coil would produce heat within the cryostat increasing the overall base temperature, and the design and

manufacture of a stable and compact superconducting solenoid would be beyond the budget and time-frame allotted to the candidature. To achieve a tunable magnetic field using a permanent magnet array, adjusting the spacing between magnets is the most straightforward approach. This assembly was designed around the Attocube photonic probe station (PPS) cryostat, which featured two XYZ nanopositioner stacks adjacent to the main sample stage. Originally designed to hold and position optical fibres for in-plane excitation of the sample, the nanopositioners were repurposed to accommodate custom machined permanent magnet holders with an appropriate mounting design. To date the PPS cryostat and magnetic field assembly have not yet been used in spectroscopic experiments as it was discovered that the stock nanopositioners supplied could not overcome the attractive strength between the magnet pairs. Consultations and redesign in collaboration with the manufacturer is currently ongoing to overcome this challenge.

To achieve high magnetic field strengths, the strongest grade samarium cobalt (Sm_2Co_{17}) magnets were selected. SmCo magnets feature high stability and reduced demagnetisation at low temperatures when compared to the common rare-earth neodymium-iron-boron magnets. Such magnets undergo the spin-reorientation transition at temperatures below 135 K, resulting in a rapid decrease in remanence and shift in magnetization direction [109]. In contrast, the remanence of SmCo magnets do not undergo the spin-reorientation transition resulting in a remanence of 1.2-1.09 T at 4 K [110]. Such a system was employed by Steindl et al [111] to address quantum dots embedded in a microcavity, employing a pair of static 9x9 mm SmCo cylindrical magnets with an air gap of 4.5 mm that achieves 475 mT at 5 K. Given the geometry of the nanopositioner, sample stack, and diameter of the microscope objective, the achievable air gap for our setup ranges from 19.5 mm to 24.5 mm. To reach comparable magnetic field strengths, a larger 25x12x12 mm cuboid magnet was used in the design. Additionally, a smaller 6x12 mm cylindrical magnet mount was designed for lower magnetic field strengths. For both magnet geometries, a custom mount to attach the magnetics to the nanopositioners were designed (Fig. 4.3). Magnetic field simulations were performed using the MagPyLib package in Python [112], yielding field strengths of 225 mT to 150 mT with the large magnet and 40 mT to 25 mT for the smaller one (Fig. 4.4). Such values are suitable for the Lindner and Rudolph protocol in QDs, with the smaller field strength aligning with previous implementations and the larger field strength enabling the faster precession rate proposed in this work.

4.1.3 Laser systems

Ti:Saph laser

Above band excitation and implementation of the AC Stark effect requires the use of a wide-tunable near-infrared CW laser, ideally exhibiting good frequency and power

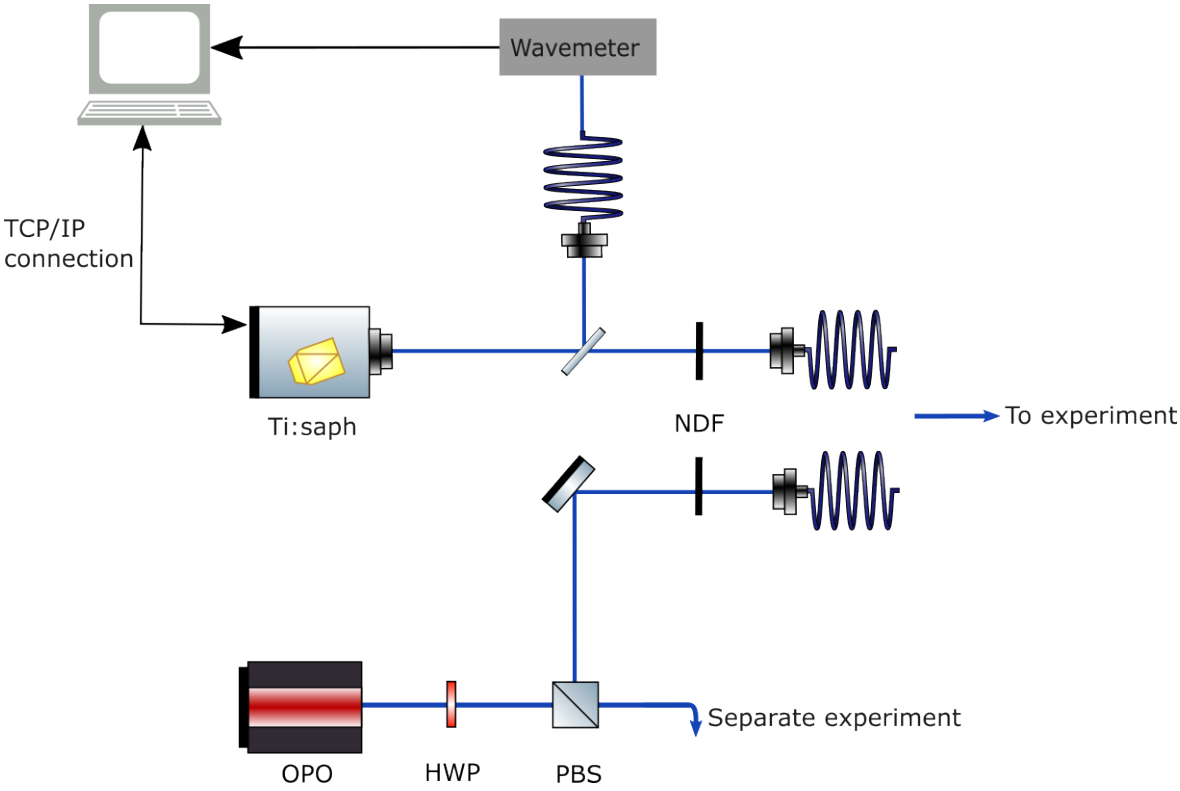
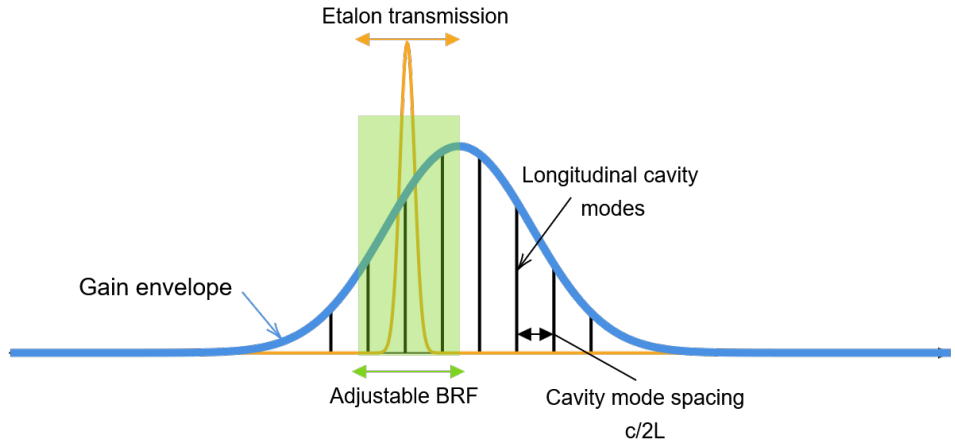


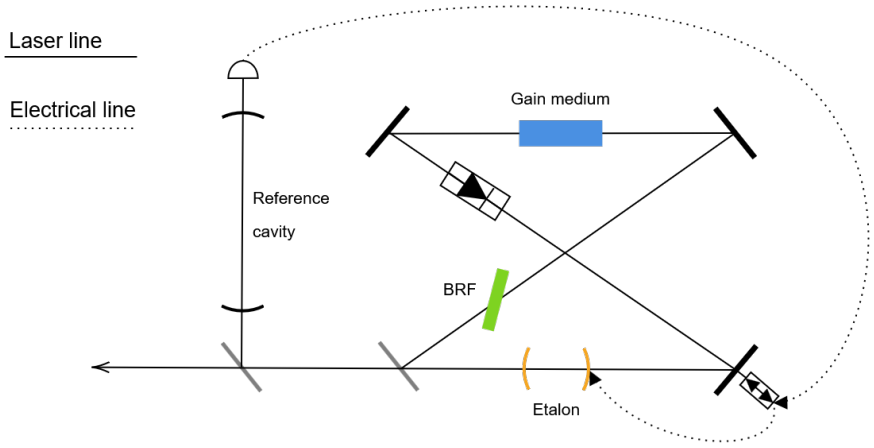
Figure 4.5: **Schematic diagram of the laser setup**. Setup was located on a separate table to the experiment for stability. The two main lasers used were a pulsed laser (OPO: optical parametric oscillator) and CW laser (Ti:saph). Abbv. used: HWP—half wave plate, PBS—polarising beam splitter, NDF—neutral density filter.

stability as the AC Stark shift is sensitive to both. The laser currently used is a M-Squared SolsTiS titanium sapphire (Ti:saph) laser tunable between 700 nm and 900 nm, which is suitable for the QD samples that emit at 750-800 nm for the droplet QDs, and 900-1000 nm for the self assembled QDs [113]. The Ti:saph gain medium (Fig. 4.6a) has a broad emission range from 670 nm to ∼1000 nm, with the lasing wavelength determined by the longitudinal modes supported by the internal bow-tie ring cavity (Fig. 4.6b). With just the gain medium and cavity, the laser would oscillate between multiple cavity modes. As such additional wavelength-dependent losses are introduced into the system to reduce the allowed modes. Adjusting the transmission wavelength of the loss-inducing elements changes the allowed lasing modes, resulting in a tunable wavelength laser. The first stage of wavelength-dependent loss is through a birefringent filter (BRF), where changing the angle of the filter allows for a coarse wavelength tuning. The incorporation of an étalon adds additional loss with a narrower transmission range than the BRF, enhancing the laser linewidth and enabling fine

wavelength tuning through modulating the étalon length.



(a)



(b)

Figure 4.6: **Principle of operation of the Ti:Saph laser.** (a) Illustration of lasing of a single longitudinal mode. The overall gain envelop from the titanium sapphire material is pictured in blue. Losses in the system are introduced through an adjustable birefringent filter (BRF, green) and a thin étalon (orange). Changing the angle of the BRF allows for coarse wavelength tuning, while changing the étalon length provides fine tuning. The resulting laser frequency results from the gain and loss overlap of all components. (b) Ti:saph laser schematic with coloured components corresponding to the gain profiles in (a). Feedback from the reference cavity is fed to the bow-tie cavity mirror.

Laser frequency stabilisation is accomplished by electronically locking the etalon

peak transmission to the closest longitudinal mode, minimising the risk of mode-hopping. After the lock is engaged, wavelength tuning is accomplished by adjusting the bow-tie cavity length via a piezo mounted mirror. This modifies the longitudinal modes, "dragging" the etalon peak transmission along with the locking electronics to maintain single longitudinal mode lasing. The linewidth is further refined by referencing the bow-tie cavity length to feedback from an external reference cavity. A photodiode detects the beat signal between the laser and reference cavity frequencies, generating an error signal that is used to fine-tune the bow-tie cavity length and stabilising the laser frequency. By adjusting the reference cavity length, the laser frequency can be precisely scanned.

The Ti:Saph laser used here is an older model on loan from another laboratory, with several components malfunctioning or not operating as intended. While both the BRF and étalon remained tunable, the étalon electronics were unable to reliably lock onto the nearest cavity mode. Additionally, the reference cavity module was non-functional, preventing precise frequency scanning and frequency stabilisation. As a result, the laser exhibited mode-hopping and frequency drift over extended periods. To address these limitations, a workaround was implemented by referencing the laser to an external wavemeter[1]. Custom software was developed by the author to compare the desired laser wavelength with the actual output and adjust the etalon length accordingly. This process involved a multi-step tuning approach: initial coarse tuning with the BRF, followed by fine adjustment using the etalon. The mode-hop-free region of the etalon was then identified, ensuring that the selected longitudinal mode remained within the linewidth of the etalon transmission peak as the etalon length was varied. Once the region was identified, the frequency difference between desired and actual laser output was used as an error signal in a PI control loop. This would continuously adjust the étalon length within the stable mode-hop-free region to minimise the error signal. While rudimentary, the laser exhibited significantly improved frequency stability for minutes at a time, an improvement of several orders of magnitude compared to the unstabilised laser.

One limitation of this approach is the lengthy initial wavelength tuning time, as well as locating the mode-hop-free region of the etalon. Depending on performance, the time taken to engage the PI control loop section of the protocol would take up to 15 minutes for a single desired frequency. The main source of time delay is likely due to the digital TCP/IP ethernet connection between the controlling PC and the laser control system. A significant portion of time was taken in the communication of each tuning signal sent to the laser, potentially due to the age of the control system. An alternative approach would be to direct the wavemeter error signal to an analog feedback loop directly controlling the cavity length, bypassing the ethernet connection which would result in a considerable speed improvement. As of time of writing, continuous frequency scanning

[1] HighFinesse WS6

with the external wavemeter feedback intervention has also not been implemented.

OPO laser

In addition to the CW laser, an optical parametric oscillator[2] (OPO) was used in this work. The OPO outputs a broadly wavelength-tunable pulsed laser from 600 nm to 2300 nm at 80 MHz or one pulse every 12.5 ns, with pulse widths around 8 ps at 800 nm. This was used as an alternative to the Ti:saph laser for photoluminescence measurements, as well as QD lifetime measurements. Both lasers were sited on a central optics table along with a 633 nm diode laser[3] used for beam alignment, as depicted in Figure 4.5. Said lasers were collimated into a single-mode fibre which was brought to the experiment table with the housed cryostat. The OPO's laser power was reduced with a combination of polarisation filtering with a half-wave plate and polarising beam splitter, and with neutral density filters, which lowered the input laser power to below the damage threshold of the single mode fibres. The Ti:saph laser only used neutral density filters as the output power could be lowered by controlling the pump power.

4.1.4 Optical measurement elements

Spectrometer

QD spectroscopy was conducted with an 0.5 m long Andor Shamrock 750 spectrometer, which utilised a reflecting diffraction grating to split the emission into its constituent wavelengths. The spectrometer was equipped with a motorised rotating turret with 3 reflecting diffraction gratings at various grooves per mm, allowing for a range of wavelength resolutions. An Andor iDus CCD camera at the end of the optical emission path captured the resulting emission spectrum. Sweeping of the wavelength range captured by the CCD was achieved by adjusting the angle of the diffraction grating electronically. For single photon collection, the spectrometer was equipped with a motorised flip mirror that would redirect the emission from the CCD at the end of the spectrometer to an exit slit on the side of the housing.

Single photon counting assembly

For single photon detection, a superconducting nanowire single photon detector (SNSPD)[4] was used. The use of an SNSPD over a standard avalanche photodiode or other single photon counters was chosen due to the lower dark counts, high detection efficiency and greater time resolution [114]. The SNSPD incorporates a superconducting material patterned into a meandering nanowire. A current is applied, with the magnitude

[2] APE Levante Emerald
[3] ThorLabs LP633-SF50
[4] Single Quantum Excellence

below the critical current of the superconducting material where regular conductivity is restored. Absorption of a single photon disrupts the local superconductive state, resulting in a resistive hotspot. The increased resistance is greater than the resistance of the readout amplifier, resulting in the current redirecting to the readout. This generates a voltage pulse from the amplifier, which is then sent to a time-tagger [5]. With the trigger signal from the pulsed laser, the time tagger tracks the timing of arrival of each photon relative to the trigger. Although the time tagger offers a minimum bin size of 2 ps, the overall time resolution is limited by the 15 ps timing jitter of the SNSPD. This level of precision remains sufficient for measuring the temporal profile of quantum dot emission, which typically occurs on hundreds of picosecond timescales. This setup thus enables precise time-resolved measurements of single-photon emission events with high detection efficiency and temporal resolution.

4.1.5 Optical setup

The emission wavelength of quantum dots are variable and depends on the exact growth conditions, dot geometry, and material choice. In order to identify suitable QDs for experiments, a spectroscopic system was designed around the cryostat embedded in an optical table. The pump laser was delivered from the central laser table (Fig. 4.5) and directed to the microscope objective within the cryostat, creating electron-hole pairs. Subsequent recombination within the sample resulted in photon emission, which was then collected by the objective.

Figure 4.7 is a schematic of the optical breadboard setup used for QD spectroscopy. A combination of a half wave plate, polarising beam splitter, and ND filter wheel control the power of the pump laser continuously before it enters the 90:10 beamsplitter. The 90:10 BS reflects 10% of the pump beam into the objective, further cutting down the laser power. Electron-hole pairs are generated in the area of the sample illuminated by the focused laser. For non-resonant excitation, non-radiative and radiative processes lead to generated electrons and holes in the QDs forming exciton states. If the excitonic spin states favour dipole-allowed radiative recombination, spontaneous emission resulted in light emitted at various wavelengths depending on the specific exciton. Recombination through other states and structures such as in quantum wells or other impurity states were also present. The emission is collected through the same microscope objective and directed through the 90:10 BS where a majority of the emitted light gets transmitted. The beam was then expanded through a x4 telescope, and focused onto the entrance slit of the reflection spectrometer[6]. The beam expander was placed to ensure the emission beam completely filled the diffraction grating within the spectrometer, and a high-pass filter removed the majority of the pump beam. De-

[5] Swabian instruments time tagger X
[6] Andor Shamrock 750

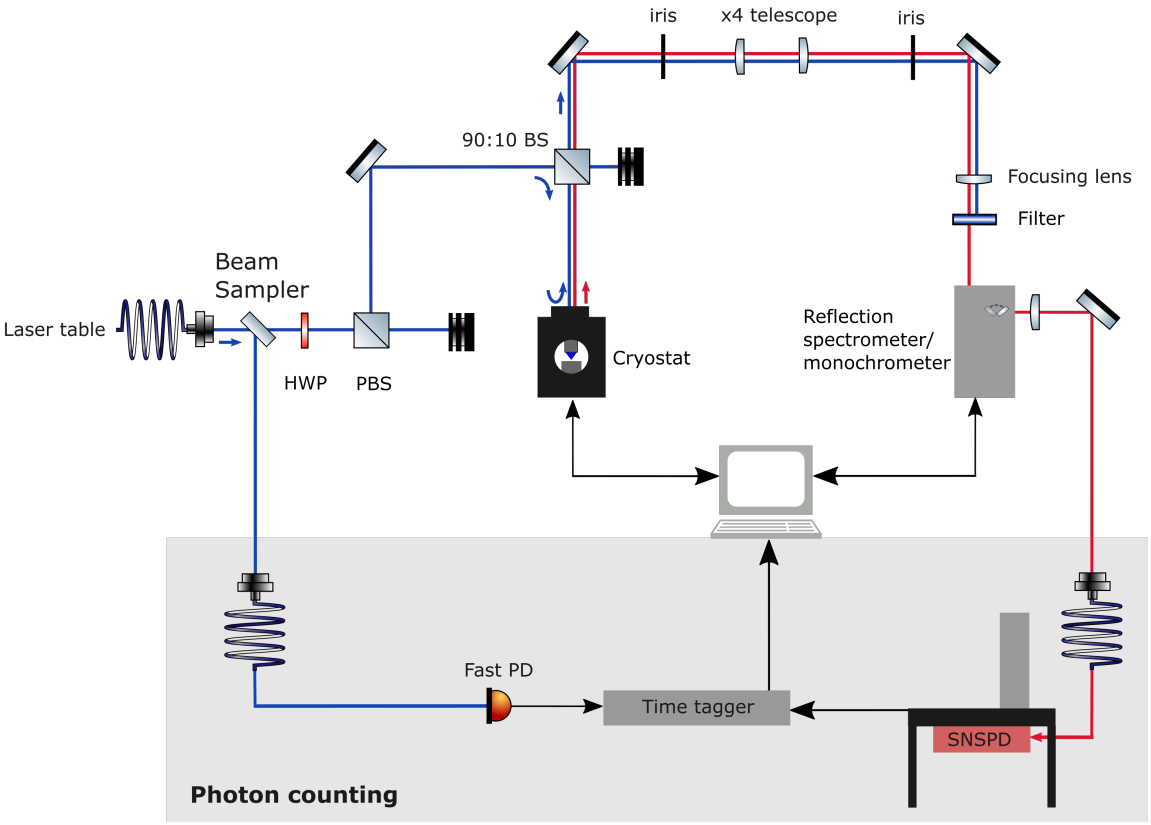


Figure 4.7: **Optical setup used in probing single quantum dots.** The spectrometer has an internal motorised flip mirror directing the beam to an output slit, allowing the system to act as a monochrometer. Abbv. used: 90:10 BS—90:10 transmission/reflection beam splitter, PD—photodiode, SNSPD—superconducting nanowire single photon detector.

pending on the desired experiment, the diffracted emission would either be sent to the attached CCD in the spectrometer for spectral analysis, or sent to the output slit of the spectrometer to the photon counting assembly. For single photon counting, the outgoing emission beam was coupled into a single-mode fibre and fed into the SNSPD. The SNSPD sends electrical pulses on detection of a single photon which is picked up by the time tagger. When using the pulsed OPO laser, a beamsplitter picking off part of the pump beam sends the pulses to a fast photodiode connected to the time tagger. This functions as a trigger for the emitted photons, enabling time-sensitive experiments such as excited state lifetime measurements.

In practice, a low photon count rate in the SNSPD was observed and required high integration times for data acquisition. This is likely due to several contributing

factors. The low transmission efficiency (0.3) of the diffraction gratings significantly reduced photon flux exiting the spectrometer. Furthermore the exit beam profile was considerably non-gaussian, as measured with a camera. This limited the coupling efficiency into the single mode fibre and reduced the number of photons entering the SNSPD through the fibre. Workarounds are currently under development as of time of writing, such as assembling a transmission spectrometer or employing a volume Bragg grating to isolate the QD emission and reject other spectral lines. Such methods would bypass the present spectrometer and minimise the loss in signal from such elements. Further inefficiencies arise from the isotropic emission of the quantum dots, where photons are emitted in all directions. Due to the limited solid angle coverage of the objective lens, only a small fraction (approximately 1%) of the emitted photons are collected [115]. The incorporation of a micro-cavity around the QD would greatly enhance the collection efficiency through the Purcell effect, directing emission towards the objective.

4.2 Photoluminescence spectroscopy on QD samples

4.2.1 Micro-photoluminescence spectroscopy

Above-band micro-photoluminescence (PL) spectroscopy was conducted on the QD sample using the setup outlined in Figure 4.7. Compared to bulk photoluminescence, single emitters were illuminated with an objective (working distance 0.7 mm, focal length 2.93 mm) focusing a 705 nm laser (10 nW) to a spot size of approximately 4 μm^2. This generated electron-hole pairs far above the band gap of the bulk AlGaAs crystal and diffuse throughout the material before recombination. The exact recombination wavelength was dependent on the local semiconductor structure at the site of recombination. This results in a wide range of emission wavelengths, which provides insight into the structures present in the sample and permits identification of the various QD emission lines.

Two diffraction gratings were used to analyse the emission spectra of the QD sample, where different lines per mm of each grating allowed for two different wavelength ranges. The lower resolution grating had 300 lines per mm, resulting in a resolution of 65 pm per pixel. With a centre wavelength of 770 nm, the spectrometer and CCD camera configuration allowed for a wavelength window from 708 to 829 nm. This provided a wide enough window to search for the quantum dot emission while scanning with the x-y nanopositioners. The high resolution scan had 1200 lines per mm, providing a resolution of 13 pm per pixel. The spectra was identified by localised features that would grow and recede from view as the position was scanned.

Figure 4.8a depicts a wide-wavelength scan of the spectrum following the location

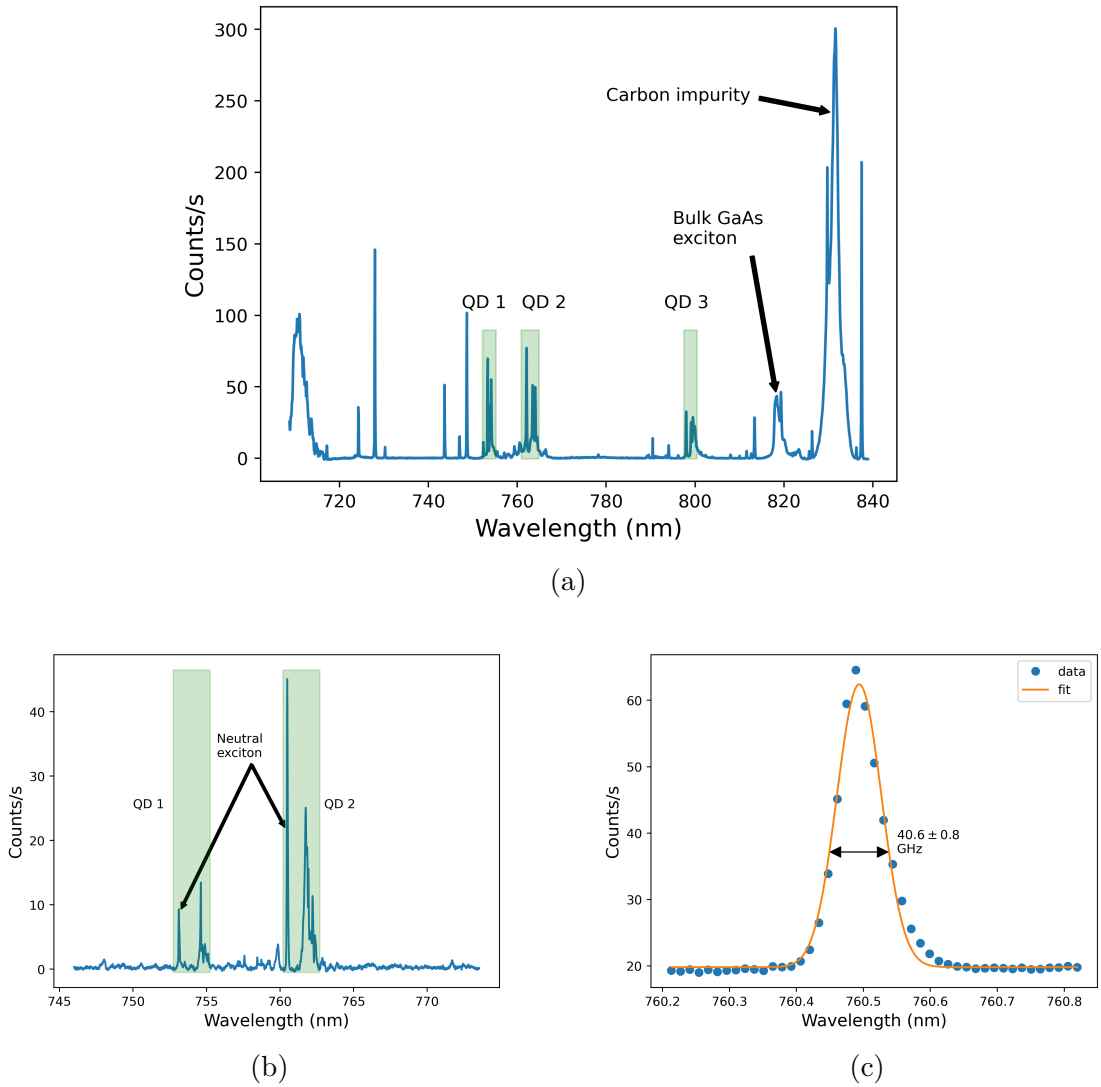


Figure 4.8: **Photoluminescence spectra of a QD sample.** Spectra taken with the sample held at 4 K. (a) PL spectra with several notable features identified. Delta spikes are likely cosmic rays triggering the detector. Other unlabelled features have not yet been definitively identified. (b) Increased resolution spectra of the emission of two quantum dots. The neutral exciton lines are identified by comparison to literature PL spectra. The family of emission lines at higher wavelengths correspond to various exciton states. (c) Emission profile of the neutral exciton. A gaussian with linewidth of 40 GHz is fitted to the emission spectra. A slight asymmetry is present at higher wavelengths, typical of the neutral exciton emission lineshape [116].

of the QD emission lines. Salient features were compared to literature PL spectra for identification. The bright line at 831 nm is likely attributed to carbon impurities substituting As sites in the GaAs crystal structure, where conduction electrons recombine with empty valence states in the carbon atom [117]. The persistent obervation of the carbon impurity line across the scanned sample region, along with the high intensity, suggests significant carbon presence in the sample substrate. Exciton recombination in bulk GaAs is visible at 818 nm, which differ from the band gap energy due to the effect of the exciton binding energy [118]. The labelled QD spectra in Figure 4.8b and 4.8a were identified by the isolated bright neutral exciton, followed by a series of longer wavelength emission lines corresponding to a range of exciton states including the trion [116, 119]. Due to resolution limitations, the biexciton and trion lines could not be clearly resolved among the family of excited states. Finally, a Gaussian fit of the neutral exciton line in Figure 4.8c yielded a linewidth of 78 ± 2 pm, corresponding to a frequency width of 40.6 ± 0.8 GHz at a centre wavelength of 760.49 nm. This linewidth is likely broadened by the above-band pumping scheme, requiring a higher precision measurement protocol such as resonance fluorescence to determine the natural linewidth of the emission [119].

4.2.2 Time resolved photoluminescence

Time-correlated photon counting was used to characterise the decay profile of the neutral exciton. The OPO generates 15 ps width pulses at 80 MHz with a wavelength of 650 nm. 3 µW of power at the objective was used due to the low collection efficiencies of the setup. Prior to entering the objective, a 50:50 beamsplitter divided the excitation beam, with one branch directed to a photodiode connected to the time tagger. This uses the OPO pulses as a timing reference for the photons emitted from the QD. The second branch is directed to the cryostat, where charge carriers are excited above-band as before. The exciton emission line of a single QD was identified with the built-in CCD camera before being redirected to the exit slit, which isolated the exciton line at 760 nm. Emitted photons were then detected by the photon counting setup outlined in Figure 4.7, and a histogram with 5 ps bin width representing the photon emission probability was generated.

The data was deconvolved with the instrument response function, a Gaussian with FWHM 15 ps corresponding to the documented timing jitter of the SNSPD as provided by the manufacturer. The exponential decay of the neutral exciton was observed to contain two decay components as shown in Figure 4.9. The decay times of each component were determined with a least square fit to an exponential decay function $f(t) = Ae^{-t/\tau}$. The first component with characteristic lifetime of $\tau_1 = 0.626 \pm 0.004$ ns matches with existing literature values of radiative recombination rates which range from 0.5 to 1.2 ns in both droplet etched and self-assembled QDs [120, 121, 122], though such lifetimes are highly dependent on size and geometry of the QD itself. This suggests that the

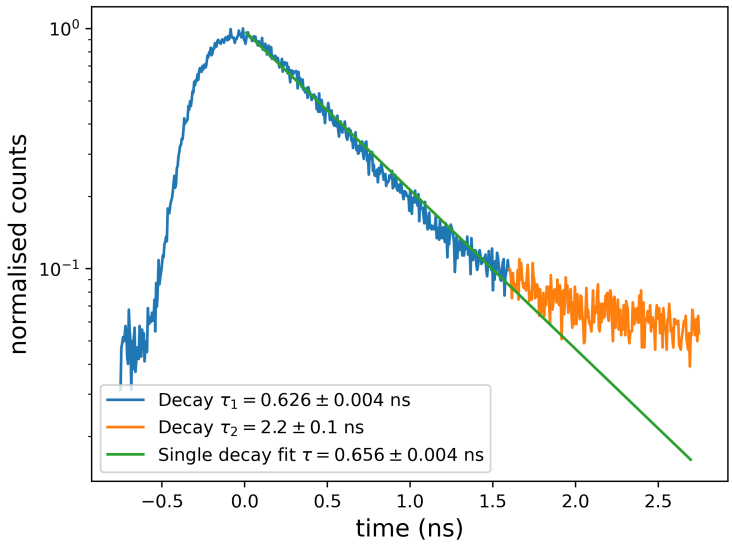


Figure 4.9: **PL decay profile of the neutral exciton.** Profile exhibits two decay components. A single-component decay fit does not match well with the data when plotted on a log scale.

observed lifetime is associated with radiative recombination of the exciton state, where the bright exciton, made of spin anti-aligned electron and hole pairs directly recombine to generate photons. The secondary decay time of 2.2 ± 0.1 ns is attributed to the dark exciton converting to a bright exciton before recombination. This involves the electron in the dark exciton flipping its spin, while the hole remains unperturbed. The exact mechanism is contentious, as various sources attribute this to either interactions with external conduction electrons in the continuum [123] or through a phonon mediated process [121]. In either case, the reported secondary decay times vary greatly, ranging from 2 ns up to 50 ns. The exact secondary decay time likely depends on a combination of several factors, including external voltage biases, excitation wavelength and intensities, and QD geometries. The presence of the secondary decay time also serves as confirmation of the isolation of the neutral exciton, as the trion decay path does not exhibit this secondary decay time [123].

4.3 Outlook and future work

This chapter has documented the first steps towards the construction of a high-precision optical setup for the investigation of semiconductor quantum dots. The completion of which would mark a major milestone in the establishment of a top of the line all-

integrated semiconductor optical QD facility in Australia at the University of Adelaide, enabling rapid prototyping, design, and analysis of solid state single photon emitters.

The next immediate steps are the completion of a cross-polarised measurement system to eliminate the pump laser entirely, while allowing the emitted light through to the collection optics. This would enable more sophisticated experiments such as resonance fluorescence, where transitions are directly excited with the laser. Such experiments could measure the transition linewidth precisely by scanning the laser frequency and would pave the way for resonant pumping of the QD, a crucial step in many communication protocols. Additionally the development of a transmission spectrometer is currently underway to replace the current reflection spectrometer in isolating the desired emission lines and greatly increase the collection efficiencies of the current setup. Once complete, further characterisation of the QD sample will commence. This includes $g^{(2)}(0)$ measurements to certify the single-photon generation capabilities of the sample and Hong-Ou-Mandel experiments to measure photon indistinguishability [119]. Finalisation of the magnetic field enclosure would enable measurement of the Zeeman shift, and pave the way for observation of the combined Zeeman-AC Stark effect.

On the QD sample design front, the integration of a diode structure around the QD would allow voltage biasing, enabling precise control over the charge state of the QD [124]. This would facilitate preparation of the QD in either the neutral exciton or charged exciton state based on the applied bias. The incorporation of QDs into a microcavity structure tuned to the emission wavelength would enhance both the emission rate and emission directionality of the QD, further improving the collection efficiency. It is expected that the development of such structures will commence soon, with initial efforts focusing on fine-tuning fabrication techniques to precisely control the QD emission frequencies.

Chapter 5

Summary and Outlook

The field of quantum communication is advancing rapidly, with ongoing efforts focused on developing scalable and robust methods for generating and manipulating entangled photonic states with high fidelity. One of the key challenges is the distribution of error-resistant entangled states in the face of decoherence and photon loss. Overcoming this challenge is a major step for the realisation of quantum networks and secure quantum cryptographic protocols. In this context, quantum dots offer a pathway toward scalable quantum communication architectures with straightforward integration into photonic devices and boasting on-demand photon generation. The work in this thesis contributes towards broader efforts in the group to establish a world-competitive fully integrated semiconductor optical quantum dot research facility, with the development of in-house capabilities for quantum dot fabrication, characterisation, and integration into quantum technologies. Furthermore, ongoing progress towards enhanced protocols for the generation rate of spin-photon entangled cluster states advances the understanding towards methods of coherent control for QD states in the production of single photons.

- Chapter 2 presented the foundations of quantum information and communication, and outlined the fundamental principles of single photon production in semiconductor quantum dots. The mechanisms for the generation of entangled states in QDs were introduced, along with the Lindner and Rudolph protocol for the production of photonic cluster states. The state of the art for cluster state generation was discussed, followed by a proposal for the enhancement of the Lindner and Rudolph protocol through the optical Stark effect.

- Chapter 3 introduced the AC Stark effect and the four level model of the trion-hole manifold in a QD. Using the QuTiP package, simulations were conducted to model the spontaneous emission process and determine the emission spectrum under the conditions of a combined Zeeman-AC Stark effect. The influence of the AC Stark field on the spin precession rate was investigated, revealing that the applied field induces mixing between the trion and hole manifolds. Consequently,

the hole-like dressed state precesses at a rate modified by the Larmor frequency of the trion manifold. The results confirmed that, with carefully chosen magnetic field strengths, detuning parameters, and Rabi frequencies, greater precession rates can be achieved within practical experimental constraints without sacrificing the spectral indistinguishability of the entangled photon states.

- Chapter 4 outlined the experimental progress towards construction of an optical spectroscopy system capable of measuring the combined Zeeman-AC Stark effect. The assembly process and characterization of key system components were discussed, highlighting the progress toward a high-precision optical measurement setup. Preliminary above-band photoluminescence measurement on a QD sample were conducted, confirming the ability to locate and characterise the spontaneous emission from the QD neutral exciton. Time-resolved photoluminescence enabled a measurement of the decay rate of the neutral exciton, observing a two-component decay profile in agreement with literature.

Future work will focus on completing and refining the experimental setup to enable direct measurement of the predicted effects of the magnetic field and AC Stark field. This will involve finalizing the optical spectroscopy system, enabling high-precision measurements to detect the shift in emission frequencies. Additionally, extending the simulations to account for environmental decoherence effects such as the presence of the nuclear Overhauser field would be a crucial next step, along with the complete modelling of the modified Lindner and Rudolph protocol. Ultimately, the simultaneous application of magnetic and AC Stark fields presents a promising strategy for enhancing the generation of spin-photon entangled cluster states. This work demonstrates the feasibility of this approach, establishes a clear pathway for its experimental realization, and contributes valuable insights into the development of scalable quantum communication technologies.

Appendix A

Appendix of Chapter 3

A.1 Derivation of the rotating wave approximation

The interaction Hamiltonian in the Schrödinger picture is written in Equation 3.6:

$$H_{\text{int}} = \frac{\hbar\Omega}{2}\Big(\left(e^{-i\omega_L t} + e^{i\omega_L t}\right)|e\rangle\langle g| + \left(e^{i\omega_L t} + e^{-i\omega_L t}\right)|g\rangle\langle e|\Big) \tag{A.1}$$

A transformation to the interaction picture is given by the unitary operator:

$$\begin{aligned} U &= e^{iH_0 t/\hbar} \\ &= e^{-i\omega_0 t/\hbar}|g\rangle\langle g| + e^{i\omega_0 t/\hbar}|e\rangle\langle e| \end{aligned} \tag{A.2}$$

Where H_0 is the free Hamiltonian (Eq. 3.1). The matrix exponential is computed through Sylvester's formula $f(A) = \sum_{i=1}^{k} f(\lambda_i)A_i$ for a given matrix A, λ_i are the eigenvalues of A, and $A_i = \prod_{j=1,j\neq i} \frac{1}{\lambda_i - \lambda_j}(A - \lambda_j I)$. The unitary transformation is given as:

$$\begin{aligned} H_{\text{int}} \to \tilde{H}_{\text{int}} &= UH_{\text{int}}U^\dagger + i\hbar\dot{U}U^\dagger \\ &= -\frac{\hbar\Omega}{2}(e^{-i\omega_L t} + e^{-i\omega_L t})e^{-i\omega_0 t}|e\rangle\langle g| - \frac{\hbar\Omega}{2}(e^{-i\omega_L t} + e^{i\omega_L t})e^{i\omega_0 t})|g\rangle\langle e| + 0 \\ &= -\frac{\hbar\Omega}{2}(e^{-i(\omega_L+\omega_0)t} + e^{-i(\omega_L-\omega_0)}|e\rangle\langle g| - \frac{\hbar\Omega}{2}(e^{(i(\omega_0-\omega_L)} + e^{i(\omega_0+\omega_L)t})|g\rangle\langle e| \end{aligned} \tag{A.3}$$

The rotating wave approximation in this case corresponds to discarding the exponential terms containing $(\omega_0 + \omega_L)$. Defining the detuning as $\Delta = \omega_0 - \omega_L$, the interaction Hamiltonian in the interaction picture is:

$$\tilde{H}_{\text{int}} = \frac{-\hbar\Omega}{2}e^{-i\Delta t}|e\rangle\langle g| - \frac{\hbar\Omega}{2}e^{i\Delta t}|g\rangle\langle e| \tag{A.4}$$

Transforming back to the Schrodinger picture and including the unperturbed Hamiltonian yields:

$$H_0 + H_{\text{int}} = -\frac{\hbar\omega_0}{2}\left|g\right\rangle\left\langle g\right| + \frac{\hbar\omega_0}{2}\left|e\right\rangle\left\langle e\right| - \frac{\hbar\Omega}{2}e^{-i\omega_L t}\left|e\right\rangle\left\langle g\right| - \frac{\hbar\Omega}{2}e^{-i\omega_L t}\left|g\right\rangle\left\langle e\right| \tag{A.5}$$

The time dependence of the total Hamiltonian is removed by another unitary transformation to a rotating reference frame with frequency ω_L, with unitary transformation operator $U = \exp\frac{-i\omega_L t(|g\rangle\langle g| - |e\rangle\langle e|)}{2}$:

$$\begin{aligned}
H \to \tilde{H} &= UHU^\dagger + i\hbar\dot{U}U^\dagger \\
&= \Big(\frac{-\hbar\omega_0}{2}\left|g\right\rangle\left\langle g\right| + \frac{\hbar\omega_0}{2}\left|e\right\rangle\left\langle e\right| - \frac{\hbar\Omega}{2}\left|e\right\rangle\left\langle g\right| - \frac{\hbar\Omega}{2}\left|g\right\rangle\left\langle e\right|\Big) \\
&\quad + i\hbar\Big(-\frac{i\omega_L}{2}\left|g\right\rangle\left\langle g\right| + \frac{i\omega_L}{2}\left|e\right\rangle\left\langle e\right|\Big) \\
&= \Big(\frac{-\hbar(\omega_0-\omega_L)}{2}\left|g\right\rangle\left\langle g\right| + \frac{\hbar(\omega_0-\omega_L)}{2}\left|e\right\rangle\left\langle e\right| - \frac{\hbar\Omega}{2}\left|e\right\rangle\left\langle g\right| - \frac{\hbar\Omega}{2}\left|g\right\rangle\left\langle e\right|\Big) \\
&= \Big(\frac{-\hbar\Delta}{2}\left|g\right\rangle\left\langle g\right| + \frac{\hbar\Delta}{2}\left|e\right\rangle\left\langle e\right| - \frac{\hbar\Omega}{2}\left|e\right\rangle\left\langle g\right| - \frac{\hbar\Omega}{2}\left|g\right\rangle\left\langle e\right|\Big)
\end{aligned} \tag{A.6}$$

Bibliography

[1] P. Benioff, "The computer as a physical system: A microscopic quantum mechanical Hamiltonian model of computers as represented by Turing machines," *Journal of Statistical Physics*, vol. 22, no. 5, pp. 563–591, 1980. 1, 5

[2] R. P. Feynman, "Simulating physics with computers," *International Journal of Theoretical Physics*, vol. 21, no. 6, pp. 467–488, 1982. 1

[3] I. Buluta and F. Nori, "Quantum Simulators," *Science*, vol. 326, no. 5949, pp. 108–111, 2009. 1

[4] S. Pirandola, B. R. Bardhan, T. Gehring, C. Weedbrook, and S. Lloyd, "Advances in photonic quantum sensing," *Nature Photonics*, vol. 12, no. 12, pp. 724–733, 2018. 1

[5] H. J. Kimble, "The quantum internet," *Nature*, vol. 453, no. 7198, pp. 1023–1030, 2008. 1

[6] P. Senellart, G. Solomon, and A. White, "High-performance semiconductor quantum-dot single-photon sources," *Nature Nanotechnology*, vol. 12, no. 11, pp. 1026–1039, 2017. 1, 10

[7] P. Michler, A. Kiraz, C. Becher, W. V. Schoenfeld, P. M. Petroff, L. Zhang, E. Hu, and A. Imamoglu, "A quantum dot single-photon turnstile device," *Science*, vol. 290, no. 5500, pp. 2282–2285, 2000. 1, 2

[8] N. H. Wan, T.-J. Lu, K. C. Chen, M. P. Walsh, M. E. Trusheim, L. De Santis, E. A. Bersin, I. B. Harris, S. L. Mouradian, I. R. Christen, E. S. Bielejec, and D. Englund, "Large-scale integration of artificial atoms in hybrid photonic circuits," *Nature*, vol. 583, no. 7815, pp. 226–231, 2020. 2

[9] A. Muller, W. Fang, J. Lawall, and G. S. Solomon, "Creating polarization-entangled photon pairs from a semiconductor quantum dot using the optical stark effect," *Physical Review Letters*, vol. 103, no. 21, p. 217402, 2009. 2, 24, 29

[10] I. Schwartz, D. Cogan, E. R. Schmidgall, Y. Don, L. Gantz, O. Kenneth, N. H. Lindner, and D. Gershoni, "Deterministic generation of a cluster state of entangled photons," *Science*, vol. 354, no. 6311, pp. 434–437, 2016. 2, 29

[11] H. J. Briegel and R. Raussendorf, "Persistent Entanglement in Arrays of Interacting Particles," *Physical Review Letters*, vol. 86, no. 5, pp. 910–913, 2001. 2, 10

[12] D. Schlingemann and R. F. Werner, "Quantum error-correcting codes associated with graphs," *Physical Review A*, vol. 65, no. 1, p. 012308, 2001. 2

[13] N. H. Lindner and T. Rudolph, "Proposal for pulsed on-demand sources of photonic cluster state strings," *Physical Review Letters*, vol. 103, no. 11, p. 113602, 2009. 2, 26

[14] C. E. Shannon, "A mathematical theory of communication," *Bell System Technical Journal*, vol. 27, no. 3, pp. 379–423, 1948. 5

[15] A. M. Turing, "On computable numbers, with an application to the entscheidungsproblem," *Proceedings of the London Mathematical Society*, vol. s2-42, no. 1, pp. 230–265, 1937. 5

[16] D. Deutsch, "Quantum theory, the Church–Turing principle and the universal quantum computer," *Proceedings of the Royal Society of London. A. Mathematical and Physical Sciences*, vol. 400, no. 1818, pp. 97–117, 1985. 5

[17] P. Shor, "Algorithms for quantum computation: Discrete logarithms and factoring," in *Proceedings 35th Annual Symposium on Foundations of Computer Science*, pp. 124–134, 1994. 5

[18] A. S. Holevo, "Bounds for the quantity of information transmitted by a quantum communication channel," *Problemy Peredachi Informatsii*, vol. 9, no. 3, pp. 3–11, 1973. 5

[19] R. S. Ingarden, "Quantum information theory," *Reports on Mathematical Physics*, vol. 10, no. 1, pp. 43–72, 1976. 5

[20] B. Schumacher, "Quantum coding," *Physical Review A*, vol. 51, no. 4, pp. 2738–2747, 1995. 5

[21] J. Chow, O. Dial, and J. Gambetta, "IBM Quantum breaks the 100-qubit processor barrier." https://research.ibm.com/blog/127-qubit-quantum-processor-eagle, 2021. 5

[22] Google Quantum AI team and collaborators, "Quantum error correction below the surface code threshold," *Nature*, pp. 1–3, 2024. 5

[23] R. Horodecki, P. Horodecki, M. Horodecki, and K. Horodecki, "Quantum entanglement," *Reviews of Modern Physics*, vol. 81, no. 2, pp. 865–942, 2009. 9

[24] H. J. Briegel, "Cluster States," in *Compendium of Quantum Physics* (D. Greenberger, K. Hentschel, and F. Weinert, eds.), pp. 96–105, Berlin, Heidelberg: Springer, 2009. 9

[25] M. Hillery, V. Bužek, and A. Berthiaume, "Quantum secret sharing," *Physical Review A*, vol. 59, no. 3, pp. 1829–1834, 1999. 9

[26] B. Kraus, "Local unitary equivalence of multipartite pure states," *Physical Review Letters*, vol. 104, no. 2, p. 020504, 2010. 9

[27] M. Hein, W. Dür, J. Eisert, R. Raussendorf, M. V. den Nest, and H. Briegel, "Entanglement in graph states and its applications," 2006. 10

[28] R. Raussendorf and H. J. Briegel, "A one-way quantum computer," *Physical Review Letters*, vol. 86, no. 22, pp. 5188–5191, 2001. 10

[29] A. Fowler and K. Goyal, "Topological cluster state quantum computing," *Quantum Information and Computation*, vol. 9, no. 9&10, pp. 721–738, 2009. 10

[30] C. Couteau, S. Barz, T. Durt, T. Gerrits, J. Huwer, R. Prevedel, J. Rarity, A. Shields, and G. Weihs, "Applications of single photons to quantum communication and computing," *Nature Reviews Physics*, vol. 5, no. 6, pp. 326–338, 2023. 10, 14

[31] I. Aharonovich, D. Englund, and M. Toth, "Solid-state single-photon emitters," *Nature Photonics*, vol. 10, no. 10, pp. 631–641, 2016. 10, 15

[32] R. Hanbury Brown and R. Q. Twiss, "Correlation between photons in two coherent beams of light," *Nature*, vol. 177, no. 4497, pp. 27–29, 1956. 10

[33] C. K. Hong, Z. Y. Ou, and L. Mandel, "Measurement of subpicosecond time intervals between two photons by interference," *Physical Review Letters*, vol. 59, no. 18, pp. 2044–2046, 1987. 12

[34] L. A. Ngah, O. Alibart, L. Labonté, V. D'Auria, and S. Tanzilli, "Ultra-fast heralded single photon source based on telecom technology," *Laser & Photonics Reviews*, vol. 9, no. 2, pp. L1–L5, 2015. 14

[35] S. Krapick, H. Herrmann, V. Quiring, B. Brecht, H. Suche, and C. Silberhorn, "An efficient integrated two-color source for heralded single photons," *New Journal of Physics*, vol. 15, no. 3, p. 033010, 2013. 14

[36] H.-S. Zhong, Y. Li, W. Li, L.-C. Peng, Z.-E. Su, Y. Hu, Y.-M. He, X. Ding, W. Zhang, H. Li, L. Zhang, Z. Wang, L. You, X.-L. Wang, X. Jiang, L. Li, Y.-A. Chen, N.-L. Liu, C.-Y. Lu, and J.-W. Pan, "12-Photon Entanglement and Scalable Scattershot Boson Sampling with Optimal Entangled-Photon Pairs from Parametric Down-Conversion," *Physical Review Letters*, vol. 121, no. 25, p. 250505, 2018. 14

[37] P. Maunz, D. L. Moehring, S. Olmschenk, K. C. Younge, D. N. Matsukevich, and C. Monroe, "Quantum interference of photon pairs from two remote trapped atomic ions," *Nature Physics*, vol. 3, no. 8, pp. 538–541, 2007. 14

[38] D. B. Higginbottom, L. Slodička, G. Araneda, L. Lachman, R. Filip, M. Hennrich, and R. Blatt, "Pure single photons from a trapped atom source," *New Journal of Physics*, vol. 18, no. 9, p. 093038, 2016. 14

[39] D. P. Ornelas-Huerta, A. N. Craddock, E. A. Goldschmidt, A. J. Hachtel, Y. Wang, P. Bienias, A. V. Gorshkov, S. L. Rolston, and J. V. Porto, "On-demand indistinguishable single photons from an efficient and pure source based on a Rydberg ensemble," *Optica*, vol. 7, no. 7, pp. 813–819, 2020. 14

[40] A. Dréau, A. Tchebotareva, A. E. Mahdaoui, C. Bonato, and R. Hanson, "Quantum Frequency Conversion of Single Photons from a Nitrogen-Vacancy Center in Diamond to Telecommunication Wavelengths," *Physical Review Applied*, vol. 9, no. 6, p. 064031, 2018. 14, 15

[41] B. Hensen, H. Bernien, A. E. Dréau, A. Reiserer, N. Kalb, M. S. Blok, J. Ruitenberg, R. F. L. Vermeulen, R. N. Schouten, C. Abellán, W. Amaya, V. Pruneri, M. W. Mitchell, M. Markham, D. J. Twitchen, D. Elkouss, S. Wehner, T. H. Taminiau, and R. Hanson, "Loophole-free Bell inequality violation using electron spins separated by 1.3 kilometres," *Nature*, vol. 526, no. 7575, pp. 682–686, 2015. 14

[42] Y.-M. He, G. Clark, J. R. Schaibley, Y. He, M.-C. Chen, Y.-J. Wei, X. Ding, Q. Zhang, W. Yao, X. Xu, C.-Y. Lu, and J.-W. Pan, "Single quantum emitters in monolayer semiconductors," *Nature Nanotechnology*, vol. 10, no. 6, pp. 497–502, 2015. 14

[43] C. Palacios-Berraquero, D. M. Kara, A. R.-P. Montblanch, M. Barbone, P. Latawiec, D. Yoon, A. K. Ott, M. Loncar, A. C. Ferrari, and M. Atatüre,

"Large-scale quantum-emitter arrays in atomically thin semiconductors," *Nature Communications*, vol. 8, no. 1, p. 15093, 2017. 14

[44] C. Fournier, S. Roux, K. Watanabe, T. Taniguchi, S. Buil, J. Barjon, J.-P. Hermier, and A. Delteil, "Two-Photon Interference from a Quantum Emitter in Hexagonal Boron Nitride," *Physical Review Applied*, vol. 19, no. 4, p. L041003, 2023. 14

[45] M. Anderson, T. Müller, J. Skiba-Szymanska, A. B. Krysa, J. Huwer, R. M. Stevenson, J. Heffernan, D. A. Ritchie, and A. J. Shields, "Gigahertz-Clocked Teleportation of Time-Bin Qubits with a Quantum Dot in the Telecommunication C Band," *Physical Review Applied*, vol. 13, no. 5, p. 054052, 2020. 14, 15

[46] N. Somaschi, V. Giesz, L. De Santis, J. C. Loredo, M. P. Almeida, G. Hornecker, S. L. Portalupi, T. Grange, C. Antón, J. Demory, C. Gómez, I. Sagnes, N. D. Lanzillotti-Kimura, A. Lemaítre, A. Auffeves, A. G. White, L. Lanco, and P. Senellart, "Near-optimal single-photon sources in the solid state," *Nature Photonics*, vol. 10, no. 5, pp. 340–345, 2016. 14, 16

[47] D. C. Burnham and D. L. Weinberg, "Observation of Simultaneity in Parametric Production of Optical Photon Pairs," *Physical Review Letters*, vol. 25, no. 2, pp. 84–87, 1970. 13

[48] S. Ramelow, A. Mech, M. Giustina, S. Gröblacher, W. Wieczorek, J. Beyer, A. Lita, B. Calkins, T. Gerrits, S. W. Nam, A. Zeilinger, and R. Ursin, "Highly efficient heralding of entangled single photons," *Optics Express*, vol. 21, no. 6, pp. 6707–6717, 2013. 14

[49] E. Pomarico, B. Sanguinetti, T. Guerreiro, R. Thew, and H. Zbinden, "MHz rate and efficient synchronous heralding of single photons at telecom wavelengths," *Optics Express*, vol. 20, no. 21, pp. 23846–23855, 2012. 14

[50] M. Tippmann, E. Fitzke, O. Nikiforov, P. Kleinpaß, T. Dolejsky, M. Mengler, and T. Walther, "Fiber-based double-pass single-crystal photon-pair source for quantum key distribution in a network," *Physical Review Applied*, vol. 23, no. 3, p. 034017, 2025. 14

[51] H. J. Kimble, M. Dagenais, and L. Mandel, "Photon Antibunching in Resonance Fluorescence," *Physical Review Letters*, vol. 39, no. 11, pp. 691–695, 1977. 14

[52] M. Saffman, "Quantum computing with atomic qubits and Rydberg interactions: progress and challenges," *Journal of Physics B: Atomic, Molecular and Optical Physics*, vol. 49, no. 20, p. 202001, 2016. 14

[53] R. Blatt and C. F. Roos, "Quantum simulations with trapped ions," *Nature Physics*, vol. 8, no. 4, pp. 277–284, 2012. 14

[54] C. D. Bruzewicz, J. Chiaverini, R. McConnell, and J. M. Sage, "Trapped-ion quantum computing: Progress and challenges," *Applied Physics Reviews*, vol. 6, no. 2, p. 021314, 2019. 15

[55] R. J. MacDonell, C. E. Dickerson, C. J. T. Birch, A. Kumar, C. L. Edmunds, M. J. Biercuk, C. Hempel, and I. Kassal, "Analog quantum simulation of chemical dynamics," *Chemical Science*, vol. 12, no. 28, pp. 9794–9805, 2021. 15

[56] S. Rodt, S. Reitzenstein, and T. Heindel, "Deterministically fabricated solid-state quantum-light sources," *Journal of Physics: Condensed Matter*, vol. 32, no. 15, p. 153003, 2020. 15

[57] S. Sahoo, V. A. Davydov, V. N. Agafonov, and S. I. Bogdanov, "Hybrid quantum nanophotonic devices with color centers in nanodiamonds [Invited]," *Optical Materials Express*, vol. 13, no. 1, pp. 191–217, 2023. 15

[58] C. Kurtsiefer, S. Mayer, P. Zarda, and H. Weinfurter, "Stable Solid-State Source of Single Photons," *Physical Review Letters*, vol. 85, no. 2, pp. 290–293, 2000. 15

[59] N. Mizuochi, T. Makino, H. Kato, D. Takeuchi, M. Ogura, H. Okushi, M. Nothaft, P. Neumann, A. Gali, F. Jelezko, J. Wrachtrup, and S. Yamasaki, "Electrically driven single-photon source at room temperature in diamond," *Nature Photonics*, vol. 6, no. 5, pp. 299–303, 2012. 15

[60] T. M. Babinec, B. J. M. Hausmann, M. Khan, Y. Zhang, J. R. Maze, P. R. Hemmer, and M. Lončar, "A diamond nanowire single-photon source," *Nature Nanotechnology*, vol. 5, no. 3, pp. 195–199, 2010. 15

[61] I. Aharonovich and E. Neu, "Diamond Nanophotonics," *Advanced Optical Materials*, vol. 2, no. 10, pp. 911–928, 2014. 15

[62] R. Bourrellier, S. Meuret, A. Tararan, O. Stéphan, M. Kociak, L. H. G. Tizei, and A. Zobelli, "Bright UV Single Photon Emission at Point Defects in h-BN," *Nano Letters*, vol. 16, no. 7, pp. 4317–4321, 2016. 15

[63] A. Gottscholl, M. Diez, V. Soltamov, C. Kasper, A. Sperlich, M. Kianinia, C. Bradac, I. Aharonovich, and V. Dyakonov, "Room temperature coherent control of spin defects in hexagonal boron nitride," *Science Advances*, vol. 7, no. 14, p. eabf3630, 2021. 15

[64] T. T. Tran, K. Bray, M. J. Ford, M. Toth, and I. Aharonovich, "Quantum emission from hexagonal boron nitride monolayers," *Nature Nanotechnology*, vol. 11, no. 1, pp. 37–41, 2016. 15

[65] P. Auburger and A. Gali, "Towards ab initio identification of paramagnetic substitutional carbon defects in hexagonal boron nitride acting as quantum bits," *Physical Review B*, vol. 104, no. 7, p. 075410, 2021. 15

[66] F. Pinilla, N. Vásquez, I. Chacón, J. R. Maze, C. Cárdenas, and F. Munoz, "Spin-active single photon emitters in hexagonal boron nitride from carbon-based defects," *Physica Scripta*, vol. 98, no. 9, p. 095505, 2023. 15

[67] S. Im, S. Moon, J. Kim, J. Song, C. Ji, S. Pak, and J. K. Kim, "Quantum emitters based on hexagonal boron nitride for next-generation quantum technology," *Progress in Quantum Electronics*, vol. 102, p. 100576, 2025. 15

[68] L. Sapienza, M. Davanço, A. Badolato, and K. Srinivasan, "Nanoscale optical positioning of single quantum dots for bright and pure single-photon emission," *Nature Communications*, vol. 6, no. 1, p. 7833, 2015. 15

[69] I. N. Stranski and L. Krastanow, "Zur Theorie der orientierten Ausscheidung von Ionenkristallen aufeinander," *Monatshefte für Chemie*, vol. 71, no. 1, pp. 351–364, 1937. 16

[70] G. S. Solomon, J. A. Trezza, and J. S. Harris, "Substrate temperature and monolayer coverage effects on epitaxial ordering of InAs and InGaAs islands on GaAs," *Applied Physics Letters*, vol. 66, no. 8, pp. 991–993, 1995. 16

[71] M. Bayer, G. Ortner, O. Stern, A. Kuther, A. A. Gorbunov, A. Forchel, P. Hawrylak, S. Fafard, K. Hinzer, T. L. Reinecke, S. N. Walck, J. P. Reithmaier, F. Klopf, and F. Schäfer, "Fine structure of neutral and charged excitons in self-assembled In(Ga)As/(Al)GaAs quantum dots," *Physical Review B*, vol. 65, no. 19, p. 195315, 2002. 16, 17, 18, 24

[72] D. Gossink, "Droplet etching epitaxy for the nanostructuring of strain-free GaAs quantum dots," Master's thesis, University of Adelaide, 2024. 16, 17

[73] Zh. M. Wang, B. L. Liang, K. A. Sablon, and G. J. Salamo, "Nanoholes fabricated by self-assembled gallium nanodrill on GaAs(100)," *Applied Physics Letters*, vol. 90, no. 11, p. 113120, 2007. 16

[74] S. F. C. da Silva, G. Undeutsch, B. Lehner, S. Manna, T. M. Krieger, M. Reindl, C. Schimpf, R. Trotta, and A. Rastelli, "GaAs quantum dots grown by droplet etching epitaxy as quantum light sources," *Applied Physics Letters*, vol. 119, no. 12, p. 120502, 2021. 16

[75] W. A. Harrison, *Electronic Structure and the Properties of Solids: The Physics of the Chemical Bond*. New York: Dover, 1989. 17

[76] M. Abbarchi, C. Mastrandrea, T. Kuroda, A. Vinattieri, T. Mano, N. Koguchi, K. Sakoda, and M. Gurioli, "Line broadening of excitonic complexes in self-assembled GaAs/AlGaAs single quantum dots," *Physica Status Solidi c*, vol. 6, no. 4, pp. 886–889, 2009. 17

[77] D. Cogan, O. Kenneth, N. Lindner, G. Peniakov, C. Hopfmann, D. Dalacu, P. Poole, P. Hawrylak, and D. Gershoni, "Depolarization of electronic spin qubits confined in semiconductor quantum dots," *Physical Review X*, vol. 8, no. 4, p. 041050, 2018. 17

[78] C. P. Slichter, *Principles of Magnetic Resonance*, vol. 1. Springer Science & Business Media, 2013. 20

[79] D. Paget, G. Lampel, B. Sapoval, and V. I. Safarov, "Low field electron-nuclear spin coupling in gallium arsenide under optical pumping conditions," *Physical Review B*, vol. 15, no. 12, pp. 5780–5796, 1977. 20

[80] R. de Sousa and S. D. Sarma, "Electron spin coherence in semiconductors: Considerations for a spin-based solid-state quantum computer architecture," *Physical Review B*, vol. 67, no. 3, p. 033301, 2003. 20

[81] I. A. Merkulov, Al. L. Efros, and M. Rosen, "Electron spin relaxation by nuclei in semiconductor quantum dots," *Physical Review B*, vol. 65, no. 20, p. 205309, 2002. 20

[82] R. Trivedi, K. A. Fischer, J. Vučković, and K. Müller, "Generation of non-classical light using semiconductor quantum dots," *Advanced Quantum Technologies*, vol. 3, no. 1, p. 1900007, 2020. 21, 23

[83] A. Schwan, B.-M. Meiners, A. Greilich, D. R. Yakovlev, M. Bayer, A. D. B. Maia, A. A. Quivy, and A. B. Henriques, "Anisotropy of electron and hole g-factors in (In,Ga)As quantum dots," *Applied Physics Letters*, vol. 99, no. 22, p. 221914, 2011. 22

[84] A. Shabaev, A. L. Efros, D. Gammon, and I. A. Merkulov, "Optical readout and initialization of an electron spin in a single quantum dot," *Physical Review B*, vol. 68, no. 20, p. 201305, 2003. 22

[85] P. Corfdir, Y. Fontana, B. Van Hattem, E. Russo-Averchi, M. Heiss, A. Fontcuberta i Morral, and R. T. Phillips, "Tuning the g-factor of neutral and charged excitons confined to self-assembled (Al,Ga)As shell quantum dots," *Applied Physics Letters*, vol. 105, no. 22, p. 223111, 2014. 22

[86] K. De Greve, L. Yu, P. L. McMahon, J. S. Pelc, C. M. Natarajan, N. Y. Kim, E. Abe, S. Maier, C. Schneider, M. Kamp, S. Höfling, R. H. Hadfield, A. Forchel, M. M. Fejer, and Y. Yamamoto, "Quantum-dot spin–photon entanglement via frequency downconversion to telecom wavelength," *Nature*, vol. 491, no. 7424, pp. 421–425, 2012. 23, 25

[87] N. Akopian, N. H. Lindner, E. Poem, Y. Berlatzky, J. Avron, D. Gershoni, B. D. Gerardot, and P. M. Petroff, "Entangled photon pairs from semiconductor quantum dots," *Physical Review Letters*, vol. 96, no. 13, p. 130501, 2006. 23

[88] O. Benson, C. Santori, M. Pelton, and Y. Yamamoto, "Regulated and entangled photons from a single quantum dot," *Physical Review Letters*, vol. 84, no. 11, pp. 2513–2516, 2000. 23

[89] M. A. Nielsen and I. L. Chuang, *Quantum Computation and Quantum Information*. Cambridge: Cambridge university press, 10th anniversary edition ed., 2010. 24

[90] R. M. Stevenson, R. J. Young, P. See, D. G. Gevaux, K. Cooper, P. Atkinson, I. Farrer, D. A. Ritchie, and A. J. Shields, "Magnetic-field-induced reduction of the exciton polarization splitting in InAs quantum dots," *Physical Review B*, vol. 73, no. 3, p. 033306, 2006. 24

[91] T. Kuroda, T. Mano, N. Ha, H. Nakajima, H. Kumano, B. Urbaszek, M. Jo, M. Abbarchi, Y. Sakuma, K. Sakoda, I. Suemune, X. Marie, and T. Amand, "Symmetric quantum dots as efficient sources of highly entangled photons: Violation of Bell's inequality without spectral and temporal filtering," *Physical Review B*, vol. 88, no. 4, p. 041306, 2013. 24

[92] W. B. Gao, P. Fallahi, E. Togan, J. Miguel-Sanchez, and A. Imamoglu, "Observation of entanglement between a quantum dot spin and a single photon," *Nature*, vol. 491, no. 7424, pp. 426–430, 2012. 25

[93] N. Coste, D. A. Fioretto, N. Belabas, S. C. Wein, P. Hilaire, R. Frantzeskakis, M. Gundin, B. Goes, N. Somaschi, M. Morassi, A. Lemaître, I. Sagnes, A. Harouri, S. E. Economou, A. Auffeves, O. Krebs, L. Lanco, and P. Senellart, "High-rate entanglement between a semiconductor spin and indistinguishable photons," *Nature Photonics*, vol. 17, no. 7, pp. 582–587, 2023. 27, 29

[94] M. Van den Nest, J. Dehaene, and B. De Moor, "Local invariants of stabilizer codes," *Physical Review A*, vol. 70, no. 3, p. 032323, 2004. 27

[95] E. M. Purcell, H. C. Torrey, and R. V. Pound, "Resonance absorption by nuclear magnetic moments in a solid," *Physical Review*, vol. 69, no. 1-2, pp. 37–38, 1946. 28

[96] G. S. Solomon, M. Pelton, and Y. Yamamoto, "Single-mode spontaneous emission from a single quantum dot in a three-dimensional microcavity," *Physical Review Letters*, vol. 86, no. 17, pp. 3903–3906, 2001. 28

[97] M. Bayer, O. Stern, A. Kuther, and A. Forchel, "Spectroscopic study of dark excitons in $In_xGa_{1-x}As$ self-assembled quantum dots by a magnetic-field-induced symmetry breaking," *Physical Review B*, vol. 61, no. 11, pp. 7273–7276, 2000. 28

[98] D. Cogan, Z. E. Su, O. Kenneth, and D. Gershoni, "Deterministic generation of indistinguishable photons in a cluster state," *Nature Photonics*, vol. 17, no. 4, pp. 324–329, 2023. 29, 47

[99] T. A. Wilkinson, D. J. Cottrill, J. M. Cramlet, C. E. Maurer, C. J. Flood, A. S. Bracker, M. Yakes, D. Gammon, and E. B. Flagg, "Spin-selective AC Stark shifts in a charged quantum dot," *Applied Physics Letters*, vol. 114, no. 13, p. 133104, 2019. 29, 36, 48

[100] M. O. Scully and M. S. Zubairy, *Quantum Optics*. Cambridge: Cambridge University Press, 1997. 32, 40

[101] S. Haroche and J.-M. Raimond, *Exploring the Quantum: Atoms, Cavities and Photons*. Oxford Graduate Texts, Oxford ; New York: Oxford University Press, 2006. 33

[102] E. B. Flagg and G. S. Solomon, "Optical spin readout method in a quantum dot using the ac Stark effect," *Physical Review B*, vol. 92, no. 24, p. 245309, 2015. 37

[103] N. Lambert, E. Giguère, P. Menczel, B. Li, P. Hopf, G. Suárez, M. Gali, J. Lishman, R. Gadhvi, R. Agarwal, A. Galicia, N. Shammah, P. Nation, J. R. Johansson, S. Ahmed, S. Cross, A. Pitchford, and F. Nori, "QuTiP 5: The Quantum Toolbox in Python," 2024. 39

[104] V. Weisskopf and E. Wigner, "Berechnung der natürlichen Linienbreite auf Grund der Diracschen Lichttheorie," *Zeitschrift fr Physik*, vol. 63, no. 1-2, pp. 54–73, 1930. 39

[105] M. Lax, "Formal theory of quantum fluctuations from a driven state," *Physical Review*, vol. 129, no. 5, pp. 2342–2348, 1963. 40

[106] J.-P. Jahn, *An Artificial Rubidium Atom*. Thesis, University of Basel, 2018. 41

[107] P. A. Dalgarno, J. M. Smith, J. McFarlane, B. D. Gerardot, K. Karrai, A. Badolato, P. M. Petroff, and R. J. Warburton, "Coulomb interactions in single charged self-assembled quantum dots: Radiative lifetime and recombination energy," *Physical Review B*, vol. 77, no. 24, p. 245311, 2008. 41

[108] C. F. Jekel, G. Venter, M. P. Venter, N. Stander, and R. T. Haftka, "Similarity measures for identifying material parameters from hysteresis loops using inverse analysis," *International Journal of Material Forming*, vol. 12, no. 3, pp. 355–378, 2019. 51

[109] K. Tokuhara, Y. Ohtsu, F. Ono, O. Yamada, M. Sagawa, and Y. Matsuura, "Magnetization and torque measurements on Nd2Fe14B single crystals," *Solid State Communications*, vol. 56, no. 4, pp. 333–336, 1985. 54

[110] Y. Z. He, "Experimental research on the residual magnetization of a rare-earth permanent magnet for a cryogenic undulator," *Chinese Physics B*, vol. 22, no. 7, p. 074101, 2013. 54

[111] P. Steindl, T. van der Ent, H. van der Meer, J. Frey, J. Norman, J. Bowers, D. Bouwmeester, and W. Löffler, "Resonant two-laser spin-state spectroscopy of a negatively charged quantum-dot–microcavity system with a cold permanent magnet," *Physical Review Applied*, vol. 20, no. 1, p. 014026, 2023. 54

[112] M. Ortner and L. G. Coliado Bandeira, "Magpylib: A free Python package for magnetic field computation," *SoftwareX*, vol. 11, p. 100466, 2020. 54

[113] J. Y. Marzin, J. M. Gérard, A. Izraël, D. Barrier, and G. Bastard, "Photoluminescence of single inas quantum dots obtained by self-organized growth on gaas," *Physical Review Letters*, vol. 73, no. 5, pp. 716–719, 1994. 55

[114] J. Chang, I. E. Zadeh, J. W. N. Los, J. Zichi, A. Fognini, M. Gevers, S. Dorenbos, S. F. Pereira, P. Urbach, and V. Zwiller, "Multimode-fiber-coupled superconducting nanowire single-photon detectors with high detection efficiency and time resolution," *Applied Optics*, vol. 58, no. 36, pp. 9803–9807, 2019. 58

[115] J. Claudon, J. Bleuse, N. S. Malik, M. Bazin, P. Jaffrennou, N. Gregersen, C. Sauvan, P. Lalanne, and J.-M. Gérard, "A highly efficient single-photon source based on a quantum dot in a photonic nanowire," *Nature Photonics*, vol. 4, no. 3, pp. 174–177, 2010. 61

[116] K. Brunner, U. Bockelmann, G. Abstreiter, M. Walther, G. Böhm, G. Tränkle, and G. Weimann, "Photoluminescence from a single GaAs/AlGaAs quantum dot," *Physical Review Letters*, vol. 69, no. 22, pp. 3216–3219, 1992. 62, 63

[117] T. Sekiguchi, Y. Sakuma, and T. Takebe, "Cathodoluminescence study of AlGaAs/GaAs multilayers grown on ridge-type triangles on GaAs (111)A substrates," *Journal of Electron Microscopy*, vol. 52, no. 4, pp. 383–389, 2003. 63

[118] S. B. Nam, D. C. Reynolds, C. W. Litton, R. J. Almassy, T. C. Collins, and C. M. Wolfe, "Free-exciton energy spectrum in GaAs," *Physical Review B*, vol. 13, no. 2, pp. 761–767, 1976. 63

[119] E. Schöll, L. Hanschke, L. Schweickert, K. D. Zeuner, M. Reindl, S. F. Covre Da Silva, T. Lettner, R. Trotta, J. J. Finley, K. Müller, A. Rastelli, V. Zwiller, and K. D. Jöns, "Resonance fluorescence of GaAs quantum dots with near-unity photon indistinguishability," *Nano Letters*, vol. 19, no. 4, pp. 2404–2410, 2019. 63, 65

[120] C. Heyn, C. Strelow, and W. Hansen, "Excitonic lifetimes in single GaAs quantum dots fabricated by local droplet etching," *New Journal of Physics*, vol. 14, no. 5, p. 053004, 2012. 63

[121] P. Tighineanu, R. Daveau, E. H. Lee, J. D. Song, S. Stobbe, and P. Lodahl, "Decay dynamics and exciton localization in large GaAs quantum dots grown by droplet epitaxy," *Physical Review B*, vol. 88, no. 15, p. 155320, 2013. 63, 64

[122] P. A. Dalgarno, J. McFarlane, B. D. Gerardot, R. J. Warburton, K. Karrai, A. Badolato, and P. M. Petroff, "Decay dynamics of the positively charged exciton in a single charge tunable self-assembled quantum dot," *Applied Physics Letters*, vol. 89, no. 4, p. 043107, 2006. 63

[123] P. A. Dalgarno, J. M. Smith, B. D. Gerardot, A. O. Govorov, K. Karrai, P. M. Petroff, and R. J. Warburton, "Dark exciton decay dynamics of a semiconductor quantum dot," *Physica Status Solidi (a)*, vol. 202, no. 14, pp. 2591–2597, 2005. 64

[124] N. Ha, T. Mano, T. Kuroda, Y. Sakuma, and K. Sakoda, "Current-injection quantum-entangled-pair emitter using droplet epitaxial quantum dots on GaAs(111)A," *Applied Physics Letters*, vol. 115, no. 8, p. 083106, 2019. 65